Jet de basse couche nocturne en été dans la région parisienne : interactions avec la chaleur urbaine et les caractéristiques de surface.

Jonnathan Céspedes Rojas

INSTITUT POLYTECHNIQUE DE PARIS

NNT : 2024IPPAX091

Thèse de doctorat

Summertime nocturnal Low-Level Jet in the Paris region: interactions with the urban heat and surface characteristics

Thèse de doctorat de l'Institut Polytechnique de Paris
préparée à l'École polytechnique

École doctorale n°626: École Doctorale de l'Institut Polytechnique de Paris (ED IP Paris)
Spécialité de doctorat : Mécanique des fluides et des solides, acoustique

Thèse présentée et soutenue à Palaiseau, le 13.11.2024, par

JONNATHAN CÉSPEDES ROJAS

Composition du Jury :

Riwal Plougonven Professeur, École polytechnique	Président
Ulrich Löhnert Professeur, Universität zu Köln	Rapporteur
Matthias Mauder Professeur, Technische Universität Dresden	Rapporteur
Natalie Theeuwes Chargée de recherche, Royal Netherlands Meteorological Institute	Examinatrice
Elsa Dieudonné Maîtresse de conférences, Université du Littoral Côte d'Opale	Examinatrice
Martial Haeffelin Ingénieur de recherche, CNRS	Directeur de thèse
Simone Kotthaus Professeure assistante, École Polytechnique	Co-directrice de thèse
Clément Toupoint Ingénieur, Vaisala France	Invité

Acknowledgments

My PhD journey has been a transformative experience, leaving an indelible mark on both my personal and professional life. It has undoubtedly been the challenge of my life, requiring me to adapt to a new country, language, and perspectives. While this adventure was often exciting, it was not without its difficulties. I would like to take a moment to acknowledge the many people and organizations that played a role in this journey.

This PhD project was made possible through funding from the Île-de-France Region as part of the "Paris Region PhD 2020" program (Convention No. 20007179). This thesis is based on data collected by a Doppler Wind Lidar Vaisala WindCube Scan 400s, acquired through funding from the DIM QI2 program supported by Région Île-de-France, the OBS4CLIM project funded by ANR under the France 2030 program, the ACTRIS-FR research infrastructure, and CNRS-INSU. This thesis has been conducted in the context of the COST Action PROBE (CA18235), supported by COST (European Cooperation in Science and Technology, https://www.cost.eu/).

One of the aspects I appreciated most about my PhD was conducting research at the intersection of academia and industry. On the academic side, I would like to extend my deepest gratitude to my supervisors, Martial Haeffelin and Simone Kotthaus. When I began this thesis, I knew I was facing a big challenge, Simone demonstrated remarkable patience and dedication in helping me tackle this challenge day by day. She was always available to answer my questions, discuss and help me understand my own results. Her scientific view was invaluable in contextualizing my findings. I am equally grateful to Martial, who was always available to support me. His extensive experience doing research, coupled with his global and structured vision, provided me with key feedback that consistently guided the project in the right direction. To both of you, I sincerely appreciate your support, working with you has been a truly rewarding experience.

In addition, I could not been more lucky to have such special and collaborative teammates at SIRTA team. I want to express special thanks to Marc-Antoine Drouin whose support in all related to the development of my code and computational aspects was essential for academic formation. I'm also very grateful to Christophe Boitel, Jean-Charles Dupont, and Jean-François Ribaud, all of you contributed to my project in many different ways from technical aspects to very exciting scientific discussions. The PANAME field work was a very nice team experience from which I learned a lot and was able to put in real context the theory learned in the classes.

On the industrial side, I am grateful to Vaisala France, as in addition to providing funding through the scholarship, the LMD - VAISALA collaboration (École polytechnique research collaboration contract No. 2021COLLR0009) allowed me to gain practical knowledge of the WindCube Scan 400s, from its installation to the development of a new scanning strategy. Furthermore, Vaisala hosted me at their facilities during my thesis, enabling fruitful discussions with the data science team. Special thanks to Ludovic Thobois, Clément Toupoint, and Jana Preissler, my advisors at Vaisala, who were always available to support me in overcoming the challenges of this experiment and discussing new results.

Part of the novelty of my thesis is the consolidation of a long-term wind data set collected in the urban environment of Paris, France. Over nearly three years, this instrument collected wind measurements that will contribute to a better understanding of the urban atmosphere. I sincerely thank the QUALAIR-SU supersite for hosting the WindCube Scan 400s at the Zamansky Tower experimental platform on the Sorbonne Université campus and for providing meteorological data. Special thanks to Camille Viatte and Cristelle Cailteau-Fischbach for their constant support, from installation to troubleshooting connection issues.

In addition to WindCube Scan 400s data, this thesis incorporates measurements from other sources. I thank EDF R&D/CEREA for providing Doppler lidar WLS70 data from SIRTA, with special appreciation to Aurélien Faucheux for his continuous support and insights on its operation and outputs. Thanks to AERIS for supplying ReOBS data and supporting PANAME (`https://paname.aeris-data.fr/`). Finally, I appreciate Météo-France for providing meteorological surface station data.

I sincerely thank my thesis monitoring committee, Elsa Dieudonné and Marie Lothon, for their time and dedication in reviewing my reports and attending my progress presentations. I also appreciate the jury members—Riwal Plougonven, Ulrich Löhnert, Matthias Mauder, Natalie Theeuwes, and Elsa (again) for their time and effort in reviewing my PhD thesis manuscript.

As I mentioned earlier, this journey has also been a personal one. Outside of work, I was fortunate to receive support from many wonderful people who, over the past three years, almost made me forget that my family was thousands of kilometers away. I am especially grateful to the Cité U team—Louis, Leon, Héloïse, Vincent, Elsa, Bachar, Fex, and Andri. Spending two and a half years at Cité U was an incredible experience, filled with great moments and lasting memories.

My time in the lab would not have been as enjoyable without my dear friends from the Butte-aux-Cailles team: Alessandro, Assia, Charlotte, Félix, Jean, Melania, Rachel, and Shuli. A special thanks to my wonderful girlfriend, Lia ♡, whose support was invaluable during the final sprint of this thesis. The time spent with you all has been a true gift, and you will always have a place in my heart. Of course, I am also grateful to everyone else in the lab, even if I don't have enough space to mention every name here.

No tendría el mismo sentido si no lo escribiera en español. Gracias a mis queridos ticos, Alonso y "Fachis", por adoptarme como un tico más, pero sobre todo como un amigo y parte de su familia. Demasiadas experiencias, kilómetros y emociones que solo pueden resumirse en: we are forever Ravers. También gracias a Marta y Rubén por su hermosa amistad y por los momentos compartidos; son los latinos más españoles que conozco. También agradezco a los chiquitos de Aprobado Añañay, que se ganaron mi corazón.

Para concluir, agradezco infinitamente a mi hermosa familia, mi mayor apoyo y sin duda mis más leales fans. A pesar de la distancia, siempre han estado conmigo, brindándome amor y aliento en cada paso, no solo en esta tesis, sino en cada etapa de mi vida. Gracias por todo el apoyo incondicional, esta victoria también le pertence a ustedes.

Abstract

Although urban surfaces cover between 1–3% of global land, over 50% of the world's population lives in urban areas. Hence, cities are a critical interface for the interaction between humans and the Atmospheric Boundary Layer (ABL). Urban surfaces characterized by direct heat emissions, impervious materials, and increased roughness, retain heat more efficiently than organic surfaces and alter airflow through increased friction. As a consequence, cities experience a unique microclimate and the Urban Boundary Layer (UBL) is characterized by lower wind speeds and enhanced turbulence At night, cities tend to be warmer than their rural surroundings, a phenomenon known as nocturnal Urban Heat Island (UHI). The UHI exacerbates heat-related risks to human health by disrupting sleep quality, negatively impacting health and quality of life. Synoptic weather further influences ABL dynamics, impacting transport processes, urban-induced circulations, near-surface microclimates, and air quality. Currently, these interactions are not well understood or quantified in real-world conditions, partly due to a lack of observations that characterize the spatial and temporal variations of relevant UBL dynamics.

This thesis examines how the regional-scale nocturnal Low-Level Jet (LLJ) interacts with the UBL and the surface of the Paris region (France). The presented results highlight advances both regarding methodological achievements and novel scientific findings. Novel observations of wind and turbulence profiles were collected over the course of two years using Doppler Wind Lidar (DWL) techniques. Data were recorded simultaneously at two experimental sites: the QUALAIR-SU urban site in central Paris and the SIRTA suburban site in Palaiseau, $25\,\mathrm{km}$ southwest of the city center. To effectively exploit these data sets, an algorithm was developed for the automatic detection and characterisation of LLJ events. A novel shallow (Doppler Beam Swinging) DBS scan was proposed with proven benefits for the monitoring of shallow LLJ events. Focused on the summer periods of 2022 and 2023, a detailed investigation of LLJ characteristics in the Paris region was conducted to describe their spatial and temporal variations and implications for the urban canopy layer UHI.

This quantitative assessment revealed that the LLJ is a frequent nocturnal phenomenon in the region, with inter-annual variability (about 70% of nights with LLJ in 2022, and 40-48% in 2023). These differences were largely explained by the respective synoptic conditions, as southwesterly wind directions appear less favorable for the LLJ formation. The LLJ typically forms after sunset and dissipates after sunrise, with most jets originating from the northeast. The LLJ core heights range from 200 to $950\,\mathrm{m}$ above sea level, with higher altitudes recorded above the city despite its lower ground elevation compared to the suburban site. LLJ speeds vary from 3 to $18\,\mathrm{m\,s^{-1}}$, with an average duration of 8.6 h. The LLJ characteristics

and its associated mechanical turbulence vary depending on the wind direction. Vertical mixing, quantified by the vertical velocity variance (σ_w^2), was used to classify LLJ events into three categories: high variance (strong LLJs at greater altitudes), medium variance (moderate LLJs), and low variance (mostly weaker LLJs at lower altitudes). The strongest jets were generally linked to northeasterly winds, while weaker jets occurred under more variable conditions. High-variance LLJs display characteristics typical of the inertial oscillation formation mechanism: a systematic increase in wind speed and a veering of the wind direction over the course of the night.

During the extreme heat events in summer 2022 and 2023, night temperatures in central Paris were up to 9°C higher than at a rural site, documenting a pronounced UHI effect. The σ_w^2-based classification system revealed a clear link between the LLJ characteristics and the UHI intensity, showing that the UHI intensity increases as σ_w^2 values decrease, with the highest UHI only observed during LLJ events with very weak σ_w^2. The LLJ impact on the UHI intensity is associated with variations in atmospheric stability as increased stratification can cause the LLJ to detach from the urban surface, allowing cool air to remain aloft and not mix into the urban canopy layer.

Topography and urban buoyancy were found to affect the LLJ. Again, the exchange of vertical momentum between the near-surface atmosphere and the LLJ core was found to play an important role. Analyzing LLJ events by wind direction sectors it was found that jets from the northeast sector present higher core heights and lower wind speeds at the suburban site compared to the urban site, with the differences increasing as LLJ core wind speeds increase. The LLJ interacts with the topography, causing vertical momentum transport that elevates the jet core and reduces horizontal wind speed. Differences between LLJ at the two sites were minimal for events with weak vertical mixing (predominantly from the southeast) as atmospheric stratification detached the jet flow from surface drag forces. In the northwest sector, the urban atmosphere plays a role in driving spatial variability in the LLJ core characteristics. In this sector, intermediate-height jets with intermediate to low speeds were detected at greater heights over the city as the nocturnal buoyancy over the urban surface displaces the jet core slightly upwards.

The findings of this thesis highlight the great importance of ABL dynamics as a link between synoptic-scale flow conditions and the urban atmosphere. Results not only deepen our understanding of the nocturnal LLJ but also have clear implications for critical environmental risks in cities, such as heat or air pollution.

Keywords: Atmospheric Boundary Layer, Low-Level Jet, Atmospheric Stability, Vertical Mixing, Urban Climate, Urban Heat Island, Doppler Wind Lidar.

Résumé

Bien que les surfaces urbaines ne couvrent que 1 à 3 % des terres mondiales, plus de 50 % de la population mondiale vit dans des zones urbaines. Ainsi, les villes constituent une interface essentielle pour les interactions entre les humains et la couche limite atmosphérique (ABL). Les surfaces urbaines, caractérisées par des émissions directes de chaleur, des matériaux imperméables et une rugosité accrue, retiennent la chaleur plus efficacement que les surfaces naturelles et modifient les flux d'air. Par conséquent, les villes connaissent un microclimat particulier, et la couche limite urbaine (UBL) se distingue par des vitesses de vent plus faibles et une turbulence accrue. La nuit, les villes sont souvent plus chaudes que les zones rurales environnantes, un phénomène connu sous le nom d'îlot de chaleur urbaine nocturne (UHI). Ce phénomène aggrave les risques liés à la chaleur en perturbant la qualité du sommeil, ce qui affecte la santé humaine et la qualité de vie. Les conditions météorologiques synoptiques influencent également la dynamique de l'ABL, impactant les processus de transport, les circulations induites par la ville, les microclimats de surface et la qualité de l'air. Actuellement, ces interactions sont mal comprises ou quantifiées dans des conditions réelles, en partie en raison d'un manque d'observations sur les variations spatiales et temporelles des dynamiques de la UBL.

Cette thèse examine comment le Jet de Basse Altitude nocturne (LLJ) à l'échelle régionale interagit avec la UBL et la surface de la région parisienne (France). Les résultats présentés mettent en lumière des avancées tant au niveau méthodologique que des découvertes scientifiques nouvelles. Des observations inédites des profils de vent et de turbulence ont été collectées sur une période de deux ans à l'aide de techniques de lidar Doppler (DWL). Les données ont été enregistrées simultanément sur deux sites expérimentaux : le site urbain QUALAIR-SU au centre de Paris et le site SIRTA périurbain à Palaiseau, situé $25\,\mathrm{km}$ au sud-ouest du centre-ville. Pour exploiter efficacement ces jeux de données, un algorithme a été développé pour la détection et la caractérisation automatiques des événements de LLJ. De plus, un balayage DBS (Doppler Beam Swinging) novateur à basse élévation a été proposé, avec des avantages prouvés pour la caractérisation des événements de LLJ de très basse altitude. En se concentrant sur les périodes estivales de 2022 et 2023, une analyse détaillée des caractéristiques des LLJ dans la région parisienne a été menée pour décrire leurs variations spatiales et temporelles et leurs implications sur l'UHI dans la couche de canopée urbaine.

Cette évaluation quantitative a révélé que le LLJ est un phénomène nocturne fréquent dans la région, avec une variabilité interannuelle (présence de LLJ environ 70 % des nuits en 2022, contre 40 à 48 % en 2023). Ces différences s'expliquent principalement par les conditions synoptiques, les vents de secteur sud-ouest semblant moins favorables à la formation du LLJ. Le LLJ se forme généralement

après le coucher du soleil et se dissipe après le lever du soleil, la plupart des jets provenant du nord-est. Les hauteurs du cœur des LLJ varient de 200 à $950\,\mathrm{m}$ au-dessus du niveau de la mer, avec des altitudes plus élevées enregistrées au-dessus de la ville malgré son altitude plus basse par rapport au site périurbain. Les vitesses des LLJ varient entre 3 et $18\,\mathrm{m\,s^{-1}}$, avec une durée moyenne de 8,6 heures. Les caractéristiques du LLJ et sa turbulence mécanique associée varient en fonction de la direction du vent. Le mélange vertical, quantifié par la variance de la vitesse verticale (σ_w^2), a permis de classer les événements de LLJ en trois catégories : haute variance (jets forts à des altitudes plus élevées), variance moyenne (jets modérés) et faible variance (jets plus faibles à des altitudes plus basses). Les jets les plus puissants étaient généralement associés à des vents de secteur nord-est, tandis que les jets plus faibles se produisaient dans des conditions plus variables. Les LLJ à haute variance affichent des caractéristiques typiques du mécanisme de formation par oscillation inertielle, telles qu'une augmentation systématique de la vitesse du vent et une rotation de la direction du vent au cours de la nuit.

Lors des vagues de chaleur extrêmes de l'été 2022 et 2023, les températures nocturnes dans le centre de Paris étaient jusqu'à 9°C plus élevées que dans un site rural, révélant un effet UHI prononcé. Le système de classification basé sur σ_w^2 a révélé un lien clair entre les caractéristiques du LLJ et l'intensité de l'UHI, montrant que l'intensité de l'UHI augmente à mesure que les valeurs de σ_w^2 diminuent, l'UHI le plus élevé étant observé lors d'événements de LLJ avec des σ_w^2 très faibles, généralement associés à des flux de secteur sud-est. Les vents de secteur nord-est étaient liés à des LLJ à haute variance et à des intensités d'UHI plus faibles. L'impact du LLJ sur l'intensité de l'UHI est associé à des variations de la stabilité atmosphérique, une stratification accrue pouvant détacher le LLJ de la surface urbaine, permettant à l'air frais de rester en altitude sans se mélanger à la couche de canopée urbaine.

La topographie urbaine et la flottabilité atmosphérique ont également été identifiées comme des facteurs influençant le LLJ. L'échange vertical de quantité de mouvement entre l'atmosphère proche de la surface et le cœur du LLJ a également joué un rôle important. En analysant les événements de LLJ par secteur de direction du vent, il a été constaté que les jets provenant du secteur nord-est présentaient des hauteurs de cœur plus élevées et des vitesses de vent plus faibles sur le site périurbain par rapport au site urbain, avec des différences croissantes à mesure que la vitesse du vent au cœur du LLJ augmentait. Le LLJ interagit avec la topographie, provoquant un transport vertical de quantité de mouvement qui élève le cœur du jet et réduit la vitesse horizontale du vent. Les différences entre les LLJ aux deux sites étaient minimes lors d'événements avec un faible mélange vertical (principalement en provenance du sud-est), car la stratification atmosphérique détachait le flux du jet des forces de frottement de surface. Dans le secteur nord-ouest, l'atmosphère urbaine joue un rôle dans la variabilité spatiale des caractéristiques du LLJ. Dans ce

secteur, des jets à hauteur intermédiaire avec des vitesses intermédiaires à faibles ont été détectés à de plus grandes hauteurs au-dessus de la ville, la flottabilité nocturne au-dessus de la surface urbaine déplaçant légèrement le cœur du jet vers le haut.

Les résultats de cette thèse soulignent l'importance de la dynamique de l'ABL en tant que lien entre les conditions de flux synoptiques et l'atmosphère urbaine. Ils approfondissent notre compréhension du LLJ nocturne et ont des implications claires pour des risques environnementaux critiques dans les villes, tels que la chaleur ou la pollution de l'air.

Mots clés : Couche limite atmosphérique, Jet de basse altitude, Stabilité atmosphérique, Mélange vertical, Climat urbain, Îlot de chaleur urbain, Lidar Doppler.

Contents

List of Figures

List of Tables

Chapter 1

Introduction

Contents

1.1 Motivation: linking regional scale flow dynamics and urban heat

Extreme heat is one of the most dangerous health risks faced by urban populations, with severe socio-economic consequences (Canouï-Poitrine et al., 2006; Rojas-Rueda et al., 2021). In the context of a changing climate, extreme heatwaves are becoming more frequent (Lemonsu et al., 2024a) and have increasingly severe impacts on human life and activities. The formation of these extreme events is related to specific synoptic conditions. For example, in the Paris region, an extreme heatwave in summer 2022 was induced by a persistent high-pressure system situated between Morocco, France, and the British Isles that gradually warmed the air, and a secondary low-pressure system located between the Azores and Portugal, which caused the advection of particularly hot air from the Iberian Peninsula. Anomalous temperatures were recorded, accompanied by severe drought with an 80% precipitation deficit and prevailing winds from the northeast (Petit et al., 2023).

In the cities, heat waves are much more intense due to the urban heat island phenomenon (Oke et al., 2017b). This phenomenon exacerbates the impact of heatwaves and makes them last longer (Li and Bou-Zeid, 2013). As a result, the high nocturnal urban temperatures affect the quality of nighttime sleep, with negative impacts on public health. While the causes for urban heat island development are generally well understood, it is still challenging to predict its significant temporal variability that occurs from one night to the next even within a single heat wave event (Petit et al., 2023). As a consequence, temporal variations in UHI intensity are often not taken into account for the implementation of heat mitigation measures and policies to reduce associated risks.

A widely promoted urban planning strategy to mitigate heat-related risks is to increase the proportion of vegetated areas and implement more green spaces and parks in cities. Through shade and evapotranspiration, trees and green spaces can lower heat risks in built-up environments. During the day, shading is key for reducing the total amount of received radiation, with mean radiant temperature being a more meaningful measure of thermal comfort than air temperature (Shashua-Bar and Hoffman, 2000; Grimmond and Oke, 2002). At night, the situation shifts, with thermal radiation and air temperature both becoming more important for the human body. However, there is considerable uncertainty about the factors determining the intensity and spatial extent of these cooling effects (Doick et al., 2014). It is known that factors like biomass density, vegetation type and arrangement, topography, and the size of green spaces influence cooling intensity (Zhu et al., 2021; Cai et al., 2023) while meteorological parameters, such as cloud cover or wind speed also play a critical role (Morris et al., 2001; Lin et al., 2022). However, quantitative knowledge on the impact of boundary layer dynamics and meteorological conditions on the cooling effect of urban green spaces is still limited.

During the extreme heatwave of summer 2022, Haeffelin et al. (2024) found that park cooling efficiency is strongly influenced by mixing conditions in the UBL. As shown in Chapter 3 of this thesis, this period was associated with a high frequency of mesoscale Low-Level Jet (LLJ) events, which caused different intensities of vertical mixing below the height of the maximum wind speed when comparing different nights during this heatwave. Haeffelin et al. (2024) identified three cooling regimes, depending on atmospheric stability and the vertical mixing of Turbulent Kinetic Energy (TKE) generated by the LLJ maximum wind speed. Nocturnal cooling of green spaces is more intense when the urban atmosphere is statically stable, with weak or absent vertical turbulent mixing. In contrast, when mixing is strong, green spaces show weaker cooling, and temperature contrasts between green spaces and nearby built-up areas are reduced.

This thesis investigates how the vertical component of the TKE is then related to the LLJ dynamics and the spatial and temporal variations of its core characteristics. To achieve this, a detailed comparison is conducted between wind

profile observations from a Doppler Wind Lidar (DWL) located in central Paris and another DWL in a suburban setting, taking into account temporal variations of the synoptic flow and spatial variations of the regional topography (Chapter 4).

1.2 The Atmospheric Boundary Layer (ABL)

Apart from the people who live in the International Space Station and very few other exceptions, all humans live in the Atmospheric Boundary Layer (ABL). It has been defined by Stull (1988a) as "*the lowest part of the troposphere that is directly influenced by the presence of the Earth's surface and responds to surface forcing (frictional drag, evaporation and transpiration, heat transfer, pollutant emission, and terrain induced flow modification) with a timescale of about an hour or less*".

An improved understanding of ABL dynamics, based on quantitative knowledge (e.g., long-term profiling observations (Bosveld et al., 2020; Cimini et al., 2020)), is essential because it plays a significant role in various aspects that connect human life to the atmosphere, such as meteorology (Garratt, 1994), aviation operations (Gultepe et al., 2019), renewable energy (Rajewski et al., 2013; Peña et al., 2016), and weather forecasting and climate modeling (Holtslag et al., 2013). Knowledge of ABL meteorology is crucial in urban environments to address environmental risks such as air pollution (Bossioli et al., 2009; Li et al., 2017) and heat risk (Rojas-Rueda et al., 2021; Lemonsu et al., 2024a; Miralles et al., 2014). In rural areas, understanding ABL dynamics is important because it affects agricultural production and determines its environmental impacts (Adegoke et al., 2007).

The ABL represents $\approx 10\%$ of the thickness of the tropospheric column (between 10 and $15\,\mathrm{km}$), it extends vertically from a few hundred of meters up to $\approx 3\,\mathrm{km}$ with variable thickness subject to a diurnal cycle. Given its direct interaction with the Earth's surface, the airflow within the ABL is normally in a turbulent state (Stull, 1988a). The turbulence in the ABL is sustained by two major controllers: heat exchange between the surface and the atmosphere (*thermal turbulence*) (Dabberdt et al., 1993; Kotthaus and Grimmond, 2014), and vertical shear of the horizontal wind (*mechanical turbulence*), which are closely related through the stability of the atmosphere (Holtslag et al., 2013). This thesis mostly focuses on the physical processes related to the mechanical turbulence.

The wind, which is the flow of air in the atmosphere, is primarily driven by variations in atmospheric pressure, known as the *pressure gradient force*. This force affects wind dynamics at different altitudes above ground level. In the free troposphere, where the Earth's surface friction and heat exchange between the surface and atmosphere do not influence the wind, the pressure gradient force can be exactly balanced by the *Coriolis force* (a result of the Earth's rotation), producing

the *geostrophic wind* (see Fig. 1.1) (Monin, 1970). In the geostrophic regime, air moves from regions of high pressure to regions of low pressure at varying wind speeds.

In the ABL, where the wind is in direct contact with the Earth's surface, two additional forces come into play: the *friction force* and the *buoyancy force* (Barlow, 2014). Friction deflects the wind direction towards low-pressure areas and reduces wind speed, while the buoyancy (a result of surface-atmosphere heat exchange) produces ascending parcels of hot air, enhancing the vertical motion of the wind.

Wind can be expressed as a three-dimensional (3D) vector, $\vec{U} = (\vec{u}, \vec{v}, \vec{w})$, composed of the horizontal meridional and zonal components, $\vec{u}$ and $\vec{v}$ respectively, and the vertical velocity component $\vec{w}$. Typically, wind blows roughly parallel to the ground due to the constraining effect of the terrain, causing the magnitudes of the horizontal components ($\vec{u}$, $\vec{v}$) to be much larger than the vertical component ($\vec{w}$). Consequently, instruments measuring weather often approximate wind as a two-dimensional parameter, with a magnitude defined as $U_h = \sqrt{u^2 + v^2}$, and a horizontal direction expressed in terms of the wind origin ϕ (in degrees from geographic north, clockwise) (Oke et al., 2017b). However, surface roughness elements and buoyancy forces enhance vertical wind motions, producing continuous uplift and sinking motions, represented by $\vec{w}$, being positive for updrafts and negative for downdrafts.

Assuming that the U_h magnitude is to be measured at a given point in space over the course of a certain period (t), the records registered by the instrument would show fluctuations over short intervals which are produced by the turbulence. According to the Reynolds decomposition, the instantaneous velocity is composed of a mean (e.g. $\bar{u}$) estimated over a set period t and a certain deviation from that mean (e.g. u'), the latter describing the contribution of turbulent motion at the given instance. The Reynolds decomposition is applicable to all three velocity components:

$$\begin{aligned} u &= \bar{u} + u' \\ v &= \bar{v} + v' \\ w &= \bar{w} + w'. \end{aligned} \tag{1.1}$$

Generally, the turbulence concept is referred to perturbations given at time scales smaller than 30 min (Stull, 1988a).

The turbulent motions of wind can be generated or influenced by the friction force exerted by the Earth's surface. Roughness elements on the surface produce a vertical flux of horizontal momentum near the surface, typically in the lowest 10% of the ABL. This momentum flux is called friction velocity (u_*) and is expressed as follows (Kotthaus and Grimmond, 2014):

$$u_* = [(\overline{u'w'})^2 + (\overline{v'w'})^2]^{1/4}, \tag{1.2}$$

where $\overline{u'w'}$ and $\overline{v'w'}$ are the surface kinematic momentum fluxes in the x and y directions that represent the surface stress, known as *Reynolds stress*, and represents the covariance of horizontal and vertical wind fluctuations near the surface. Hence, u_* is a scaling velocity that accounts for the influence of surface friction on the wind in the ABL.

The vertical profile of horizontal wind speed is strongly influenced by the interaction between the ABL and the Earth's surface. The change in wind speed with height above ground is largely defined by the reduction in surface drag, but also the stratification of the atmosphere plays a role. Under neutral conditions of atmospheric stability, the vertical profile of horizontal wind speed in the surface layer of the ABL can be approximated by a logarithmic increase (see Fig. 1.1c) (Barlow, 2014; Kent et al., 2017). Frictional drag on the air causes the wind speed to become very weak close to the ground in the initial $\approx 10\%$ of the ABL height, while pressure gradient forces cause the wind speed to increase with height. Hence, the vertical profile of horizontal wind speed can be expressed by:

$$\bar{u}_z = \frac{u_*}{\kappa} \ln\left(\frac{z - z_d}{z_0}\right), \tag{1.3}$$

where $\bar{u}_z$ is the mean wind speed at height z, z_0 is the aerodynamic roughness length (the height at which U_h decreases by the ground obstacles), z_d is the zero-plane displacement length height and accounts for momentum absorption by the upper level of the surface canopy, $\kappa = 0.4$ is the dimensionless von Kármán constant.

The ABL is typically in a turbulent state , driven by both mechanical and thermal processes (Stull, 1988b; Hogan et al., 2009; Barlow, 2014; Kotthaus and Grimmond, 2014). Momentum exchange between the surface and the atmosphere is influence by surface drag, while thermal buoyancy responds to the surface energy balance. The relation between thermal buoyancy and mechanically-driven turbulence describes the **stability** of the atmosphere. There are three broad categories of stability in the ABL:

- The *neutral* ABL, where mechanical turbulence predominates.
- The *unstable* ABL, dominated by thermal turbulence with enhanced vertical motions driven by buoyancy forces.
- The *stable* ABL, characterized by strong surface-driven atmospheric stratification (e.g., clear skies at night). Weak and intermittent turbulence (mostly mechanical).

Note that the vertical column of the ABL could present variations in dynamic stability, causing the formation of layers with different stability conditions (Stull, 1988a).

In meteorology, various quantities provide valuable insights into ABL dynamics (Kotthaus et al., 2023). One widely used parameter to estimate mixing processes in the ABL is the vertical velocity variance (σ_w^2), which serves as a proxy for turbulent vertical mixing (Tucker et al., 2009; Hogan et al., 2009). Under shear-driven turbulence, σ_w^2 is an effective indicator of atmospheric stability and can be used to estimate the maximum height of surface-based turbulence. For example, Tucker et al. (2009) utilized sigma profiles to estimate mixing heights over offshore sites, with strong turbulence indicated by sigma values above 0.03. However, these values can differ in continental areas, particularly over urban surfaces, which experience increased surface roughness (Theeuwes et al., 2019).

The stability of the ABL exhibits significant variations throughout the day in response to two types of processes operating at different scales: surface-atmosphere exchanges and synoptic flow patterns in the free troposphere (Banta et al., 2006; Goger et al., 2022). These stability variations determine the diurnal cycle of the vertical structure of the ABL, presenting the following major components: *the convective layer, the stable boundary layer, the residual layer, the entrainment zone and the free troposphere* (see Fig. 1.1) (Stull, 1988a; Kotthaus et al., 2023). The diurnal cycle of the ABL is primarily governed by surface-atmosphere exchanges of radiation, momentum, and sensible and latent heat. While the synoptic flow introduces spatial variations in the ABL by advection and entrainment of air masses with diverse stability conditions.

Fig. 1.1a is a representation of the diurnal evolution of the ABL vertical structure under cloud-free sky conditions over a flat terrain. During the late afternoon, as thermal forcing decreases and vertical motions subside, the turbulence in the *Convective Boundary Layer* (CBL) decays, making this layer gradually dissipate in the early evening. At night, in the absence of incoming solar radiation, and once the CBL has completely dissipated, the radiative cooling of the Earth's surface becomes predominant. This radiative effect cools the air closest to the ground, leading to the formation of the nocturnal *Stable Boundary Layer* (SBL). In the SBL, cooler and heavier air remains near the ground and the warmer air in the upper layers (Fig. 1.1b). The strength of this inversion determines the degree of decoupling between the lower SBL and the warmer air layer above the inversion height, i.e., the neutral *Residual Layer* (RL). The stronger the inversion, the greater the decoupling between these layers. The SBL and RL persist through the night until sunrise, when incoming solar radiation heats the ground, enhancing the mixing and gradually merging both layers into a new CBL.

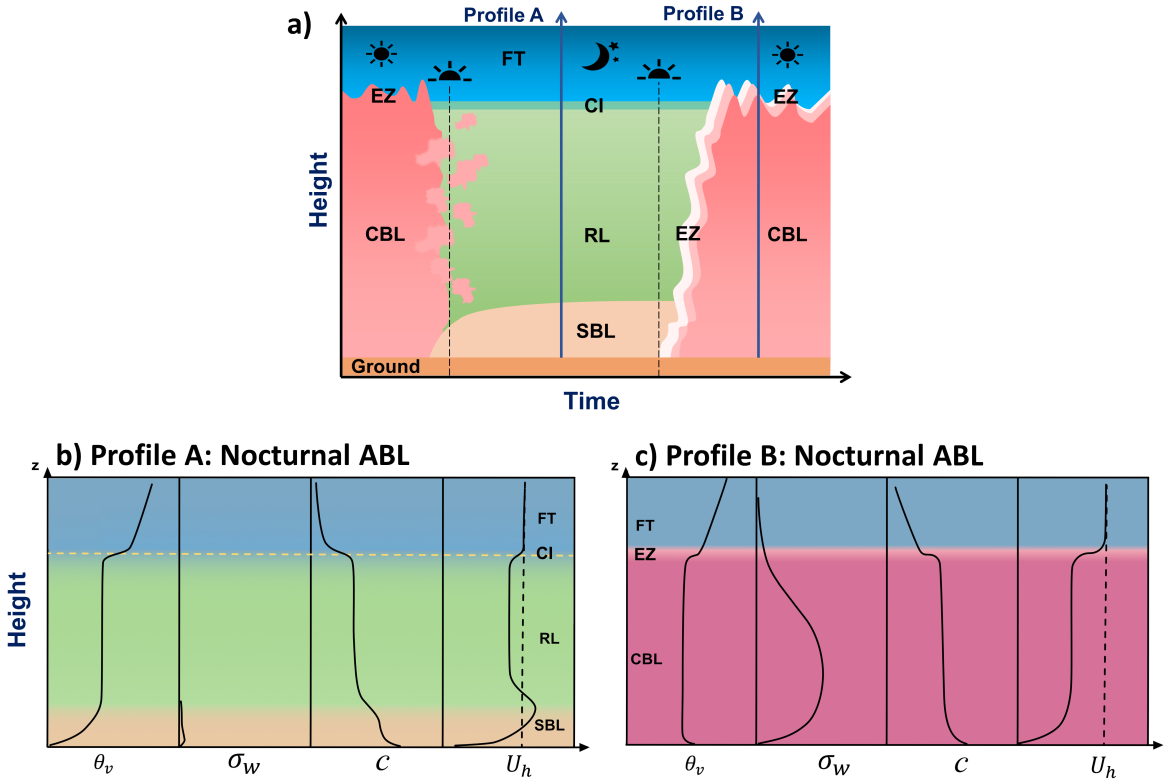

Figure 1.1 : The structure and diurnal evolution of the Atmospheric Boundary Layer (ABL). **a)** Time–height diagram for an ABL over flat terrain on a cloud-free day. Selected profiles (navy blue vertical arrows) are shown at two distinct moments and present idealised vertical profiles of atmospheric variables that are used to characterise thermodynamics (mean virtual potential temperature θ_v), dynamic and turbulent processes (vertical velocity variance σ_w, mean horizontal wind speed U_h), and resulting distributions of atmospheric tracers (mean atmospheric constituent c) during the idealised diurnal evolution of the ABL. Dashed vertical lines represent the sunset and sunrise. **b)** Profile A, nocturnal conditions with a residual layer (RL; green shading) above the stable boundary layer (SBL; orange shading) near the surface. A capping inversion (CI) separates the ABL from the free troposphere (FT; blue shading) above. The U_h profile shows the signature of a Low-Level Jet (LLJ). **c)** Profile B, early afternoon with a fully developed CBL. The entrainment zone (EZ) is a region of enhanced exchange between the CBL and the RL or FT, respectively. For both profiles A and B, the dashed vertical lines in the U_h panels represent the geostrophic wind reference, so that in profile A the LLJ presents a supergeostrophic magnitude. Adapted from Kotthaus et al. (2023).

The CBL is driven by turbulent sensible heat fluxes that develop in response to the heating of the surface through solar radiation. It begins forming in the early morning, grows throughout the day with increasing heating, and reaches its maximum height in the early afternoon (see Fig. 1.1c). At this point, the CBL extends over the entire ABL, so that the top of the CBL coincides with the top of the ABL. Vertical motions prevail in the CBL dynamics, diluting tracers such as aerosols throughout the ABL (see Fig.1.1c). At the top of the CBL, there is a stable layer called the *Entrainment Zone* (EZ), marked by an increase in absolute temperature with height. The less dense air of the EZ creates a boundary that acts like a "lid," retaining

the buoyant plumes of the CBL. At night, the upper boundary of the nocturnal RL is also subject to the temperature inversion that in this case forms the called *Capping Inversion* (CI), which retains aerosols layers below the ABL top.

The upper part of the EZ is also known as the *ABL height* and marks the boundary of the Atmospheric Boundary Layer (ABL) and the beginning of the *Free Troposphere* (FT). The FT is so named because it is no longer directly affected by the Earth's surface forcing, and aerosols remain below the ABL height. Hence, the ABL height is a relevant variable as it defines the volume of air in which heat, moisture, and pollutants are diluted in the ABL with meaningful impacts on human and environmental health.

Vertical profiles of atmospheric variables across the entire ABL provide essential information about atmospheric stability. Accurate representation of turbulence and its effects in the ABL is vital for weather forecasting, climate studies, air quality assessment, and other environmental applications. However, numerical representation of the SBL poses challenges due to weak and intermittent turbulence (Mauritsen and Svensson, 2007), model sensitivity under these conditions, and a lack of experimental data collected during SBL phases (Holtslag et al., 2013; Wouters et al., 2013). Continuous high-resolution spatial and temporal observations of the SBL are still required to improve model performance and enhance the understanding of SBL dynamics.

1.3 The Urban Boundary Layer (UBL)

Urban areas are important interfaces in the relationship between human life and the atmosphere. Due to their unique geometric and thermodynamic characteristics, cities experience a distinct micro-climate, different from that of rural areas. The urban surface alters the surface energy balance and momentum exchange, therefore modifying the structure of the ABL leading to the formation of a distinct *Urban Boundary Layer* (UBL). In conditions of very weak regional winds and cloud-free sky, the added heat and urban roughness enhance buoyancy. This can lead to the formation of an internal boundary layer, often referred to as the urban "dome," over the city. The increased buoyancy over urban areas can generate a thermally induced near-surface wind, promoting the advection of cooler air from rural surroundings. This phenomenon is known as the urban heat island circulation (Menut et al., 2000; Barlow, 2014; Oke et al., 2017b).

Fig 1.2a shows an example of the structure of the UBL during the day. In urban areas, the canopy is defined by roughness elements such as buildings (bluff bodies) and urban vegetation (porous roughness elements), this boundary is known as the *Urban Canopy Layer* (UCL). The significant landscape transformation of the UCL exerts substantial drag on the wind flow. This interaction enhances the mechanical

turbulence and forms a turbulent layer of air referred to as the Roughness Sublayer (RSL). Above the RSL is the Inertial Sublayer (ISL), where turbulent fluxes remain constant with height due to the integrated effects over a specific area of the UCL. Together, the RSL and ISL constitute the Surface Layer (SL), which typically extends to a height ranging from 1.5 to 3 times the average height of the UCL. Above the SL lies the Mixed Layer (ML), characterized by vertical motions driven by enhanced buoyancy forces. As over rural surfaces the EZ marks the region of exchange between the ML and the above residual layer or FT.

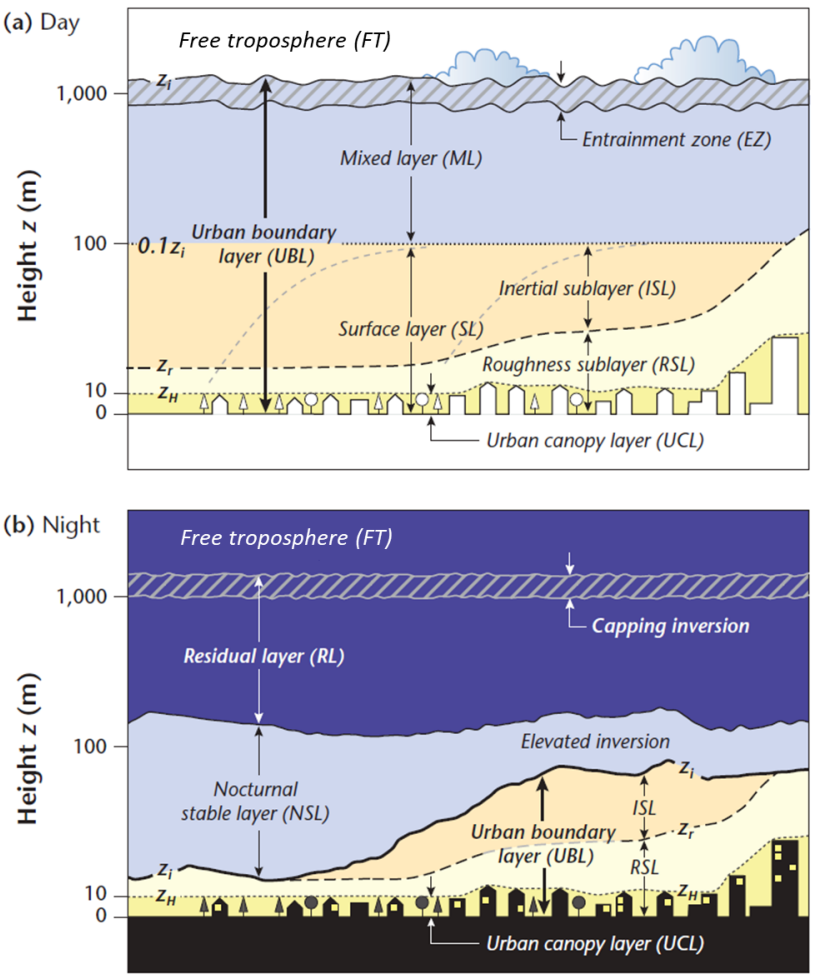

Figure 1.2 : Diagram for the structure of the Urban Boundary Layer (UBL) during a) day, and b) night. Note that in a) and b), from 10 m the height scale is logarithmic. Adapted from Oke et al., 2017b.

As over rural surfaces, radiative cooling processes have a strong impact on the atmospheric stability in the urban boundary layer. In the absence of incoming solar radiation and the surface radiative cooling process at night can exert a dominant control on the dynamic stability of the urban atmosphere. However, the geometry of the UCL and the impervious materials used in urban construction exhibit different thermodynamic properties compared to the organic land cover. This results in more efficient absorption and storage of heat in urban areas, which is gradually

released as sensible heat and thermal radiation during the night. This continued heat source means buoyancy can be maintained in the urban atmosphere even at night so that neutral or even unstable atmospheric stratification prevail over the city. Combined with the turbulent mixing induced by surface roughness, this causes the RSL and ISL to play a substantial role in the nocturnal UBL. As a result, the nocturnal UBL is typically deeper than the rural ABL due to convective motions induced by buoyancy. These differences between the urban and rural surface energy balance lead to spatial contrast of the air temperatures where cities tends to be almost always warmer during night, leading to the formation of the ***Urban Heat Island*** (UHI) effect.

The UHI is a difference in air temperature between the urban interface and its rural surroundings: $\Delta UHI = T_{Urban} - T_{Rural}$, where T_{Urban} and T_{Rural} are urban and rural air temperatures, respectively. To estimate the ΔUHI, the air temperature can be measured in the canopy layer or even in the vertical columns of the ABL and UBL. The UHI at UCL level is the most commonly studied type of UHI in the urban climate framework, given that most of the human life occurs up to the height of the UCL level. The ΔUHI is generally strongest during cloud-free nights and low wind speed conditions, following days with the same characteristics, as *cloudiness and wind* are environmental parameters that exert a strong control on the evolution of the UHI intensity.

Fig. 1.3 presents an example of the average diurnal variations of the urban and rural temperatures, as well as the ΔUHI, using data recorded by standard meteorological stations in the UCL in the Paris region between June 16 and August 31 2022. Only cloudless days were considered to ensure that the main control is attributed to the wind speed intensity. Fig. 1.3a shows that the urban temperature reaches its maximum peak between 14 and 16 UTC and then the air cools down to minimum temperatures between 4 and 5 UTC, before warming starts again just after sunrise. The rural temperature curve exhibits similar behavior, but the intensity differences between them are well-defined, with much stronger cooling rates at night, causing the UHI to peak around 4 UTC, as observed in Fig. 1.3b.

The UHI effect has been observed globally and can occur at any time of the year. However, its impact on human comfort can be much more severe during the summer in mid-latitudes due to higher temperatures and the inadequate preparedness of cities (Lemonsu and Masson, 2002; Oke et al., 2017a). The expansion of urban areas under poor ventilation and cooling design has made the UHI a prominent factor in the deterioration of the human thermal comfort (Kong et al., 2016; Li et al., 2019; Lin et al., 2022). High nocturnal temperatures increase the stress on the human body at times when it needs to rest (sleep), leading to higher mortality (Robine et al., 2008; Taylor et al., 2015; Ridder et al., 2016; He et al., 2022). While the UHI phenomenon is driven by excess heat in the built environment, atmospheric dynamics (advection, mixing, subsidence) significantly modulate the

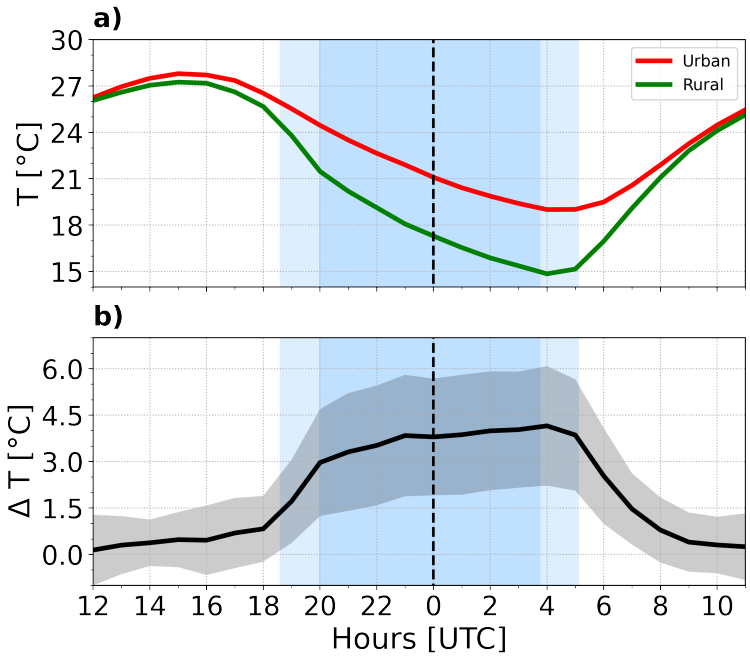

Figure 1.3 : Measurements of air temperature in the Paris region collected in the period between 16 June and 30 August 2022 for a) rural and urban environments. b) The difference between rural and urban temperature, indicating the intensity of the Urban Heat Island (UHI). The blue shadows in a) and b) represent the nocturnal period, the temporal variability in sunset and sunrise are represented by a less intense blue color.

UHI intensity (Oke, 1973; Oke et al., 2017a). Although it has been shown that each increase of $1\,\mathrm{m\,s^{-1}}$ in surface wind speed can reduce urban air temperature by up to $2\,^{\circ}\mathrm{C}$ during summer nights (Cheng et al., 2012; He et al., 2022), the effects of variations in wind profiles on the intensity of the UHI effect are still not well understood.

1.4 The Low-Level Jet (LLJ)

Atmospheric stratification in the SBL reduces the vertical transfer of momentum, causing the air in the ABL to become increasingly decoupled from the friction forces exerted by the Earth's surface. Influenced by the synoptic-scale horizontal pressure gradient, this decoupling can lead to the formation of the nocturnal ***Low-Level Jet*** (LLJ) (Baas et al., 2009). The LLJ is defined as a sharp maximum in the vertical profile of horizontal wind speed near the height of the surface-based temperature inversion, typically observed between 100 and $1000\,\mathrm{m}$ above ground level. This maximum wind, known as the **jet core**, is characterized by its *wind speed, wind direction, and height*. Usually, the maximum wind speed develops near the inversion height. If the maximum wind speed forms sufficiently above this height level, it can lead to a turbulent breakdown of the thermal stratification and the LLJ can hardly maintains throughout the night (Blackadar, 1957). The LLJ local wind speed

maximum goes along with a minimum above, which results from the perturbation of the momentum equilibrium in the ABL due to the jet acceleration (Shapiro and Fedorovich, 2010).

The LLJ is a mesoscale phenomenon with a spatial extent of up to hundreds of kilometers. Different theories about the genesis of the LLJ have been discussed over the past 60 years, which usually agree in that the formation of the LLJ requires the atmospheric decoupling of the SBL from surface drag. Once the stable stratification is established, various processes associated with mesoscale circulation can play a role in the formation of the LLJ. For example, in regions with significant changes in topography, the alternation between heating and cooling of sloped surfaces cause pressure gradients, generating horizontal forces that act upon the thermal stratification to provide the acceleration required for the LLJ formation (Holton, 1967; Parish and Oolman, 2010; Parish et al., 2020). The LLJ has also been widely observed in coastal regions, where it is generated due to land-sea breezes interactions (Dieudonné et al., 2023; Tuononen et al., 2017). The jet formation can also be associated with synoptic-scale changes in weather patterns (Sánchez et al., 2022b) and the formation of tropical cyclones (Kotroni and Lagouvardos, 1993).

At peak development, the LLJ can reach *supergeostrophic* wind speeds, i.e. it can be stronger than the geostrophic wind. Therefore, the LLJ is associated with strong vertical variation in horizontal wind speed (*horizontal wind shear*). The wind shear is an efficient source of mechanical turbulence that depends on the core height and speed (Wiel et al., 2010). While the maximum wind shear of the LLJ occurs at the core height, the region with the most mechanical turbulence production has been observed below the jet core, associated with a potential increase in TKE and downward turbulent transport of momentum (Banta et al., 2002; Banta et al., 2003), a phenomenon which has also been demonstrated in wind tunnel experiments (Ohya et al., 2008).

The LLJ induced downward transport of momentum can produce significant alterations to the momentum and greenhouse gas fluxes in the nocturnal boundary layer (Karipot et al., 2008; Brunsell et al., 2021; Duarte et al., 2015). It also impacts near-surface atmospheric processes in urban environments, such as the UHI effect (Hu et al., 2013; Lin et al., 2022). While variations in surface winds can influence UHI intensity, only a few studies in urban areas have investigated the relationship between advection caused by the nocturnal LLJ and the UHI. The few studies conducted in cities worldwide (Kallistratova and Kouznetsov, 2012; Kallistratova et al., 2013; Hu et al., 2013; Lin et al., 2022; Sánchez et al., 2022a) have found a negative correlation between UHI intensity and the wind speed generated by the LLJ core. Although these studies have advanced our understanding of the LLJ impact on UHI, they were limited by a few number of radiosonde observations in a few case studies. Therefore, continuous wind profile observations with high spatial

and temporal resolution are still needed, as the characteristics of the LLJ have their own nocturnal evolution, which affects UHI intensity in different ways.

The LLJ characteristics also present a nocturnal evolution, which is strongly associated to the formation mechanism of the LLJ. Provided a certain synoptic scale pressure gradient, a LLJ can also form over flat and relatively homogeneous terrain through the **Inertial Oscillations (IO)** mechanism. Blackadar, 1957 described the IO in his pioneering theory as an undamped oscillation around the geostrophic wind vector near the elevated nocturnal temperature inversion height (see Appendix A).

1.5 ABL wind observations

1.5.1 The Wind Profiling

The vertical profile of the wind field (speed and direction) stands out as one of the most critical variables in the atmospheric sciences, it influence significantly the cloud dynamics, pollutant dispersion and weather patterns (Johansson and Chen, 2003; Stoffelen et al., 2020). The vertical structure of the wind field exhibits high variability, with distinct different behaviour between day and night, and undergoes significant alterations upon interaction with rural or urban environments. It is crucial as input for implementing high-resolution Numerical Weather Prediction (NWP) models, energy transport, and dispersion models for air quality and pollutant dispersion studies, as well as regional or global climate models for climate change evaluation. However, despite its importance, wind profiling remains inadequately addressed, with limited spatial coverage of measurements, especially over urban areas (WMO, 2018). This inadequacy arises from various factors, including technical limitations, challenges in physical implementation, and the high spatial variability of the wind system (Rennie et al., 2021).

Historically, wind profiling has primarily been achieved using radiosondes (Blackadar, 1957). While this in situ profiling method provides valuable information about the atmospheric column, its temporal frequency is insufficient to capture the diurnal evolution of the wind profile, producing only one profile per launch. Additionally, these ascent balloons are horizontally transported, affecting the measurements through the spatial and temporal variability of the wind field, which poses a challenge for interpretation. Despite these limitations, radiosounding has been an indispensable method for observing the LLJ in the wind profile.

Another traditional measurement approach to capture the wind profile is the installation of anemometers on tall towers (Foken and Bange, 2021). Unlike radiosounding, this approach provides super high frequency and continuous observation of all three wind components which is beneficial for turbulence observations, but presents physical limitations. For instance, the physical

installation of the tower requires substantial economic and technical resources and can be challenging in urban environments. The height of the tower is limited, and only a few anemometers are installed, reducing the spatial resolution and maximum height range of the wind profile product.

Advancements in ground-based remote sensing technology over the past few decades have introduced powerful instruments designed to bridge the temporal and spatial resolution gap in atmospheric monitoring. The high temporal and spatial resolution profiling offered by the remote sensing instruments enables a detailed monitoring of the wind and turbulence profiles throughout the daily cycle. For exmaple, the SODAR (Sonic Detection and Ranging) is a ground-based active sensor that uses sound pulses to scan the atmosphere, capturing wind data within $20\,\mathrm{m}$ above the instrument (Emeis, 2021). It effectively monitors the nocturnal dynamics and seasonal variations of the wind profile but measurements can be affected by precipitation, humans and animals, but the main limitation is that it is perceptive to background noise which makes it challenging to have sufficient signal-noise-ratio in levels beyond about $1\,\mathrm{km}$ (Lehmann and Teschke, 2008), limiting its use to certains rural areas. Another example is the Radar Wind Profilers (RWP), which use high-frequency electromagnetic radiation and Doppler techniques, offer vertical resolution between 100-$400\,\mathrm{m}$ and can operate in all weather conditions. RWPs are less expensive and are suitable for example for detecting the LLJ but have limitations, such as a blind zone below $500\,\mathrm{m}$ (Michael H. Jain and Stensrud, 1990; Kalapureddy et al., 2007). However, both SODAR and RWP face challenges due to their large size and deployment requirements, necessitating isolated areas and fixed ground installations, and offer a wind profile product with a limited maximum height range (Kotthaus et al., 2023).

The Doppler Wind Lidar is a relatively recent development in compact active remote sensing with potential to improve the quantitative knowledge of the ABL dynamics (Illingworth et al., 2019; Cimini et al., 2020; Kotthaus et al., 2023). It emits infrared light and uses the Doppler shift to capture the radial velocity of the wind (Wiegner, 2012). A combination of radial velocity observations along multiple line-of-sights can be used to derive the vertical profile of horizontal wind speed and direction, as well as the vertical velocity. The Doppler Wind Lidar offers high spatial ($15\,\mathrm{m}$) and temporal resolution ($1\,\mathrm{s}$), with a dynamic maximum range from hundred of meters up to approximately $10\,\mathrm{km}$, depending on the model of the isntrument. It has a blind zone that varies between approximately 30 to $200\,\mathrm{m}$ and it is twice the spatial resolution of the sensor. The Doppler Wind Lidar measures the wind speed in the direction of the lidar beam, termed the radial wind speed, which can be used to reconstruct the horizontal wind speed and direction. When pointed at the zenith, it directly measures the vertical wind speed (see Section 1.5.2). Depending on the sampling time and frequency, turbulence quantities can also be derived (Sathe et al., 2011). For these reasons, this sensor has become prominent in the wind profiling

field in recent years, attracting particular attention for LLJ studies.

This compact sensor is almost always unattended and much easier to deploy compared to SODARs or RWPs, even being suitable for deployment on rooftops of buildings (Céspedes et al., 2022). Due to its physical characteristics, high temporal and spatial resolution, and relatively easy handling and operation, this sensor has quickly gained worldwide users. This widespread adoption has resulted in a large number of instruments, facilitating instrumental comparison and improving spatial coverage. However, adverse weather conditions such as rainfall, clouds and fog decrease the availability of the measurements since the atmospheric transmittance of the laser is reduced mostly to the region below the clouds (Thobois et al., 2018).

1.5.2 The Doppler Wind Lidar (DWL)

Lidar (Light Detection and Ranging) is an active remote sensing instrument based on laser technology, widely used for atmospheric profiling. Every lidar system consists of three fundamental components: emitter, receiver, and detector. The lidar emits electromagnetic radiation that interacts with the atmosphere, gets scattered, and is then collected by an optical system, typically composed of optical fibers connected to a telescope. The light captured by the telescope passes through a photomultiplier tube, a light-to-voltage transducer, which converts the signal into a current that is transported to the detector. The detector typically consists of a time correlated single photon counting system, which synchronizes the emission and reception frequencies of each laser pulse, creating a signal that reconstructs an atmospheric profile (Wiegner, 2012).

The emitter component of a lidar system can be either a continuous or pulsed laser, but pulsed lasers are necessary to achieve "Detection and Ranging" and to generate a range-resolved profile with a specific vertical spatial resolution (Reitebuch and Hardesty, 2021). As laser pulses are emitted at a defined frequency, the backscattered light is collected and transmitted to the detector, where it is recorded as a time-resolved signal. However, lidar signals do not always provide a complete representation of the atmospheric profile. At near ranges, the signals are affected by perturbations due to the incomplete overlap between the optical axis of the emitted laser beam and the optical axis of the telescope's Field Of View (FOV), causing the lidar system to be "blind" in the near range, where the signal consists primarily of instrumental noise. This limitation is known as the *blind zone* effect (Yin et al., 2023; Comerón et al., 2023). The optical setup of most commercial DWLs is typically designed to achieve a minimum blind zone range that is usually twice the vertical spatial resolution.

To measure variables of the atmosphere, the lidar emits light in the ultraviolet, visible, and infrared regions. The emission wavelength depends on the target, typically ranging between 0.355 and $1.5\,\mu\mathrm{m}$. Most of the DWLs use pulsed lasers

with an emission wavelength (λ_0) of $1.5\,\mu\mathrm{m}$ due to several advantages in this near-infrared spectral region: $i)$ the emitted light is primarily backscattered by aerosols and cloud droplets (Pearson et al., 2009), $ii)$ interaction with air molecules is negligible, ensuring high atmospheric transmission (Turner et al., 2016), and $iii)$ eye safety (Thobois et al., 2018).

The DWL measures the wind field using the Doppler shift in the frequency of light backscattered by aerosol particles in the atmosphere, as these particles are small and light enough to act as tracers. The DWL operates by splitting the time-resolved signal into intervals called range gates, which correspond to measurements at specific distances from the instrument (range-resolved). The size of the range gate determines the measured volume along the beam direction. Larger range gates can results in profiles with higher altitudes but result in coarser spatial resolution. Range gate lengths typically range between $20\,\mathrm{m}$ and $200\,\mathrm{m}$. Spectral analysis is performed on the signal within each range gate to obtain the Doppler frequency shift (Δf). To smooth out random noise, several laser pulses are accumulated and averaged for each measurement. Longer accumulation times improve data quality but increase the duration for each sampling interval. The accumulation time typically ranges from a few hundred milliseconds to $2\,\mathrm{s}$. This process provides the particle velocity in the direction of the line of sight (LOS), called the radial velocity, v_r. Hence, the v_r measured from a pulse of light emitted with a speed c (speed of light) and a frequency $f_0 = c/\lambda_0$ is:

$$v_r = \frac{c}{2f_0}\Delta f. \tag{1.4}$$

The v_r is volumetric projection of the wind vector $(\vec{u}, \vec{v}, \vec{w})$ along the propagation path of the laser beam or LOS (Liu et al., 2019). The spatial resolution of this projection is determined by the pulse width and the range lenght (Thobois et al., 2018). Latest versions of DWL can measure the wind components $(\vec{u}, \vec{v}, \vec{w})$ with different spatial and temporal resolutions, by covering a wider volume of the air which varies depending of the maximum range (up to $10\,\mathrm{km}$) and the scan pattern.

DWL Scan Patterns

The most significant technological advantage of DWL over other wind measurement instruments is its ability to scan the 3D wind field within a dynamic volume defined by the height of the ABL and the maximum range of the instrument. Advanced commercial DWLs can scan the wind field using different patterns, defined by the azimuth angle (θ) and the elevation angle (ϕ). Scan patterns are classified by their Degrees of Freedom (DOF), i.e. the variation of scan angles (Liu et al., 2019).

A zero-DOF pattern is defined by both angles constantly set to a fixed value. The most common use of the fixed scan is the *vertical stare*, which involves pointing the laser beam vertically towards the zenith at $\phi = 90°$. As the DWL measures the radial velocity, it can directly be interpreted as the $\vec{w}$ wind component (Wulfmeyer and Janjić, 2005). If this stare sampling is conducted at a sufficiently heigh frequency and duration, the σ_w^2 can be obtained. This parameter characterizes the variability of the intensity of turbulence in the vertical wind and serves as a proxy for vertical mixing (Hogan et al., 2009), a variable that provides valuable insights into ABL dynamics, especially in urban areas where vertical motions dominate within the CBL (Bonin et al., 2015, 2018).

Among the scan patterns with one-DOF are the Plan-Position Indicator (PPI) and the Range Height Indicator (RHI), the latter has been used for UBL studies (Ng and Hon, 2022), but is not utilised here. The PPI is a conical scan where ϕ remains constant while θ varies in discrete positions with a certain angular resolution, covering either a full cone (i.e. full $360°$) or a sector of the circumference (i.e. less than $360°$). The PPI measures the radial velocity in a horizontal plane often parallel to the surface, enabling the reconstruction of horizontal wind components. Methods for this reconstruction include the Velocity Azimuth Display (VAD) (Teschke and Lehmann, 2017) and the Volume Velocity Processing (VVP) (Waldteufel and Corbin, 1979). VVP is the basis for the volume wind algorithm, which reconstructs the 3D wind field using multiple PPI at different ϕ and θ (Thobois et al., 2015) and has been applied in coastal city wind profile studies (Filioglou et al., 2022).

The *Doppler Beam Swinging* (DBS) is a two-DOF scan pattern widely used to capture the vertical profile of horizontal wind. It involves a dynamic scan pattern consisting of at least three up to six tilted LOS at fixed ϕ towards different θ (Lane et al., 2013; Newman et al., 2016). A common variation employs five LOS, including one vertically oriented LOS ($\phi = 90°$). In this study, two DWL using the DBS scan are employed, each with a different scanning pattern. The Vaisala WindCube Scan 400s uses a five-LOS DBS pattern that includes one vertically oriented LOS and four tilted LOS ($\phi = 75°$). The entire scan can be completed in approximately $15\,\mathrm{s}$, with an integration time of $1\,\mathrm{s}$ per LOS. In contrast, the Vaisala WLS70 performs a four-LOS scan pattern that includes the tilted LOS but omits the vertically oriented LOS. This scan is completed in about $10\,\mathrm{s}$, with $1\,\mathrm{s}$ of integration time per LOS. Each DBS cycle from both instruments produces a single vertical profile of horizontal wind speed and direction. The DBS method is particularly valuable in urban environment studies due to its rapid operation, which allows for capturing unstable flows (Pearson et al., 2009). For this reason, DBS was employed in this study to capture the horizontal wind profile.

1.5.3 Detecting the LLJ

Blackadar (1957) introduced a pioneering and elegant theory to describe the LLJ phenomenon and its formation mechanism. He also developed the earliest quantitative method to detect the LLJ in radiosonde wind profiles. According to this method, a LLJ is detected in the wind profile if there is a significant maximum wind speed below $1500\,\mathrm{m}$ that exceeds the next higher minimum by $2.5\,\mathrm{m\,s^{-1}}$. Later, Stull (1988a) proposed that a LLJ is characterized by a maximum wind speed in the lower troposphere (between 100-$1500\,\mathrm{m}$) that is at least $2\,\mathrm{m\,s^{-1}}$ greater than the minimum speed above and below it. Both methods are using absolute wind speed criteria for the detection, so they are classified into the *absolute criterion* method.

As the LLJ is a phenomenon observed worldwide (Banta et al., 2002; Tuononen et al., 2015; Zhang et al., 2019; Builes-Jaramillo et al., 2022), later studies identified that synoptic flows and surface characteristics such as topography and land cover can affect the LLJ formation and its core characteristics (Karipot et al., 2009). Indeed, a LLJ can form even under weak flow conditions (e.g., $2\,\mathrm{m\,s^{-1}}$), which would be undetectable using the absolute criterion defined by Stull (1988a). This led to the development of new methods based on *relative criteria*, which allows for the detection of a LLJ in the wind profile when the maximum wind speed is, for example, at least 20% greater than the minimum speed above and below it (Baas et al., 2009; Tuononen et al., 2015), making the methods using relative criteria more suitable for the detection of weak LLJ.

These methods are effective to identify a LLJ in a single wind profile at a time, e.g. captured by a radiosonde. Studies using radiosonde profiles for LLJ detection often face several logistical challenges because multiple balloon launches must be scheduled each night (Sánchez et al., 2022b). This process requires the deployment of instruments in the field and sometimes the mandatory presence of people at the study site. Hence, the temporal resolution of radiosonde observations is mostly insufficient for the continuous monitoring that is required to study the diurnal cycle or even night-to-night variability of a persistent phenomenon like the LLJ.

Given the continuous operation of ground-based remote sensing profiles, more sophisticated LLJ detection methods are developed for their data, to assess not only the presence of a wind speed maximum in a single wind profile, but also the physical consistency of the event over time. In this study, LLJ detection is performed on vertical profiles of horizontal wind speed recorded by two DWLs. The method, based on the approach developed by Tuononen et al. (2017), considers that a consistent LLJ event lasts at least $2\,\mathrm{h}$ and it applies relative and absolute criteria to each individual vertical profile of wind speed. Later, in a second step, the algorithm assesses whether consecutive profiles detected as LLJ exhibit sudden changes in core wind speed, core wind direction or core height, and if there is sufficient temporal continuity between the profiles.

1.6 Research questions and thesis context

Important open questions related to surface-atmosphere exchanges involve the interactions between ABL winds and the urban environments (Barlow, 2014; Kent et al., 2017; Tsiringakis et al., 2022), particularly at night when the stable boundary layer exhibits greater complexity (Holtslag et al., 2013). Urban environments, due to their unique thermodynamic and geometric properties, respond differently to airflow interactions depending on the scale (Oke et al., 2017b). For instance, the interaction between urban areas (enhanced surface roughness) and mesoscale circulations such as the LLJ, so far received relatively little attention (Barlow et al., 2014; Tsiringakis et al., 2022). This is partly due to the lack of experimental data, given the challenges associated with conducting ABL profiling in urban settings (Filioglou et al., 2022; Fenner et al., 2024).

These interactions are twofold. On the one hand, the nocturnal LLJ influences urban ventilation (Ng, 2009), cloud dynamics and coherent structures in the atmosphere (Cheliotis et al., 2021), pollutant dispersion (Wei et al., 2023), and heat distribution (Hu et al., 2013; Barlow et al., 2014; Lin et al., 2022), on the other hand, urban processes can influence the LLJ (Barlow et al., 2014; Tsiringakis et al., 2022). Due to the importance of heat as a critical risk factor in many cities such as Paris (Lemonsu and Masson, 2002; Lemonsu et al., 2024a), this thesis investigates the implications of those dynamic interactions on near-surface air temperature distributions.

Acquiring quantitative knowledge on these interactions is crucial, as the LLJ is a common nocturnal phenomenon worldwide and through advection and turbulent mixing affect the ABL dynamics (Banta et al., 2002; Banta et al., 2003; Banta et al., 2006; Duarte et al., 2015), with implications for both human health and anthropogenic activities. The formation of the LLJ and UHI over the course of the night can has implications for the human health due to heat risk. Haeffelin et al. (2024) found that nocturnal mixing associated with LLJ is an important factor to consider in the design and implementation of heat mitigation measures.

Based on the scientific background and the challenges outlined above (Sections 1.1 - 1.5), this thesis is guided by the following overarching research question:

How does the Low-Level Jet interact with the summertime Paris urban atmosphere?

To face such a challenging overarching question the research objectives are intended to answer the following specific questions:

1. ***How to design a scan strategy for DWL observations to monitor the LLJ characteristics?***
2. ***What are the characteristics of the LLJ in the Paris region during summer?***
3. ***What is the impact of LLJ dynamics on the nocturnal urban heat island?***
4. ***How do topography and urban atmosphere impact the LLJ?***

To address these questions, this thesis utilizes two DWLs manufactured by Vaisala: the WindCube Scan 400s, installed at the QUALAIR-SU site, in the center of Paris, and the WindCube WLS70, installed at the SIRTA observatory in the southwestern suburbs of the city. Observations collected during the summers of 2022 (from June 15 to August 31) and 2023 (from June 1 to September 30) are exploited to achieve the stated research objectives, through the following key activities:

1. Installation of the WindCube Scan 400s on the roof of the Zamansky tower (Sorbonne Université) in the city center.
2. Definition of a suitable scanning strategy to perform continuous observations of wind and turbulence profiles with high temporal and spatial resolution.
3. Implementation of an automatic algorithm to detect the nocturnal LLJ and its core characteristics.
4. Assessment of the relationship between the LLJ and the UHI.
5. Assessment of the role of the topography and urban ABL on the spatial variability of the LLJ characteristics detected at both the SIRTA observatory and the city center.

Since this doctoral research has been conceived and motivated to face the critical challenges of the urban climate mentioned above, the intervention of diverse social actors is essential for ensuring that the development and outcomes of this project have a meaningful impact and practical application for society. Hence this thesis has been established in the context of multiple projects and collaborations.

This research topic is particularly relevant and of interest to both the Paris and French authorities, given their commitment to the Paris Agreement (Climate Change, 2015) to face climate change by developing strategies for adaptation and mitigating its global impacts. An additional motivation derives from organizing and hosting the Paris 2024 Olympic Games. In response to these scientific needs, IPSL laboratories, CNRM and other research laboratories launched the PANAME initiative[1] (Lemonsu et al., 2024b). The PANAME initiative aims to improve the synergy between modeling studies and monitoring activities in the Paris region, and

[1] PAris Region Urban Atmospheric Observations and Models for Multidisciplinary Research

one critical requirement is the availability of continuous observations of the vertical structure of the urban atmospheric boundary layer at high spatial and temporal resolutions, including the wind and turbulence profiles.

Under this requirement, various national and regional actors, such as the DIM QI2 (funded by the Île-de-France region), OBS4CLIM PIA3, and ACTRIS-France and CNRS-INSU programs support, financially supported the acquisition a new Vaisala WindCube Scan 400s wind Doppler Lidar to be utilized not only in this doctoral research, but also to conduct permanent observations in the Paris region. This is how the scientific-industrial cooperation between the SIRTA-LMD of the Institut Polytechnique de Paris and the company Vaisala France (formerly called Leosphere) was born. This cooperation allowed for gaining the required technical knowledge to precisely operate the DWL to produce and consolidate a dataset of wind and turbulence profiling observations.

This is how this thesis has been conducted within the framework of the DYNAMICS project, which is part of the broader PANAME initiative. As suggested by its name, the DYNAMICS project focuses on understanding the spatial dynamics (both vertical and horizontal) of the atmospheric boundary layer in the Paris area. ABL dynamics is a key topic in active research fields at SIRTA (Dupont et al., 1999; Haeffelin et al., 2005), such as fog and cloud dynamics (Noel et al., 2006; Wærsted et al., 2017; Toledo et al., 2021; Dione et al., 2023), air quality (Dupont et al., 2016; Foret et al., 2022), atmospheric aerosols (Bedoya-Velásquez et al., 2019) and more recently in the field of urban meteorology that has emerged as a significant research focus for the team (Kotthaus et al., 2023). The thesis work also contributed to the experimental work and scientific analyses of the ANR project Heat and Health in Cities (H2C), also a component of the PANAME initiative, focusing on the study of the spatio-temporal variability of the Paris urban climate (Lemonsu et al., 2024a).

Aspects related to study area, instruments and experimental setting, scanning strategies, and data collected are presented in Chapter 2. Chapter 3 focuses on the description of the LLJ characteristics, its nocturnal temporal evolution, and how those characteristics modulate the intensity of the UHI. The spatial variability of the LLJ characteristics, driven by the topography features and the dynamic stability of the urban ABL is discussed in Chapter 4, which is the on-going work for a scientific paper to be submitted. Finally, Chapter 5 provides a summary, concluding remarks and future work derived from this thesis.

Chapter 2

Instruments, data and methods

Contents

This chapter aims to guide the reader in understanding the instruments, data, and methodologies used to address the research questions that shape this doctoral thesis (Chapter 1). Two types of measurements are exploited: DWL observations of wind and turbulence profiles, and meteorological surface stations data of wind and air temperature.

The chapter is organized into four main sections: the first section describes the study area and the synoptic conditions during the study periods. The second section outlines the strategy for conducting DWL measurements, introducing the instruments, their operation, data evaluation, and the development of an appropriate scan strategy for measuring wind and turbulence profiles in the region. The third section details the methods for analyzing the DWL profiles, focusing on techniques for detecting the LLJ and quantifying turbulence. Finally, the fourth

section describes the methods used to determine the spatial variation of heat in the Paris region, based on data collected from meteorological stations within the Météo-France network.

2.1 Study area and study period

The study area is the Paris region in France (administratively called Île-de-France). Fig. 2.1 shows the regional topography, with the administrative boundaries of the Paris city, the Île-de-France region, and the experimental sites. The terrain is mainly defined by the Seine River basin and plateaus, which exhibit modest topographic variation, rising no more than $300\,\mathrm{m}$ above sea level (asl). Due to its distance from the sea ($\approx 175\,\mathrm{km}$), this area is not influenced by sea breezes.

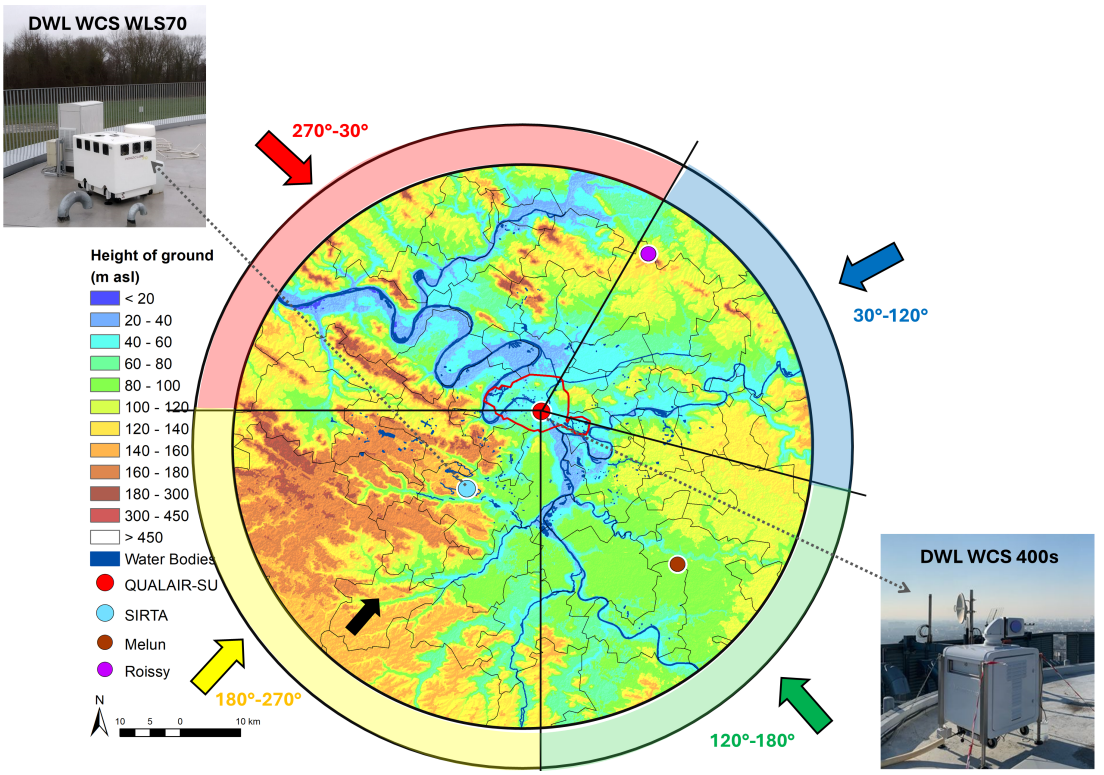

Figure 2.1 : Topography in the Île-de-France, France (ESA, 2023), with the location of the experimental sites along a suburban-urban-suburban transect. The red dot marks the location of the Doppler Wind Lidar (DWL) WindCube Scan (WCS) 400S at QUALAIR-SU (urban site), the blue dot marks the location of the DWL WCS WLS70 at SIRTA (suburban site), the magenta dot represent a suburban PANAME supersite located in a suburban setting at Roissy, not utilized in this study, and the brown dot is a Météo-France meteorological station located in the rural area of Melun. The inner black arrow indicates the prevailing southwesterly regional wind direction. The external colored polygons and arrows indicate the wind direction sectors selected for evaluation in this study (See Section 4.3.2). The red border indicates the administrative boundary of the City of Paris, while the black polygons represent administrative borders within the Paris region.

The urban agglomeration of the Paris region has a population of over 12 million people. The urban surface is mainly characterized by a topography with relatively flat terrain, with the lowest altitude at about $20\,\mathrm{m\ asl}$ along the river that crosses the city from southeast to northwest. However, in the northern parts of the city (red border in Fig. 2.1) there are hills with altitudes at about $130\,\mathrm{m\ asl}$. In constrat, the southwest suburban area is characterized by the Paris-Saclay Plateau, located approximately $12\,\mathrm{km}$ southwest of the city. This plateau has a mean extension of $10\,\mathrm{km}$, an average elevation of about $160\,\mathrm{m\ asl}$, and a maximum elevation of $180\,\mathrm{m\ asl}$.

To give some context of the overall synoptic flow conditions during the study period, Fig. 2.2a presents the wind roses of surfaces wind observed in central Paris, focusing exclusively on nocturnal winds. The data collected at the Montsouris station in central Paris ($48.82°$N; $2.33°$E; $10\,\mathrm{m\ agl}$) is provided by the ReOBS project (Chiriaco et al., 2018), which compiles a comprehensive dataset of environmental variables in the region using measurements collected by the SIRTA observatory and the Météo France surface meteorological network. The two predominant long-term wind directions in the area are from the southwest ($170°$-$225°$) with air from maritime origin and from the northeast ($0°$-$45°$) with winds with more continental influence (Haeffelin et al., 2005; Pal et al., 2012). The prevailing nocturnal winds exhibit a range of speeds below $8\,\mathrm{m\,s^{-1}}$.

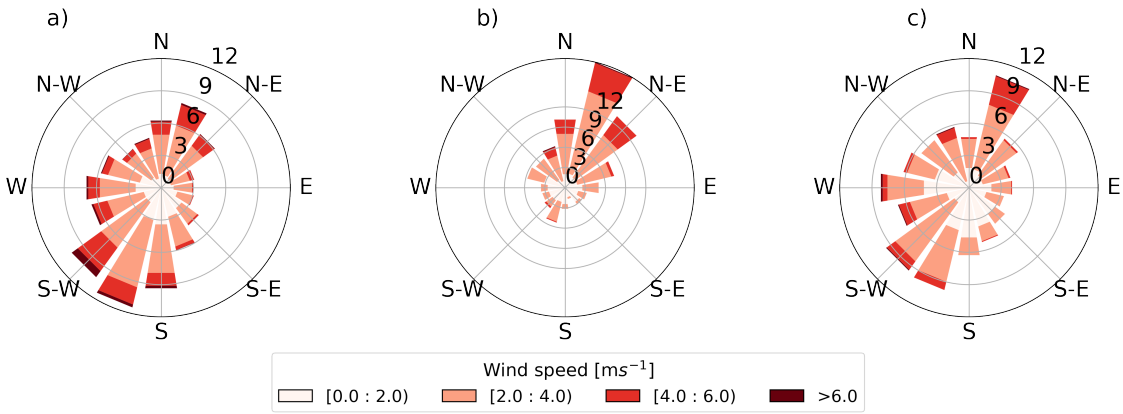

Figure 2.2 : Wind roses indicating the direction and speed of the predominant flow in the study area at night (between sunset and sunrise), defined for the following periods: a) 2014 to 2024, b) June to August 2022, and c) June to September 2023. Data is sourced from the ReOBS project (Chiriaco et al., 2018).

This study focuses on two periods: the summer of 2022, from June 15 to August 31, and the summer of 2023, from June 1 to September 30. Fig. 2.2b presents the wind rose for the summer of 2022 again focusing exclusively on nocturnal winds. During this period, the prevailing winds were from the northerly to northeasterly directions ($0°$-$75°$) with speeds up to $6\,\mathrm{m\,s^{-1}}$, and almost no winds from the southwest. The year 2022 was recorded as the warmest observed in France so far, with three reported heat waves between June and August, severe conditions were observed

especially in the July heat wave, where sea-level temperature anomalies above $12\,^{\circ}\mathrm{C}$ were associated with a deficit in precipitation rate of about 80%, leading to extreme droughts (Petit et al., 2023). Therefore, this environmental conditions lead to this exceptional synoptic conditions over the Paris region during summertime.

Fig. 2.2c presents the wind rose for the summer of 2023 again only for nocturnal winds. In contrast to the summer of 2022, during this period, the synoptic winds were similar to the overall wind climatology (Fig. 2.2a), with prevailing winds from both the southwest and northeast directions and speeds up to $6\,\mathrm{m\,s^{-1}}$.

2.1.1 The Paris region ground-based remote sensing network

A dense ground-based remote sensing network contributes to the PANAME initiative, multiple DWLs for observing the wind and turbulence profiles, Automatic Lidars and Ceilometers (ALCs) for detecting cloud base heights and profiling aerosol backscatter, and Microwave Radiometers (MWRs) for profiling air temperature (Lemonsu et al., 2024b). Three experimental supersites equipped with all three sensor types are situated along a suburban-urban-suburban transect, aligned with the predominant southwest-northeast wind direction. Fig. 2.1 presents the localization of these three supersites across the Paris region and shows pictures of the two DWL used in this thesis, at the suburban SIRTA observatory and the QUALAIR-SU site in central Paris (Section 2.2.1).

The third site is located in a suburban area at Roissy (49.016°N; 2.533°E; $112\,\mathrm{m}$ above sea level), northeast of the city center (see magenta dot in Fig. 2.1). A HALO photonics DWL was operated there by the Met Office. However, data from this sensor are not utilised here. An overview on the Paris wind profile observations available in summer 2023 is in preparation by the URBISPHERE campaign, which also contributed to the PANAME initiative (Morrison et al., In preparation).

2.2 The DWL measurement strategy

This section outlines the DWL measurement strategy developed in the context of this thesis, which included the deployment, operation and assessment of a new instrument, the implementation of an automatic data flow, as well as the design of a scan strategy appropriate for multiple research objectives, including the monitoring of the nocturnal low-level jet.

2.2.1 The experimental sites: the WindCube Scan 400s and the WindCube WLS70

In the Paris city center (urban site hereafter), a high-power scanning Vaisala WindCube Scan 400s DWL (hereafter DWL WCS 400s) is installed on the roof of

an isolated tall building with a height of 88 m above ground level (agl) at the QUALAIR-SU supersite, located on the campus of Sorbonne Université (48.8°N; 2.36°E; 125 m asl; red dot in Fig. 2.1). This building stands out in a neighbourhood with an average building height of ≈20 m, representing a high-density urban surface (Local Climate Zone: Compact Midrise (Stewart and Oke, 2012; Oke et al., 2017b)).

The instrument was deployed on this building to study the effects of an urban surface with heterogeneous roughness by assessing the variability in wind profile characteristics at different sites across the city, but not only directly above the instrument. The PPI scanning mode can be used to capture those profiles after processing with the Vaisala Volume Wind tool (see section 2.2.3).

The DWL WCS 400s is equipped with a scanning head that allows it to perform radial velocity measurements measurements alternating between four different scan patterns: DBS, PPI, Fixed, and Range Height Indicator, though the latter is not used in this study. The DBS scan pattern integrated into the factory catalogue of the DWL WCS 400s consists of five LOS (Section 1.5.2). All the scan patterns can be operated under different configurations (see Table 2.1), to retrieve range-resolved wind profiles with spatial gate resolutions of 75, 100, 150, or 200 m. Every scan mode has a blind zone equal to twice the chosen spatial resolution, meaning the first available measurement occurs at 150, 200, 300, or 400 m above the instrument, respectively, for each spatial gate resolution.

Table 2.1: Characteristics of the Vaisala Doppler Wind Lidars WindCube Scan 400S (urban site - QUALAIR-SU) and WLS70 (suburban site - SIRTA).

Characteristics	**DWL WCS 400s**	**DWL WLS70**
Pulse repetition frequency (kHz)	7, 10, 20, or 40	10
Pulse width (ns)	100, 200, 400, or 800	100
Range gate resolution (m)	75, 100, 150 or 200	50
Display resolution (m)	from 1 to 6616	–
Min range (m)	150	100
Max range (m)	7000	2000
Accumulation time (s)	1 per beam	1 per sequence
Radial wind speed range ($m\,s^{-1}$)	±30	±30
Emission wavelength (µm)	1.54	1.54
Radial wind accuracy ($m\,s^{-1}$)	0.1	0.3
Lifetime in operation (years)	12	4

In addition, this instrument offers an advanced feature called *display resolution*, which results from a spatial interpolation between gates to improve the visual representation of the recorded profiles. While the range gate resolution is fixed to one of the possible physical values, the display resolution can be set to a value between 1 and 6616 m, so that the spatial resolution can be made coarser of finer

than the range gate resolution. All profiles collected by this instrument and used in this thesis have a spatial gate resolution of $75\,\mathrm{m}$ and a display resolution of $25\,\mathrm{m}$.

The Site Instrumental de Recherche par Télédétection Atmosphérique-SIRTA (suburban site hereafter) is a multi-instrumental atmospheric platform located 25 km southwest of the Paris city center ($48.713°$N; $2.208°$E; $156\,\mathrm{m\ asl}$; see cyan dot in Fig. 2.1), in a suburban setting on the campus of the École Polytechnique on the Plateau Paris-Saclay. The SIRTA observatory is operating since 2002 (Haeffelin et al., 2005), and it is equipped with a large number of instruments that continuously record various atmospheric variables. The vertical wind profile is measured by a Vaisala WindCube WLS70 DWL (hereafter DWL WLS70), which has been in operation since 2012.

The DWL WLS70 is referred to as a *wind profiler* because it only performs measurements using the DBS scan pattern, but differs from the pattern used by the DWL WCS 400s because it does not perform the vertical stare LOS (see Section 1.5.2). Despite this difference, the vertical profiles of horizontal wind measured here are considered to be comparable as both can measure with similar temporal and spatial resolutions (Table 2.1). The DWL WLS70 has been used for research on various topics, including boundary layer dynamics (Dupont et al., 2016), extreme weather and pollution (Foret et al., 2022), and the fog life cycle (Dione et al., 2023). Hence, it is here considered as a solid instrumental reference.

2.2.2 Deployment of the DWL WindCube Scan 400s

Before its installation at the urban site, the new DWL WCS 400s has been deployed at SIRTA for a testing phase of four months to conduct an initial evaluation of the instrument and to gain experience with its operation and different wind data products. The deployment procedure involves two key steps: horizontal leveling and north alignment, which ensure spatially accurate wind profile measurements, particularly for the wind direction parameter.

Horizontal leveling and north alignment

The first step of the deployment is to roughly orient the DWL towards the north using a compass. The lidar casing has a red arrow on the top that serves as an alignment guide, this should point the north. This makes the later north alignment process easier. To achieve a precise horizontal leveling, the lidar is equipped with adjustable legs and an inclinometer that measures the degree of inclination with high accuracy. According to the procedure described in the *WindCube Scan Hardware Manual*, the acceptable degree of inclination before starting the lidar operation is $\pm 0.005°$ for both *Pitch* and *Roll*, as specified by the manufacturer. However, this procedure can take time for the first time as the inclinometer is very sensitive and the target level of accuracy is high.

Once successful leveling is completed, the accurate orientation to geographical north needs to be conducted. The DWL WCS 400s system has an integrated functionality called **hard target**, which ensures a orientation accuracy within $\pm 0.5°$. This method involves using a solid object with a fixed position on the ground (e.g., a building) as a reference (target), which is localized using the PPI scan pattern. The spatial coordinates of the target are then compared with the geographical north and the system measures the angular deviation from north to the target. The angular offset values are input into the Vaisala DWL software, specifically in the *settings system* window, to correct the angular measurements and ensure accurate wind direction values. The complete procedure is explained in the *WindCube Scan Software Manual*.

DWL WCS 400s installation at SIRTA

The DWL WCS 400s is an instrument that was developed relatively recently by the manufacturer Vaisala. It was acquired in the framework of this thesis after six month of being used in previous measurements campaigns that are not related to current project. To conduct an evaluation of this instrument, it was deployed at the SIRTA facility in September 13 2021, colocated with the DWL WLS70 at a distance of approximately $120\,\mathrm{m}$. The instrument was installed on the rooftop of the newly opened building of the SIRTA observatory, at a height of $5\,\mathrm{m\ agl}$. This installation was completed with the help of a field engineer from Vaisala as part of the *Level 1 training on the WindCube Scan 400s*.

DWL WCS 400s installation at QUALAIR

The DWL WCS 400s was deployed at the QUALAIR-SU supersite on January 15, 2022. This deployment was conducted by the SIRTA team with support from the QUALAIR-SU team. Given the dimensions and weight of the lidar, the unboxing, rough north orientation, horizontal leveling, and network connection were completed on the day of installation. To ensure an accurate and stable levelling, the lidar was secured to the ground with steel wires. Fig. 2.3 summarizes the procedure of the DWL WCS 400s installation.

The DWL WCS 400s north alignment with the hard target method was completed over the course of a week testing three tall structures in Paris as hard targets: the Eiffel Tower, the Montparnasse Tower, and the Sacré-Cœur Basilica. The Eiffel Tower, located approximately $4.6\,\mathrm{km}$ away from the sensor, was selected as the hard target for final alignment. An angular offset of $353.5°$ was found and registered in the *system settings* window of the software, indicating that the initial roughly alignment was deviated off by $6.5°$ from magnetic north. The DWL WCS 400s produces a CNR map that shows the shape of the target to ensure an accurate alignment. An schematic example of the hard target CNR map is shown in Fig. 2.4.

Figure 2.3 : Installation of the Doppler Wind Lidar WindCube Scan 400s (DWL WCS 400s) on the QUALAIR-SU platform in central Paris, including a) transport and deployment on the Zamansky tower roof, b) installation, alignment, levelling, and configuration, c) secure tie-down to the platform surface, and d) verification of successful system operation.

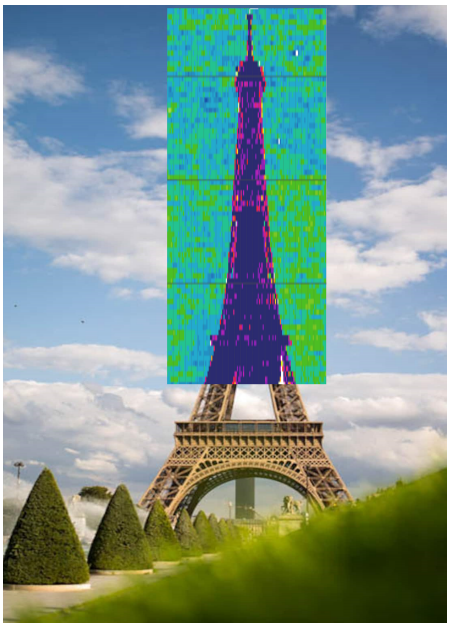

Figure 2.4 : Carrier-Noise-Ratio (CNR) map resulting from hard target alignment of the Vaisala Doppler Wind Lidar WindCube Scan 400s in the Paris city center. The CNR map is overlapping a photo of the Eiffel tower for visualization.

2.2.3 Initial evaluation of the DWL WCS 400s at SIRTA

Over approximately four months, tests were conducted with the DWL WCS 400s to master its installation, configuration, operation, automation, and the generation of easily manageable files. The first step in using this DWL model was establishing

an adequate Ethernet connection to enable file transfer to the SIRTA database. The support of qualified personnel on the team was essential, but despite this, establishing the connection was not a straightforward task. This challenge led to a dedicated team effort to create a user manual, which is now stored in the SIRTA documentation archive.

Another aspect of the operational exploration focused on gaining experience with the Vaisala DWL software, which is vital for the operation and maintenance of the instrument. Although the DWL WCS 400s has a user-friendly firmware with a graphical user- interface, a strong theoretical background is required to design an appropriate configuration and measurement strategy. One of the operational challenges is file management, as the DWL WCS 400s can generate tens of thousands of files per day creating potential issues with the file transfer and server storage capacity. To address this issue, a measurement protocol was developed to minimize the number of files generated by the lidar. These files are then processed through a concatenation routine before being stored in the SIRTA database. This concatenation routine was especially designed for this instrument and was supported by the customer service of Vaisala France, as part of the institutional cooperation.

After mastering the operational aspects of the instruments, multiple tests were conducted using the PPI, DBS, and vertical stare scanning modes. This exploratory phase also allowed for testing a computational tool called Volume Wind (VW), developed by Vaisala and based on the VVP theory (Thobois et al., 2015). The VW tool reconstructs horizontal wind from radial velocity measurements obtained using the PPI scan mode. Depending on the PPI scan configuration, it can retrieve a 3D hemispherical volume of horizontal wind information with the instrument at the origin, or selected subsets such as a 2D map or a vertical profile. For instance, a full PPI (complete circumference, see Section 1.5.2) at zero degrees elevation angle generates a 2D wind map, while multiple full PPIs at different elevation angles can reconstruct a hemispherical volume of the wind.

The VW products were compared with wind retrievals from the DWL WLS70, with the two instruments operated with a horizontal distance of less than $50\,\mathrm{m}$. From this comparison, it was concluded that the VW development was not yet sufficiently mature for application in this scientific study. The quantitative and qualitative results were reported to Vaisala France, along with a series of recommendations to improve the algorithm's performance. Vaisala has taken into account this user feedback during ongoing developments of this novel tool (Toupoint et al., 2024).

Also the DBS scan mode was evaluated at SIRTA before deploying the instrument in the Paris city center, to assess the instrument operations, retrieval results, and further determine the appropriate sampling time needed to produce reliable horizontal wind data. As part of the SIRTA data catalog, profiles of horizontal wind speed and direction are available with a temporal resolution of 10

seconds (i.e., an instantaneous measurement or one DBS cycle) and as 10-minute averaged profiles. The latter is an official SIRTA product and is widely used for scientific studies.

Evaluating the DBS scan pattern and retrieval

The DWL WCS 400s DBS retrieval was evaluated against data from the DWL WLS70. The evaluation covers the period from September 26 at 08:00 UTC to September 27 at 23:59 UTC, 2021.

As the DWL WLS70 performs the DBS with fixed parameters, including range gate resolution and a temporal resolution of $10\,\mathrm{s}$ (see Table 2.1), the configuration of the DWL WCS 400s was adjusted to produce vertical profiles of horizontal wind comparable to those recorded by the DWL WLS70. The DWL WCS 400s was operated under the DBS scan pattern with a range gate resolution of $75\,\mathrm{m}$, a display resolution of $50\,\mathrm{m}$, a temporal resolution of one cycle (i.e., $15\,\mathrm{s}$), an accumulation time of $1\,\mathrm{s}$, and a minimum and maximum range of $150\,\mathrm{m}$ and $7000\,\mathrm{m}$, respectively. Therefore, the raw vertical profiles of horizontal wind speed recorded by both instruments exhibit similar characteristics, enabling the assessment of the DWL WCS 400s DBS scan.

The first step of this assessment was to apply quality control filters to observations from both DWL systems, removing samples with a CNR > $5\,\mathrm{dB}$ to exclude regions affected by clouds and CNR < $-26\,\mathrm{dB}$ to avoid samples with weak signals or potential instrumental noise. These thresholds were recommended by the manufacturer and tested in comparison with the data produced by a Vaisala ceilometer CL31. Given that the temporal resolutions of the instruments differ, the second step was to resample the measurements by averaging the observations from both DWL systems over $30\,\mathrm{s}$ intervals to achieve the same temporal resolution.

As listed in Table 2.1, the main difference between the instruments is their maximum range of measurements. the DWL WCS 400s has a maximum measurement range of up to $7000\,\mathrm{m}$, allowing for a detailed capture of the entire ABL column. In contrast, the maximum measurement range of the DWL WLS70 is limited to $2000\,\mathrm{m}$. A preliminary qualitative evaluation (no shown here) of both wind speed and wind direction suggests a physical consistency in the recorded data for both instruments. Hence, subsequent quantitative analysis is based on the horizontal wind speed and vectorial wind components ($\vec{u}, \vec{v}$) respectively, inherently accounting for differences in wind direction.

Fig. 2.5 shows the distribution of horizontal wind speed and the horizontal velocity components $\vec{u}$ and $\vec{v}$, recorded by both the DWL WCS 400s and DWL WLS70. This analysis only considers data within the range between 150-$2000\,\mathrm{m}$ to ensure comparability. The DWL WCS 400s shows 40% higher data availability in this range compared to the DWL WLS70. While the horizontal wind speed

magnitude recorded by the DWL WCS 400s ranges between $0\,\mathrm{m\,s^{-1}}$ and $35\,\mathrm{m\,s^{-1}}$, the DWL WLS70 is limited to speeds below $25\,\mathrm{m\,s^{-1}}$ (see Fig. 2.5a). In general, both datasets exhibit similar distributions, with wind speeds mostly falling within the $0\,\mathrm{m\,s^{-1}}$ and $15\,\mathrm{m\,s^{-1}}$ range. Concerning the horizontal components $\vec{u}$ (Fig. 2.5b) and $\vec{v}$ (Fig. 2.5c), recordings from both instruments show similar distributions within the same magnitude ranges.

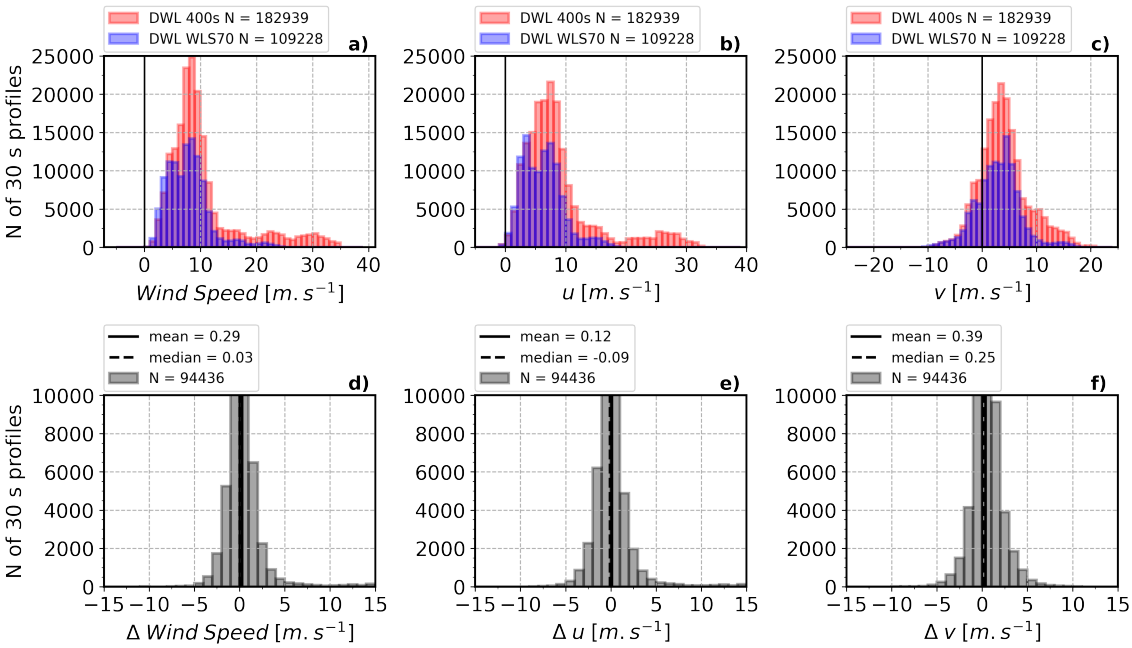

Figure 2.5 : Histograms showing the frequency of a) horizontal wind speed, b) meridional component of the horizontal wind (u), and c) zonal component of the horizontal wind (v). Red and blue bars represent data collected by the Doppler Wind Lidar (DWL) WindCube Scan 400s and DWL WLS70, respectively. Panel d) displays the histogram for the difference (Δ) in horizontal wind speed between the two instruments, while panels e) and f) show Δ for the u and v components, respectively. N stands for size dataset in terms of 30 s profiles.

Fig. 2.5d presents the difference in wind speed recorded by both instruments. The results reveal a mean deviation of $+0.29\,\mathrm{m\,s^{-1}}$, indicating that when considering the same volume of air, the DWL WCS 400s tends to record a higher magnitude of wind speed than the DWL WLS70. Differences for $\vec{u}$ (Fig. 2.5e) and $\vec{v}$ (Fig. 2.5f) exhibit a mean deviation of $+0.12\,\mathrm{m\,s^{-1}}$ and $+0.39\,\mathrm{m\,s^{-1}}$, respectively. Similar to the horizontal wind speed, these values suggest that DWL WCS 400s compares very well regarding the WLS70, even when there is a slight disparity in observing wind direction, particularly for zonal winds from east to west.

This evaluation shows that the DBS data collected by the DWL WCS 400s is in very good agreement with the data from the DWL WLS70 within the comparable range up to $2000\,\mathrm{m\ agl}$. Notably, the DWL WCS 400s demonstrates exceptional performance, measuring up to $7000\,\mathrm{m\ agl}$.

2.2.4 Designing the scan strategy

Mastering the operation of the DWL WCS 400s and exploring different scanning modes and their respective products has provided valuable insights into the potential applications of DWL observations in the Paris city center. Although this thesis focuses on studying the LLJ and its interactions with the regional surface, the implemented scan strategy aims to produce a data collection for diverse research purposes.

The operational experience improved the understanding of the instrumental limitations of the DWL WCS 400s. For instance, the blind zone can pose challenges for detecting and characterizing shallow LLJs. In the following, an adapted DBS approach is presented, which was implemented to improve observations in the blind zone of the standard DBS retrieval. A summary of the scan strategies used in this study to observe the LLJ in the Paris region during the summers of 2022 and 2023 is then provided. Given this methodological development is an important contribution of this thesis, the assessment and implementation of this novel approach are presented with the scientific results in chapter 4.

Beating the blind zone: the Shallow DBS

As described in Section 2.2.1, the DWL WCS 400s is installed on the top of the tall building ($88\,\mathrm{m\ agl}$) with a first available measurement at $150\,\mathrm{m}$ above the instrument, i.e., the first measurement gate recorded by the vertical stare and standard DBS of the DWL WCS 400s is at $238\,\mathrm{m\ agl}$. To extend the wind profile observations below this height, a novel scan pattern and wind retrieval was introduced in October 2022.

The *shallow DBS* is a variation of the standard DBS mode embedded in the WindCube Scan 400S firmware. The novel technique, developed and implemented as an experimental achievement of this thesis, is composed of 5 LOS scans using the Fixed scan mode to replicate the standard DBS but at a shallow elevation angle of $10°$. As for the standard DBS, each LOS has a physical gate resolution of $75\,\mathrm{m}$ and a display resolution of $25\,\mathrm{m}$. This configuration results in a first measurement gate located at a height of $26\,\mathrm{m}$ above the instrument ($114\,\mathrm{m\ agl}$), allowing for a downward extension of the reconstructed wind profile by $124\,\mathrm{m}$. The effective display resolution of the reconstructed vertical wind profile is $4.4\,\mathrm{m}$. Fig. 2.6 presents a schematic with the angular structure and gate heights of the standard DBS mode and the novel shallow DBS. Both the standard and shallow DBS scan sequence take approximately $15\,\mathrm{s}$ to complete, with an accumulation time of $1\,\mathrm{s}$ for each LOS ($5\,\mathrm{s}$ for all five LOS) and $2\,\mathrm{s}$ between each LOS for the lidar head rotation ($10\,\mathrm{s}$ in total). The scan strategy including the shallow DBS (operated between October 2022 - June 2024) is summarised in Fig. 2.7b.

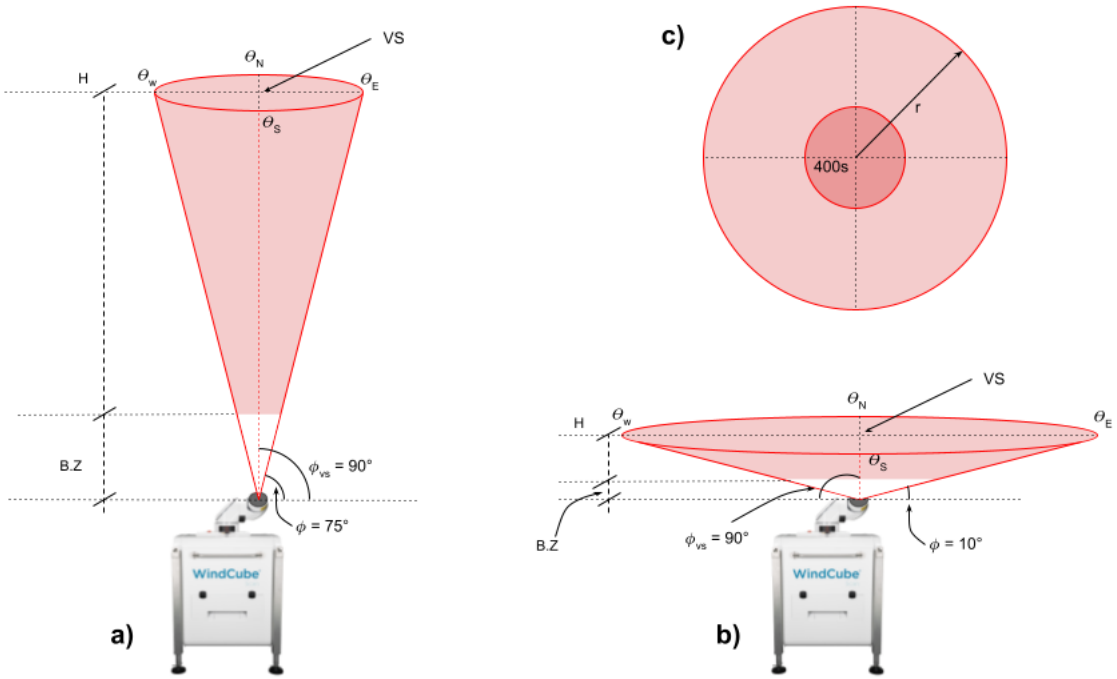

Figure 2.6 : Schematic diagram with the geometrical orientation of the vertical and tilted beams in the a) Doppler Beam Swinging (DBS) scan, and b) novel Shallow DBS scan. c) Schematic diagram in top view that represents the area scanned for both scan patterns, with the Shallow DBS scanning a greater area with radius r. For the three panels the lidar is located at the origin of the coordinate system. In a) and b): θ is the azimuth angle where N, E, S and W are north, east, south, and west respectively; ϕ is the elevation angle of the tilted beams and ϕ_{vs} the elevation angle of the vertical beam; VS is vertical stare; B.Z is the blind zone height, and H is the maximum range of measurement.

To obtain a more complete vertical profile of the horizontal wind, the results from the shallow DBS below $238\,\mathrm{m\ agl}$ are concatenated to the standard DBS profile. The shallow DBS and standard DBS product are compared up to a height of $500\,\mathrm{m\ agl}$ to evaluate the performance of the shallow DBS and consistency between the two products (see Section 4.1).

The scan strategy sampling time

Various experiments and tests were conducted between January and June 2022 to optimise the DWL WCS 400s scan strategy at the central urban site for a range of applications and requirements from the involved stakeholders of this thesis (Section 1.6). Starting from June 15th, 2022, a scan strategy was implemented that combined standard DBS, vertical stare, and PPI modes. Although this approach addressed various PANAME research objectives, it was not specifically optimized for assessing LLJ characteristics. During the study period of the summer of 2022 (15 June - 31 August), the scan strategy was designed to follow an hourly schedule (Fig. 2.7a), alternating the operation of the DBS scan with the vertical stare and PPI. In the first half of every hour the DBS is performed for $9\,\mathrm{min}$, followed by a 3-minute

full PPI at $0°$ of elevation with an angular resolution of $2°/s$, then $5\,\mathrm{min}$ of continuous vertical stare at $90°$ of elevation, followed by another $9\,\mathrm{min}$ of DBS and closing again with 3-min full PPI at $0°$. The second half of the hour repeats the same schedule. In this study, all vertical profiles of horizontal wind observations were derived from the DBS, while the vertical stare data are used to derive the vertical velocity variance (Section 2.3.2). The observations collected with the PPI mode are not exploited in this thesis, however, in the future the data can be processed using the VW algorithm (Section 2.2.3, (Thobois et al., 2015)) to study the spatial variations of the wind-field across the urban surface roughness.

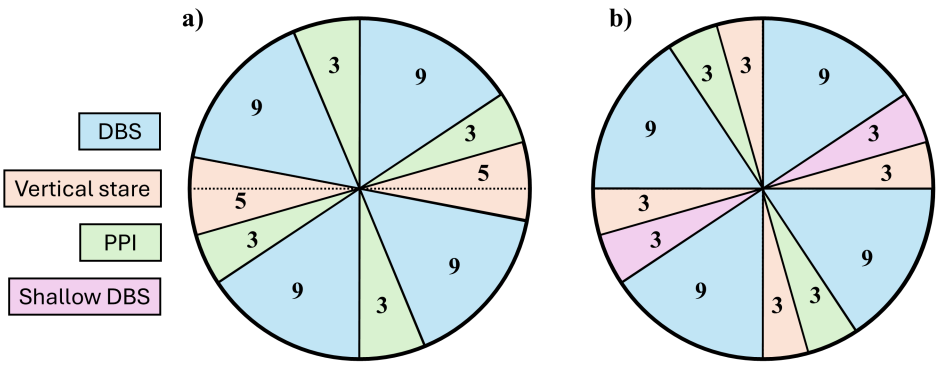

Figure 2.7 : The scan strategy implemented for the DWL WCS 400s at the urban QUALAIR-SU site in central Paris for a) 15 June - 31 August 2022, and b) 1 June - 30 Sept 2023.

As described in Section 1.5.2, the optical configuration of the DWL WCS 400s results in a blind zone of twice the spatial resolution. Since this DWL system can operate with different spatial resolutions (see Table 2.1), the blind zone varies accordingly. In this case, the spatial gate resolution used is $75\,\mathrm{m}$, meaning the vertical wind profile captured by the DWL WCS 400s begins at a height of $150\,\mathrm{m}$ above the instrument. Given that the instrument is installed on top of a tall building, the first measurement level recorded by the vertical stare and the DBS is at a height of $238\,\mathrm{m\ agl}$.

This optical configuration is limited to detecting LLJs with a core height above $238\,\mathrm{m\ agl}$. To improve the data availability below this height, the novel shallow DBS scan pattern was introduced in October 2022 (see Section 2.2.4). Data collected by this adapted scan strategy (Fig. 2.7b) were exploited to investigate the interactions of the LLJ with the regional topography and urban buoyancy (Chapter 4). In the first half of each hour, the DBS is performed for $9\,\mathrm{min}$, followed by $3\,\mathrm{min}$ of shallow DBS, $3\,\mathrm{min}$ of vertical stare at $90°$ elevation, another $9\,\mathrm{min}$ of DBS, $3\,\mathrm{min}$ of continuous full PPI at $0°$ elevation with an angular resolution of $2°/s$, and finally 3 more minutes of vertical stare. The same schedule is repeated in the second half of the hour.

2.3 Methods for DWL data analysis

This section presents the methods used for the analysis of the wind profile observations collected with the two DWLs. An algorithm for the automatic detection of the LLJ occurrence and description of its core characteristics was developed and applied to the horizontal wind profiles collected at both experimental sites using the DBS retrieval (standard DBS for 2022, concatenated product of standard + shallow DBS in 2023) (Section 2.3.1). In addition, at the urban site, data collected with the vertical stare scanning pattern were used to estimate the variance of the vertical velocity (Section 2.3.2).

2.3.1 The automatic detection of the LLJ

As described in Section 1.5.3, various methods and criteria have been developed to detect a LLJ in a vertical profile of horizontal wind. The techniques depend on the characteristics of the data source (e.g. limitations from measurement sensors) and even the study area. In this thesis, the automatic LLJ detection is an adaptation from the method described by Tuononen et al. (2017) and uses 30-min averaged profiles of horizontal wind, to best combine the 15-min data products available at QUALAIR-SU and the 10-min data products available at SIRTA. This temporal resolution was previously used in SODAR studies presenting coherent LLJ detection (Karipot et al., 2009; Baas et al., 2009; Duarte et al., 2015).

Based on the literature and exploratory tests on the data set, some important conceptual aspects were adapted compared to the original method from Tuononen et al. (2017):

- Daytime LLJ events are negligible in the Paris region. During the day, very few LLJ events are recorded at the urban site. Therefore, this study focuses on times between 18 and 9 UTC (20 h and 11 h local time).
- The maximum height explored in every 30-min wind profile is $1000\,\mathrm{m\ agl}$.
- In the study area, 99% of nocturnal periods present only one LLJ event within the ABL. Therefore, this study considers the presence of only one single LLJ event per night, unlike Tuononen et al. (2017) who accounted for the possible development of up to three simultaneous LLJ events within the ABL column in the same night at their coastal site in Helsinki.

In addition, some technical aspects of the algorithm were adapted. In the following, a brief description of the implemented adaptations in this study is given, further details can be found in Tuononen et al. (2017):

- **LLJ detection from a single wind profile**: we consider every horizontal wind speed profile between the first available gate ($238\,\mathrm{m\ agl}$ at QUALAIR-SU and $105\,\mathrm{m\ agl}$ at SIRTA) and $1000\,\mathrm{m\ agl}$. A LLJ is identified in a profile if the local

maximum of the horizontal wind speed is at least $1.5\,\mathrm{m\,s^{-1}}$ stronger than the first local minimum above or below. Note that the minimum below the core height may not be captured correctly by the observations because no information is available $< 238\,\mathrm{m\ agl}$ in the instrument's blind zone. A relative detection criterion was tested, but it produced a high number of false negatives (43%).

- **LLJ event detection**: a LLJ event is considered as a coherent detection if lasts at least $2\,\mathrm{h}$ (i.e. four 30-min averaged profiles). However, an event is valid if at least three profiles are detected over the course of this period with the following criteria for consecutive detections:
  - difference in core height $< 150\,\mathrm{m}$,
  - difference in core wind speed $< 20\%$,
  - difference in core wind direction $< 45°$,
  - difference in core time $< 1.5\,\mathrm{h}$.

The output parameters of the algorithm are listed as follows. i) LLJ occurrence: is a Boolean value (True [1] or False [0]) given to each profile; ii) LLJ core height: height of the maximum in the wind speed profile, in this case, the algorithm can provide it both in m agl and asl; iii) LLJ core speed: value of the wind speed at the core height; iv) LLJ core direction: wind direction at the height of the wind sped maximum. Additionally, the algorithm identifies the corresponding parameters for both the minimum above and below the jet core, in case they are recorded by the profile observations.

For the data collected during the summer of 2023 changes on the algorithm were implemented due to the implementation of the shallow DBS (see Section 2.2.4), the vertical profile of horizontal wind extends further down to the surface (first gate at $114\,\mathrm{m\ agl}$) in the dataset obtained for summer 2023 compared to the products available in 2022 (first gate $238\,\mathrm{m\ agl}$). This results in the observation of the wind speed minima both below and above the jet core. Therefore, for data collected for the summer of 2023, a slight update has been implemented so that now both minima are considered simultaneously (maximum compared to minima above and below). Now the two major steps of the LLJ detection can be summarized as follows:

- **LLJ detection from a single wind profile**: a wind profile is flagged as LLJ if the local maximum of the horizontal wind speed is at least $1.5\,\mathrm{m\,s^{-1}}$ stronger than the minima above **and** below if both minima exist. Otherwise, only the minimum above is considered.
- **LLJ event detection**: a set of wind profiles flagged as LLJ is considered as a coherent LLJ event if it displays a certain physical consistency over time regarding the core height, wind speed, and wind direction.

2.3.2 The vertical velocity variance

The vertical velocity variance (σ_w^2) is a powerful indicator that effectively describes the link between the jet winds and the surface-atmosphere exchanges. This turbulence quantity approximates the vertical mixing of the atmosphere (Banta et al., 2006). Hence, here it is assumed that the σ_w^2 observations at the first range gate ($238\,\mathrm{m\ agl}$) of the DWL WCS 400s at the urban site are representative to quantify the vertical mixing during the night (between sunset and sunrise) in the urban boundary layer. Section 3.3.2 describes the procedure used to classify LLJ cases according to their associated vertical mixing during.

2.4 The meteorological stations

One of the objectives of this thesis is to determine the impact of the LLJ on the UHI intensity in the Paris region. To estimate the UHI intensity (ΔUHI = $T_{urban} - T_{rural}$) (Section 1.3), the QUALAIR-SU site (red dot in Fig. 2.1) is the urban reference, and a Météo France station located at Melun ($48.613°$N; $2.679°$E; $91\,\mathrm{m\ asl}$) is the rural reference (brown dot in Fig. 2.1).

The air temperature measurements at QUALAIR-SU are collected by using a Vaisala WXT520 automatic weather station located at $22\,\mathrm{m\ agl}$ on the roof of a medium height building, while at Melun the data are collected by a Sterela Opale UME station located at $2\,\mathrm{m\ agl}$. The data from both sites are averaged in 30-min intervals to match the DWL analysis. To determine the impact of the LLJ on the ΔUHI, this study only considers the nocturnal period between sunset and sunrise. Further details of this experiment and its results are presented in Chapter 3.

2.5 Synthesis

A Vaisala DWL WCS 400s was deployed on a tall and isolated tower in the city center of Paris, in a neighbourhood with an average building height of $25\,\mathrm{m}$. For over two years, this instrument has collected wind observations using a scanning strategy designed to analyze the four-dimensional dynamics of the urban boundary layer. This thesis focuses on characterizing the summertime nocturnal LLJ and its interaction with the urban surface of the Paris region, emphasizing the use of vertical profiles of horizontal wind and vertical velocity to estimate vertical mixing. To assess the spatial variability of the LLJ, horizontal wind profile data collected by a DWL WLS70 operated by the SIRTA observatory, located $25\,\mathrm{km}$ southwest of the city center in the Plateau Paris-Saclay, are also utilized. In addition to the designed scan strategies and the implementation of the novel shallow DBS scan for an improved monitoring of near-surface horizontal winds,, this thesis developed and implemented computational methods for wind profile processing.

Furthermore, data from surface weather stations are used to evaluate the LLJ's impact on the spatial differences in air temperature between the city centre and the rural background (i.e. the urban heat island intensity).

Chapter 3

The summertime Paris region Low-Level Jet and its impacts on the UHI

Contents

This chapter presents the scientific article entitled "*The Paris Low-Level Jet During PANAME 2022 and its Impact on the Summertime Urban Heat Island*" (Céspedes et al., 2024) which is a product of this thesis and has been accepted for publication in the journal *Atmospheric Chemistry and Physics*.

In parts, this chapter contains information that has already been presented in the Introduction (Chapter 1) and the methodology (Chapter 2), specifically the

introduction of the instruments and measurement sites (Section 3.2 overlaps with Section 2.2.1), the method implemented for the detection of LLJ events (Section 3.2.3 overlaps with Section 2.3.1), and the assessment of the vertical velocity variance (Section Section 3.3.2 overlaps with Section 2.3.2). New scientific results are presented in Section 3.3.

Abstract

Both the Low-Level Jet (LLJ) and the Urban Heat Island (UHI) are common nocturnal phenomena. While the canopy layer UHI has been studied extensively, interactions of the LLJ and the urban atmosphere in general (and the UHI in particular) have received less attention. In the framework of the PANAME initiative in the Paris region, continuous profiles of wind speed and vertical velocity were recorded with two Doppler Wind Lidars (DWL) - for the first time allowing for a detailed investigation of the summertime LLJ characteristics in the region. Jets are detected for 70% of the examined nights, often simultaneously at an urban and a suburban site highlighting the LLJ regional spatial extent. Emerging at around sunset, the mean LLJ duration is $\sim 10\,\mathrm{h}$, the mean wind speed is $\sim 9\,\mathrm{m\,s^{-1}}$, and the average core height is $400\,\mathrm{m}$ above the city. Many events show signatures in the temporal evolution that indicate that the inertial oscillation mechanism plays a role in the jet development: a clockwise veering of the wind direction and a rapid acceleration followed by a slower deceleration. The horizontal wind shear below the LLJ core induces variance in the vertical velocity (σ_w^2) above the urban canopy layer. It is shown that σ_w^2 is a powerful predictor for regional contrast in air temperature, as the UHI intensity decreases exponentially with increasing σ_w^2 and strong UHI values only occur when σ_w^2 is very weak. This study demonstrates how DWL observations in cities provide valuable insights into near-surface processes relevant to human and environmental health.

3.1 Introduction

The nocturnal Urban Heat Island (UHI) in the canopy layer is surely among the most studied phenomena in the urban environment. As this UHI is defined as the difference in air temperature between built-up and rural settings right above ground level (Oke et al., 2017a), investigations usually focus on the near-surface atmosphere conditions, while the dynamics of the Atmospheric Boundary Layer (ABL) are rarely considered explicitly. Although wind speed and atmospheric stratification play a significant role in the formation of the UHI, the intensity of the UHI is strongest under low wind speed and cloud-free conditions (Oke et al., 2017a), i.e., when atmospheric stratification in rural settings tends to be relatively stable. During stable atmospheric stratification, the atmospheric boundary layer flow may become decoupled from the friction exerted by the surface, which can lead to the formation

of the nocturnal Low-Level Jet (LLJ). The LLJ is manifested by a sharp maximum in the vertical profile of the horizontal wind speed, typically at a height between $100\,\mathrm{m}$ and $1000\,\mathrm{m}$ above the ground, referred to as the core of the jet (Stull, 1988b). Another feature related to the LLJ wind profile is a strong decrease that goes along with a minimum in the horizontal wind speed above the core height (Shapiro et al., 2016). The LLJ is a mesoscale phenomenon frequently observed in the ABL, mostly during nights with fair-weather conditions after clear-sky days. It is usually characterized based on its core height, wind speed and wind direction. With clear links to various processes such as advection, wind shear and turbulent mixing, the LLJ core characteristics can have a series of practical implications with respect to, e.g., air quality (Wei et al., 2023; Klein et al., 2019), changes in precipitation patterns (Algarra et al., 2019; Chen et al., 2022), aviation safety (Gultepe et al., 2019; Liu et al., 2014), the potential of, and risk to, wind energy production (Lundquist, 2021; Luiz and Fiedler, 2022; Rubio et al., 2022), urban ventilation (He et al., 2022), as well as the heat spatial distribution and intensity of the UHI effect (Kallistratova and Kouznetsov, 2012; Hu et al., 2013; Ulpiani, 2021; Lin et al., 2022). The LLJ is highly relevant for meteorology because its core characteristics are associated with the turbulent mass exchange in the ABL (Blackadar, 1957). Since the 1950s, the LLJ has been extensively documented, worldwide and throughout the year (Blackadar, 1957; Qi et al., 1999; Banta et al., 2002; Tuononen et al., 2017; Hartman, 2018; Du and Chen, 2019; Jiménez-Sánchez et al., 2019; Li and Du, 2021). One converging point of the previous studies is that the LLJ core generally is formed during the evening, followed by an increase in the core wind speed, and it eventually dissipates at about sunrise. Blackadar (1957) proposed the inertial oscillation theory to explain the physical mechanism behind the LLJ formation, but other mechanisms can also play a role. In The Great Plains, the LLJ formation is linked to the IO and the differential heating and cooling of the sloping terrain (Holton, 1967; Shapiro et al., 2016). Jets are also observed over coastal regions as the result of the land–sea breeze interactions and temperature gradients (Karipot et al., 2009; Roy et al., 2021). However, regardless of the study area or mechanism of formation, most of the observational-descriptive studies agreed on the importance of classifying the LLJ, usually by one of its main characteristics (Banta et al., 2002; Baas et al., 2009; Karipot et al., 2009; Bonin et al., 2015). Grouping of LLJ events into categories facilitates description and the analysis of potential effects on the environment of the affected area. The most widely used classification criterion is the core wind speed. Banta et al. (2002) were one of the first to propose four categories of wind speed to describe LLJs: (0-5), (5-10), (10-15) and (15-20) $\mathrm{m\,s^{-1}}$. Subsequently, several studies around the world have adopted similar categories of wind speed to study the LLJ (Karipot et al., 2009; Kallistratova et al., 2013; Wei et al., 2013; Arfeuille et al., 2015; Vanderwende et al., 2015; Carroll et al., 2019). This classification system provides a better understanding of the LLJ phenomenon development, evolution, and impacts based on the wind speed intensity. Studies focused on the effects of the

LLJ dynamics on the near-surface atmosphere, tend to consider other parameters like Turbulent Kinetic Energy (TKE), in addition to the core wind speed. Banta et al. (2002) and Banta et al. (2003) successfully showed that the mechanical turbulence generated by the wind shear below the jet core plays a key role in controlling fluxes between the surface and the atmosphere. In particular, the downward transport of turbulence can modulate near-urban surface atmospheric processes like the UHI effect (Hu et al., 2013; Lin et al., 2022).

The UHI can be observed worldwide throughout the year, but in high-density cities in the mid-latitudes, it tends to be stronger during the summer (Lemonsu and Masson, 2002; Oke et al., 2017a). The expansion of urban areas under poor ventilation and cooling design has made the UHI a prominent factor in the deterioration of the human thermal comfort (Kong et al., 2016; Li et al., 2019; Lin et al., 2022). High nocturnal temperatures increase the stress on the human body at times when it needs to rest (sleep), leading to higher mortality (Robine et al., 2008; Taylor et al., 2015; Ridder et al., 2016; He et al., 2022). While the UHI phenomenon is driven by excess heat in the built environment, atmospheric dynamics (advection, mixing, subsidence) significantly modulate the UHI intensity (Oke, 1973; Oke et al., 2017a). Weak flow conditions favor the formation of strong UHI (Lemonsu and Masson, 2002), while each increase of $1\,\mathrm{m\,s^{-1}}$ in wind speed was found to reduce the urban air temperature during summer nights by up to $2\,^{\circ}\mathrm{C}$ (Cheng et al., 2012; He et al., 2022).

Although surface wind speed has long been recognized as an important indicator for variations in the UHI intensity, only a few studies in urban areas have investigated the relation between advection produced by the nocturnal LLJ and the UHI. Studies conducted in Sao Paulo, Brazil (Sánchez et al., 2022a); Oklahoma, USA (Hu et al., 2013); Moscow, Russia (Kallistratova and Kouznetsov, 2012; Kallistratova et al., 2013); and Beijing, China (Lin et al., 2022); concluded that there is a negative correlation between the UHI intensity and the core wind speed of the jet. Even though these efforts have contributed to understanding the potential implications of the LLJ on UHI development, these works are mostly based on a limited number of radiosonde observations and few case studies. Hence, continuous observations of the wind speed profile with high temporal and spatial resolution are still needed in urban environments. Another relevant aspect of the interaction between the LLJ and the Urban Boundary Layer (UBL) is that the urban environment enhances atmospheric mixing and buoyancy that can again also affect the characteristics of those LLJs originated in the rural surroundings. In London, UK, Barlow (2014) and Tsiringakis et al. (2022), have investigated the interaction between the LLJ and the UBL based on a combination of continuous DWL observations and modeling data, highlighting the importance of both the LLJ (downward mixing by shear-driven turbulence) and the urban surface (upward mixing driven by urban heat and roughness).

In France, the LLJ has been observed in northern coastal urban areas (Roy et al., 2021, 2022; Dieudonné et al., 2023), but coastal jets usually present different formation mechanisms and characteristics than those observed inland. This is mainly explained due to the importance of the sea-land breeze interactions (Karipot et al., 2009). Particularly in the urban area of Paris, some studies have been conducted to understand the impact of the LLJ on air quality, the mixing of pollutants within the UBL, and the UHI development. Klein et al. (2019) performed a one-day case study using a combination of DWL profiles, numerical simulations and ancillary observations, concluding that nocturnal LLJs can modulate the evolution of the mixing layer with implications for the ozone concentration in the early morning. Cheliotis et al. (2021) collected DWL data during a period of 3 months in fall 2014, observing LLJs in 20 out of 63 nights. They linked the production of turbulent coherent structures to the presence of LLJ events, that in turn play an important role in the transport of heat, moisture and pollutants through the ABL. Wouters et al. (2013) presented a model-based case study during the Summer of 2006, where simulations of UHI and LLJ allowed them to conclude that the UHI could be affected by the nocturnal stability and mixing associated to the LLJ. However, when comparing with radiosonde profiles the strong jets were underestimated by the model, making it hard to identify what characteristics of the jets influenced the UHI development. Therefore, as far as the authors of the present work are aware, variations of the LLJ characteristics over periods exceeding a few days and their possible implications for UHI development have not yet been investigated in the Paris region. One key reason is the previous lack of medium or continuous long-term observations of the wind speed profile within the Paris UBL.

Strengthening the knowledge in this field is important because there is observational evidence that the LLJ is a common phenomenon in Europe, frequently detected at distances of less than $400\,\mathrm{km}$ from the city of Paris (Baas et al., 2009). Furthermore, gaining understanding about the LLJ impacts on the UHI is imperative, given the significance of UHI as a main concern in a city like Paris where a large number of inhabitants (approx. 12 million) is potentially exposed to severe heat hazards that are expected to become increasingly severe in future climates. As a consequence, the present study is going to investigate the characteristics and nocturnal temporal evolution of the LLJ observed over the Paris region in summer 2022, and what are their implications for the UHI intensity. For the first time, providing a comprehensive description of the occurrence of summertime LLJ in the Paris region and an analysis of its variability. Here, we assess the impact of the LLJ on the profile of the horizontal wind speed and the UHI intensity. This paper is structured as follows: Section 3.2 provides details of the study area, study period, DWL and surface-based meteorological observations, and automatic detection of LLJ and UHI determination; Section 3.3 presents the results of the LLJ detection and performance, LLJ classification, LLJ characteristics and wind profile, LLJ nocturnal evolution, and the UHI evolution; finally, Section 3.4 present the summary and

conclusions of this paper.

3.2 Methods and materials

3.2.1 Study area and study period

Here we study the LLJ characteristics in the Paris region, France. With a population of over 12 million people, the Paris agglomeration is the second biggest megalopolis and the most densely populated city in Europe. The Paris region has experienced fast and wide urbanization during the last decades, but is still surrounded by natural and agricultural areas. Anthropogenic heat emissions and changes in land cover are aggravating the UHI effect (Lemonsu and Masson, 2002). Fig. 3.1 shows the topography of the Paris region, the land cover classification, and the geographical location of the experimental sites. Paris is located about $150\,\mathrm{km}$ from the sea, in a valley defined by the Seine River basin and surrounded by plateaus with modest topographic variation, which rise no more than $230\,\mathrm{m}$ above sea level (asl). In the city of Paris, the terrain is relatively flat, the lowest altitude is about $20\,\mathrm{m\ asl}$ along the river, and the highest is about $130\,\mathrm{m\ asl}$ on hills in the northern parts of the city. About $20\,\mathrm{km}$ southwest of the city, the Paris-Saclay Plateau is located, which has a mean extension of 10 km and is elevated about $160\,\mathrm{m\ asl}$. It is an important economic, academic, and industrial area in the region. Due to the distance from the sea, there is no interaction of the sea breeze with the urban area. The long-term prevailing wind direction in the area is southwesterly and has a maritime origin, but winds from the northeast are also often observed (Haeffelin et al., 2005; Pal et al., 2012).

This study focuses on the summer of 2022, between 15 June and 31 August. The year 2022 was recorded as the warmest observed in France so far, with three reported heat waves between June and August, leading to an exceptional nocturnal mesoscale flow over the Paris region during summertime with a predominant northeasterly flow. Severe conditions were observed especially in the July heat wave, where sea-level temperature anomalies above $12\,^{\circ}\mathrm{C}$ were associated with a deficit in precipitation rate of about 80%, leading to extreme droughts (Petit et al., 2023). In general, the summer of 2022 had prevailing winds coming from the northerly to northeasterly directions (0°-75°), with speeds below $7\,\mathrm{m\,s^{-1}}$. The air temperature ranged between $11.8\,^{\circ}\mathrm{C}$ and $35.2\,^{\circ}\mathrm{C}$, with a mean value of $20.6\,^{\circ}\mathrm{C}$. These temperature values for 2022 are high when compared to longer-term averages. Using a comprehensive data set spanning from 2006 to 2022, collected by the Météo France surface meteorological network and processed by the ReOBS project (Chiriaco et al., 2018), the common of synoptic conditions within the study area are analyzed for the summer months of June, July, and August. The prevailing nocturnal winds exhibit a range of directions mostly between 170° and 45°, with

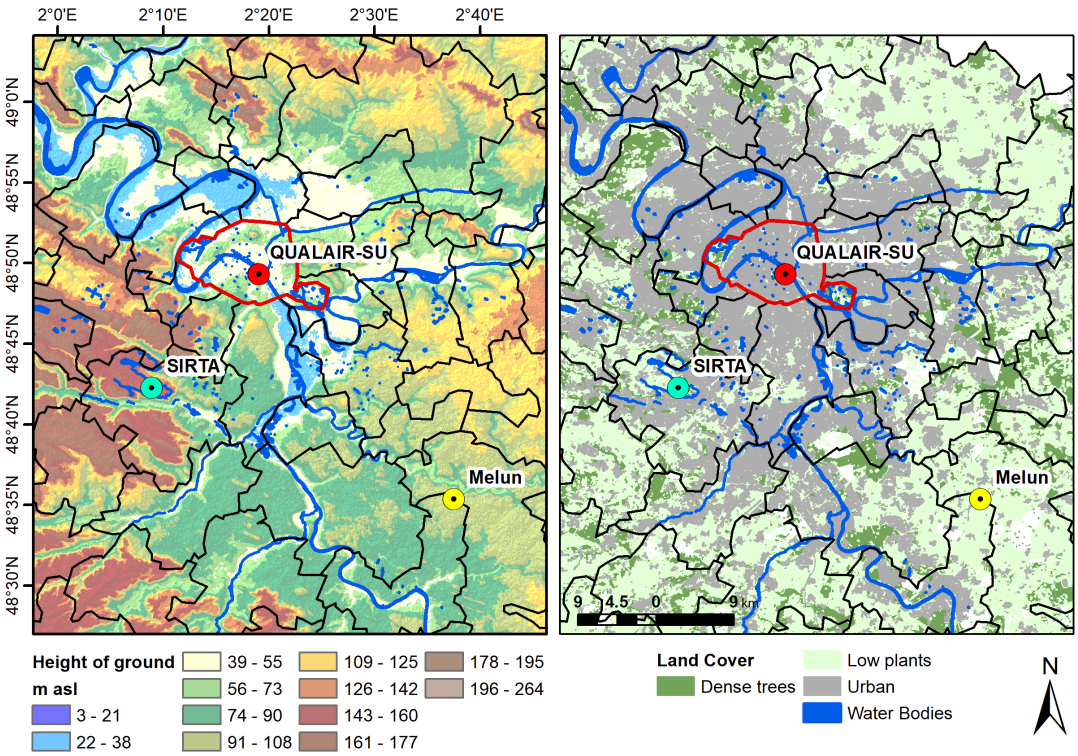

Figure 3.1 : Paris region (France) study area and the location of the experimental sites. a) Topographic map from ESA (2023), and b) land cover map from Region (2023). The red borders indicate the administrative boundary of the City of Paris. The black polygons are administrative borders within the Paris region. The red dot represents the location of the WindCube Scan 400S at QUALAIR-SU (urban lidar), the cyan dot is the location of the WindCube WLS70 at SIRTA (suburban site), and the yellow dot is the location of Météo France meteorological measurement site at Melun (rural site).

average speeds below $8\,\mathrm{m\,s^{-1}}$. The nocturnal air temperature ranges between $6.6\,^{\circ}\mathrm{C}$ to $38\,^{\circ}\mathrm{C}$, with a mean temperature of $18.6\,^{\circ}\mathrm{C}$.

3.2.2 Doppler Wind Lidar measurements

The Doppler Wind Lidar (DWL) measurements recorded during the study period (15 June and 31 August, 2022), both at the urban and the suburban sites contribute to the wind profile measurement network of the initiative PANAME (PAris region urbaN Atmospheric observations and models for Multidisciplinary rEsearch). The PANAME initiave is an unprecedented converge of multidisciplinary scietific investigations that promotes the synergy of numerous research projects that investigate the Paris urban environment in relation to weather, climate, air quality, and impacts on human health. The present study is part of the project so-called "DYNAMICS", which contributes to PANAME with an improved characterisation of nocturnal mean flow and turbulence conditions.

The high-power scanning DWL Vaisala WindCube Scan 400S was deployed in

the city center of Paris (red dot in Fig. 3.1), on the roof of the Zamansky tower ($88\,\mathrm{m}$ above ground level (agl)) at the QUALAIR-SU supersite ($48.8°$N; $2.36°$E; $125\,\mathrm{m\ asl}$). QUALAIR-SU is a platform dedicated to atmospheric observations and air quality monitoring, which is operated by the Laboratoire Atmosphères, Observations Spatiales (LATMOS) and is hosted by Sorbonne Université, at the Jussieu campus (Qualair, 2022). The WindCube Scan 400S is a DWL equipped with a scanning head capable of orienting the laser beam in any direction of the hemisphere (Thobois et al., 2019; Dolfi-Bouteyre et al., 2008). The high energy emitted by the pulse, at $1.54\,\mu\mathrm{m}$ wavelength, allows it to sample the atmosphere at a distance of up to $7\,\mathrm{km}$. Several configurations of pulses are available corresponding to different spatial resolutions (75, 100, 150, or $200\,\mathrm{m}$) with a resolution of $75\,\mathrm{m}$ used in this study. A blind zone, spanning twice the spatial resolution ($150\,\mathrm{m}$ in this study), restricts measurements close to the sensor. Table 3.1 provides a summary of the main properties of the instrument. The WindCube Scan 400S can measure under different scanning strategies such as vertical stare, Plan-Position Indicator (PPI) and Doppler Beam Swinging (DBS). Liu et al. (2019) provide a detailed technical description of every scan mode operation and their potential applications. The DBS mode is widely used in urban meteorology to measure vertical profiles of horizontal wind speed and wind direction. It was shown by Pearson et al. (2009) that DBS operates fast and it well-capture unstable flows in the urban interface. In this study, a *five-point* DBS mode is used, with the scanning head successively addressing five lines of sight (LOS): one vertically oriented LOS ($90°$ elevation angle) and four tilted LOS ($75°$ elevation angle) pointing north, east, south, and west, respectively. Each scanning sequence (1 DBS cycle) is completed in approximately $15\,\mathrm{s}$, with $1\,\mathrm{s}$ of accumulation time for each LOS and $2\,\mathrm{s}$ between two LOS. The WindCube Scan 400S has been aligned with the geographic north, using the hard target method which has a precision of $\pm 2°$.

During the study period (15 June - 31 August 2022) the scan strategy was designed to follow an hourly schedule, integrating the DBS scan with the vertical stare and PPI. In the first half of every hour the DBS is performed for $9\,\mathrm{min}$, followed by a 3-minute full PPI at $0°$ of elevation with an angular resolution of $2°/\mathrm{s}$, then $5\,\mathrm{min}$ of continuous vertical stare at $90°$ of elevation, followed by other $9\,\mathrm{min}$ of DBS and closing with other 3-minute full PPI at $0°$. The second half of hour repeats the same schedule. In this study, all vertical profiles of horizontal wind speed observations were derived from the DBS, while the vertical stare data are used to derive the Vertical Velocity Variance (σ_w^2). Observations from the PPI are not used in this study. The implemented scanning schedule was designed to fulfill several objectives but was not specifically optimized for the detection of LLJ. One quality control step is implemented to ensure a high-quality wind profile product, data with CNR (Carrier-Noise-Ratio) below $-20\,\mathrm{dB}$ and above $5\,\mathrm{dB}$ are excluded whereby omitting weak signals and clouds, respectively.

Table 3.1: Properties of the Vaisala Doppler Wind Lidars WindCube Scan 400S (Urban site) and WLS70 (Suburban site). For the WindCube Scan 400s, the symbol **(*)** marks the setting used in this study.

Properties	WindCube Scan 400S	WindCube WLS70
Altitude Location (m asl)	125	155
Pulse repetition frequency (kHz)	7, 10*, 20, or 40	10
Pulse width (ns)	100*, 200, 400, or 800	100
Range gate resolution (m)	75*, 100, 150 or 200	50
Min range (m)	150	100
Max range (m)	7000	2000
Accumulation time (s)	1 per beam	1 per sequence
Radial wind speed range ($m\,s^{-1}$)	±30	±30
Emission wavelength (µm)	1.54	1.54
Radial wind accuracy ($m\,s^{-1}$)	0.1	0.3
Height location (m agl)	88	5
First available gate (m agl)	238	105

In addition to the observations in central Paris, data collected by a Vaisala WindCube WLS70 at a suburban location on the Plateau Saclay are used in this study. The data recorded with this instrument are used in this study only to highlight the regional scale of the LLJ observed. A detailed analysis of this data collection will be the subject of future studies. This profiling DWL is an instrument specially developed for meteorological applications (Cariou et al., 2009). The observations are conducted at the SIRTA observatory (Site Instrumental de Recherche par Télédetection Atmosphérique (Haeffelin et al., 2005)), located on the campus of Ecole Polytechnique in Palaiseau, 20 km southwest of Paris (48.713°N; 2.208°E; 156 m asl; Fig. 3.1). Over the last 25 years, SIRTA has collected a comprehensive data set of atmospheric observations using in-situ measurements as well as passive and active remote sensing instruments, characterizing the regional atmospheric background of the Paris region (Dupont et al., 2016). The WindCube WLS70 uses a 1.54 µm pulsed fiber laser and a coherent detection system which provides sufficient backscattering signal up to 4 km. Every LOS performed by the WLS70 has a fixed spatial resolution of 50 m (see Table 3.1). The WLS70 performs four-point DBS measurements (10 s), in a similar way to the WindCube Scan 400S, but without the vertical LOS. This study uses 10-min averaged profiles, a previous quality control step is applied to these profiles to ensure a 80% of data availability at each range gate.

3.2.3 Automatic LLJ detection

Various methods and criteria have been developed to detect a LLJ in a vertical profile of horizontal wind, with techniques depending on the characteristics of

the data source (e.g. limitations from measurement sensors) and even the study area. Stull (1988b) defined a LLJ as any lower-tropospheric wind maximum in the vertical profile of horizontal wind speed, that is at least $2\,\mathrm{m\,s^{-1}}$ greater than speeds both above and below, within the lowest $1500\,\mathrm{m}$ of the atmosphere. This absolute criterion is widely found in the literature. It was applied to SODAR data collections (Karipot et al., 2009; Duarte et al., 2015) and radiosonde profiles measured in the USA (Bonner, 1968; Whiteman et al., 1997), and even in the Arctic Sea (Andreas et al., 2000). The threshold of this absolute criterion can be tuned as done by Banta et al. (2002), who used a value of $0.5\,\mathrm{m\,s^{-1}}$. However, under very weak flow conditions ($< 2\,\mathrm{m\,s^{-1}}$) the performance of the criterion could present limitations in the identification of LLJ events (Baas et al., 2009). In such cases, it is possible to use a relative threshold instead, in which a LLJ is detected by a velocity difference of 20%-25% between the local maxima and minima. In fact, absolute and relative thresholds have been combined to further improve detection. In different long-term radiosonde campaigns in Sao Paulo, Brazil, the criterion to identify a LLJ event in a single wind speed profile was that the maximum at the LLJ must be both greater than or equal to $2\,\mathrm{m\,s^{-1}}$ and 25% faster than the minimum above (Sánchez et al., 2022a, 2020). Although in other DWL or SODAR-based studies, the same thresholds have been used, the high temporal and spatial resolution of surface-based remote sensing observations allows the incorporation of complementary steps. This enables not only an optimized detection of individual LLJ profiles but also the identification of LLJ events evolving over the time (Baas et al., 2009; Tuononen et al., 2015; Tuononen et al., 2017). In this study, the automatic LLJ detection is an adaptation from the method described by Tuononen et al. (2017) and uses 30-min averaged profiles of horizontal wind speed, to best combine the 15-min data products available at QUALAIR-SU and the 10-min data products available at SIRTA. This temporal resolution was previously used in SODAR studies presenting coherent LLJ detection (Karipot et al., 2009; Baas et al., 2009; Duarte et al., 2015).

Therefore, based on the literature and exploratory tests on the data set, some important conceptual aspects were adapted compared to the original method from Tuononen et al. (2017):

- Daytime LLJ events are negligible in the Paris region. During the day, very few LLJ events are recorded at the urban site. Therefore, this study focuses on the nocturnal periods, times between 18 h and 9 h UTC (20 h and 11 h local time).
- The maximum height explored in every 30-min wind profile is $1000\,\mathrm{m\ agl}$.
- In the study area, 99% of nocturnal periods present only one LLJ event within the ABL. Therefore, this study considers the presence of only one single LLJ event per night, unlike Tuononen et al. (2017) who accounted for the possible

development of up to three simultaneous LLJ events within the ABL column in the same night.

Additionally, technical aspects of the algorithm were also adapted. In the following, a brief description of the implemented adaptations in this study is given, further details can be found in Tuononen et al. (2017):

- **LLJ detection from a single wind profile**: we consider every horizontal wind speed profile between the first available gate ($238\,\mathrm{m\ agl}$ at QUALAIR-SU and $105\,\mathrm{m\ agl}$ at SIRTA) and $1000\,\mathrm{m\ agl}$. A LLJ is identified in a profile if the local maximum of the horizontal wind speed is at least $1.5\,\mathrm{m\,s^{-1}}$ stronger than the first local minimum above or below. Note that the minimum below the core height may not be captured correctly by the observations because no information is available $< 238\,\mathrm{m\ agl}$ in the instrument's blind zone. A relative detection criterion was tested, but it produced a high number of false negatives (43%).
- **LLJ event detection**: a LLJ event is considered as a coherent detection if lasts at least $2\,\mathrm{h}$ (i.e. four 30-min averaged profiles). However, an event is valid if at least three profiles are detected over the course of this period with the following criteria for consecutive detections:
  - difference in core height $< 150\,\mathrm{m}$,
  - difference in core wind speed $< 20\%$,
  - difference in core wind direction $< 45°$,
  - difference in core time $< 1.5\,\mathrm{h}$.

The output parameters of the algorithm are listed as follows. i) LLJ occurrence: is a Boolean value (True [1] or False [0]) given to each profile; ii) LLJ core height: height of the maximum in the wind speed profile, in this case, the algorithm can provide it both in m agl and asl; iii) LLJ core speed: value of the wind speed at the core height; iv) LLJ core direction: wind direction at the height of the wind sped maximum. Additionally, the algorithm identifies the corresponding parameters for both the minimum above and below the jet core, in case they are recorded by the profile observations.

3.2.4 Surface data and UHI determination

The UHI intensity (ΔUHI = $T_{urban} - T_{rural}$) is defined as the difference in air temperature between an urban (T_{urban}) and a rural (T_{rural}) site. Usually, standard meteorological observations at $2\,\mathrm{m\ agl}$ height are compared. In the current work, the QUALAIR-SU site (red dot in Fig. 3.1) is chosen as the urban site, and a Météo France station at Melun ($48.613°$N; $2.679°$E; $91\,\mathrm{m\ asl}$) is chosen as the rural site (yellow dot in Fig. 3.1).

Data collected at the QUALAIR-SU supersite were used to represent the central urban air temperature (T_{urban}) given that continuous and long-term observations are available. During the Intensive Observation Period (IOP) in the framework of PANAME-2022 campaign, surface-based meteorological stations were installed to capture the air temperature within the built environment at street level, e.g. at Place de la Madeleine (48.870 84°N; 2.324 32°N; 79 m asl) and Boulevard des Capucines (48.870 66°N; 2.331 75°N; 81 m asl) on 10 July 2022, i.e. later than the start of the analysis period of the current study (15 June 2022). Hence, data from the QUALAIR-SU meteorological station located at roof level (20 m agl) are here considered to well represent the intensity of the ΔUHI for the Paris region. ΔUHI is stronger when using the street-level urban measurement sites by about 1 °C when ΔUHI $>$ 6 °C (see Fig. B.1). Additionally, wind data collected from a 25 m meteorological tower installed at Montsouris Park are used in this study to assess the relationship between ΔUHI and the near-surface wind speed.

The temperature at Melun is measured using a Sterela Opale UME at 2 m agl, and that at QUALAIR-SU using a Vaisala WXT520 automatic weather station at 22 m agl. The mean building height around the QUALAIR-SU site is about 25 m. 30-min averages are calculated for both sites to match the DWL analysis intervals. The average nocturnal UHI intensity is calculated as the mean of temperature differences recorded during the nocturnal period (sunset to sunrise). Additionally, based on cloud base height observations from a Lufft CHM15k automatic lidar ceilometer operated at the QUALIR-SU site, nights were classified into cloudy, partly cloudy, and cloud-free periods using the classification approach presented by Kotthaus and Grimmond (2018).

3.3 Results

3.3.1 LLJ detection performance

For the performance evaluation of the algorithm the time difference between two consecutive time steps for which a LLJ is detected gives an indication of the persistence of the jet event. The threshold sensitivity and performance analysis by Tuononen et al. (2017) revealed that the time-delta difference threshold has a strong influence on the performance of the algorithm. This may bias the algorithm towards the detection of false positives or very short events, which are not object of study in this work. The detection of false positives is further dependent on the quality of the measurements, which in turn depends on factors such as power and sensitivity of the laser system, vertical distribution of the aerosol load (tracers, see Section 3.2.2), and the presence of clouds.

An example of a coherent LLJ detection is presented in Fig. 3.2a. The jet core becomes visible in the late evening of the 9 August at 19h UTC at 550 m agl,

and with a wind speed of approximately $8\,\mathrm{m\,s^{-1}}$. After sunset, the core height stabilizes at $500\,\mathrm{m\ agl}$ and reaches a maximum wind speed between 21h and 23 UTC. After midnight, the core height increases beyond $550\,\mathrm{m\ agl}$, followed by a gradual decrease in the core wind speed. The jet persists throughout the night and into the early morning before it dissipates at 8h UTC on the 10 August. Fig. 3.2b presents a LLJ detection under weaker flow conditions and lower boundary layer height than the previous example. This LLJ event clearly failed the criterion of four consecutive detection explained in Section 3.2.2, and it is not considered in this study.

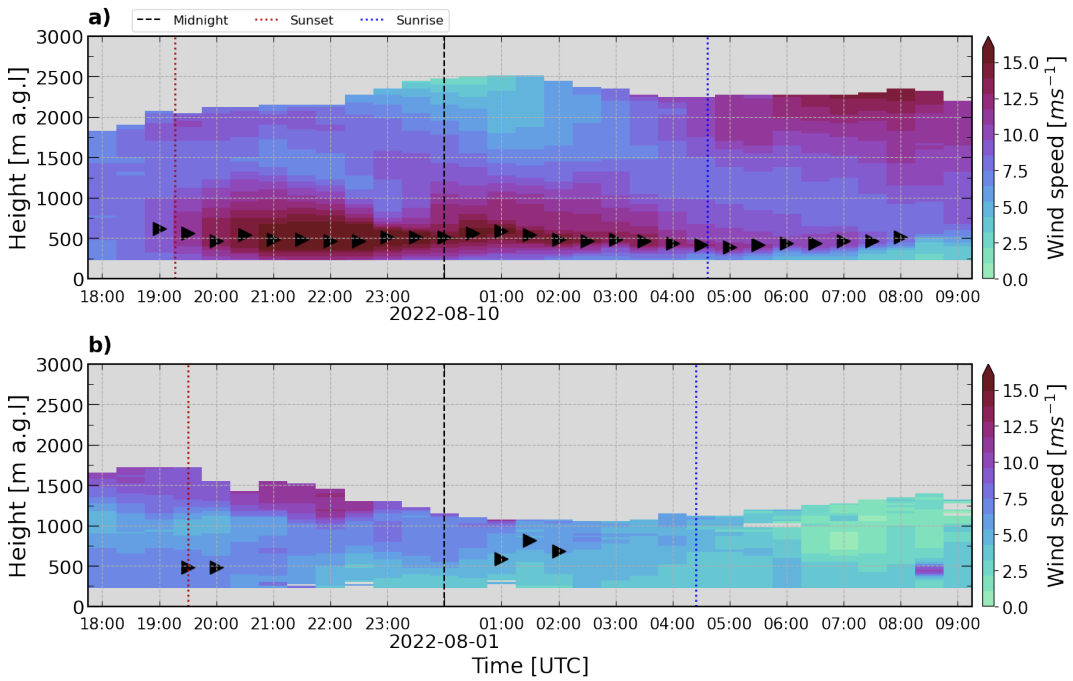

Figure 3.2 : Time-height evolution of the horizontal wind speed. The temporal series are composited by 30-min average profiles retrieved by measurements performed by the WindCube Scan 400S at QUALAIR-SU (Urban site) between 18 - 09 UTC on a), between 9 and 10 August 2022, and b) 31 July to 1 August 2022. In both cases, the black triangles represent the core of the Low-Level Jet detected by the automatic procedure.

3.3.2 LLJ classification

By classifying LLJ according to their core wind speed magnitude, Banta et al. (2002) found that strong jets tend to occur at greater altitudes. Banta et al. (2003) studied the relationship between LLJ characteristics and turbulence within the stable nocturnal boundary layer, concluding that the core wind speed and core height can be used to diagnose turbulence effects in the region beneath the jet, considering that strong core wind speed are usually associated with strong turbulence below (Bonin et al., 2015) and above the core (Conangla and Cuxart, 2006). In this study, both core wind speed and core height were tested as indicators for the classification of LLJ (not shown here), however, it was not possible to identify groups with consistent patterns in the LLJ characteristics. Hence, we found that the vertical velocity variance (σ_w^2)

is a more meaningful indicator as it effectively describes the link between the jet winds and surface-atmosphere exchanges. This turbulence quantity approximates the vertical component of the TKE during stable conditions (Banta et al., 2006). Here it is assumed that the σ_w^2 observations at the first range gate ($238\,\mathrm{m\ agl}$) of the DWL at the urban site is representative of the vertical mixing conditions in the nocturnal urban boundary layer. Each LLJ event is classified according to the mean nocturnal average σ_w^2 (between sunset and sunrise). Three classes are defined based on thresholds defined by the median and the 75th percentile of the distribution of σ_w^2 (Fig. 3.3): indicating low ($< 0.11\,\mathrm{m^2 s^{-2}}$), intermediate ($0.11\,\mathrm{m^2 s^{-2}} \leq \sigma_w^2 < 0.23\,\mathrm{m^2 s^{-2}}$), and high ($\geq 0.23\,\mathrm{m^2 s^{-2}}$) vertical velocity variance, respectively.

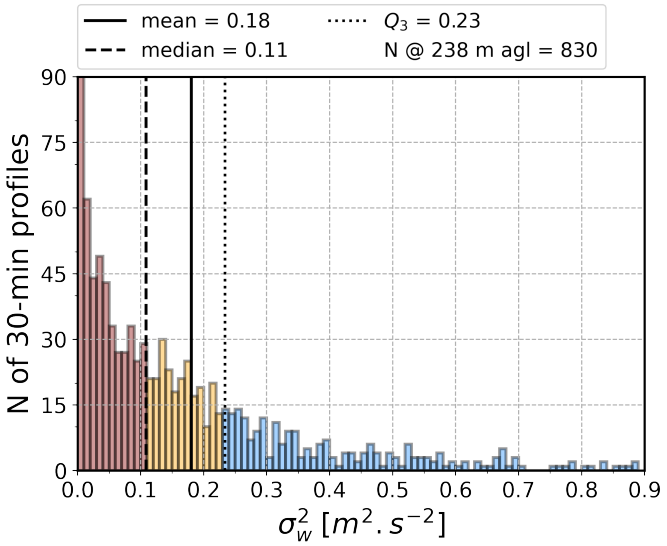

Figure 3.3 : Histogram of the variance of the vertical velocity variance (σ_w^2) retrieved from vertical stare measurements at the first range gate at the urban site ($238\,\mathrm{m\ agl}$). The colors correspond to the σ_w^2 classes and are : low vertical mixing $\sigma_w^2 < 0.11\,\mathrm{m^2 s^{-2}}$ (red), moderate vertical mixing $0.11\,\mathrm{m^2 s^{-2}} \leq \sigma_w^2 < 0.23\,\mathrm{m^2 s^{-2}}$ (orange), and strong vertical mixing $\sigma_w^2 \geq 0.23\,\mathrm{m^2 s^{-2}}$ (blue). N = total number of 30-min profiles and Q_3 = Quartile 3, upper quartile.

3.3.3 LLJ characteristics

Based on the 77-day period spanning from 15 June 2022 to 31 August 2022, 55 nights (70%) exhibit a LLJ event at the urban QUALAIR-SU site. 96% (53 out of 55 nights) of these LLJ events were also detected over the suburban site at SIRTA, showing that the nocturnal LLJ is a regional phenomenon in the Paris region. Nine out of 55 LLJ events were detected during cloudy conditions, but the complex interactions with cloud dynamics are beyond the scope of this work. Therefore, this study focuses on 46 nights (60% of the total of 77 nights in the study period) with a LLJ event detected at QUALAIR-SU under cloud-free conditions, in which 830 individual 30-min profiles (i.e. 415 h) were associated with a jet. According to these results, it is possible to say that the LLJ activity during summer Paris 2022 is high, specially when compared to previous studies conducted in Paris during the autumn period or

to other European studies of summertime LLJ activity. In the local context, Cheliotis et al. (2021) reported a 32% occurrence of LLJ during the fall of 2014 in Paris by using data collected by a DWL installed at QUALAIR-SU site. A climatological study at Cabauw, The Netherlands, found that LLJ occurred 32% of the time during summer, based on 7 years of SODAR profile data (Baas et al., 2009). At Utö, Finland, another climatological study reported an average occurrence of LLJ of 28% for the month of July, based on 2 years of DWL observations (Tuononen et al., 2017). Outside Europe, a long-term study in Florida, USA, reported a 47% occurrence rate of LLJ during summer, based on 4 years of SODAR data (Karipot et al., 2009), and another work by Duarte et al. (2015) also reported a 47% occurrence rate in a summer study in South Carolina, USA.

During the study period, the LLJ core height (Z_{LLJ}) ranges between 238 m agl and 950 m agl (Fig. 3.4a), i.e., throughout the entire height range considered for detection (Section 3.2.3). Note that for the 7% of 30-min profiles, when the core height is detected at 238 m agl, the actual LLJ core may at times be located in the instrument blind-zone, i.e. below that level. Most jets (64%) have a core height between 300 and 500 m agl, with 350-400 m agl being the most common interval (22%). The median value of the LLJ core height is 388 m agl. These results are similar to previous case study analyses that found the core height of LLJ in the Paris region at 400 m agl (Klein et al., 2019) and compare well with observations conducted over Greater London that reported core heights between 300 and 400 m agl (Tsiringakis et al., 2022). The analysis carried out at Boulogne-sur-Mer, France (about 200 km north of Paris) reports LLJ core heights < 200 m (Roy et al., 2021). At this coastal site, it is likely that land-sea breezes play a role in the formation of the jet which might explain the occurrence of low-altitude core heights. At other European sites with coastal influence (Cabauw and Utö), lower Z_{LLJ} (140 m agl) were observed during the summer (Baas et al., 2009; Tuononen et al., 2017).

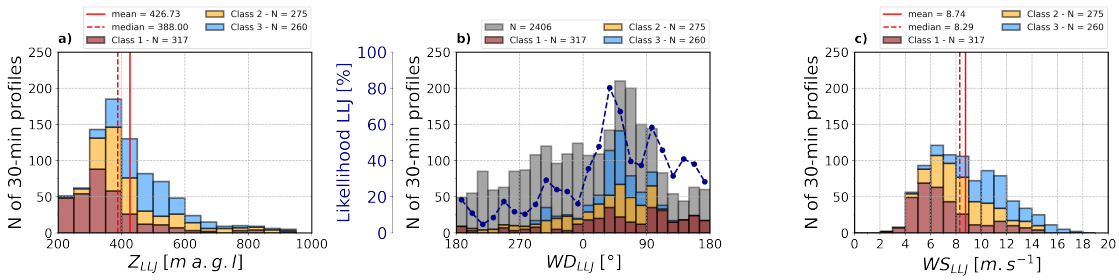

Figure 3.4 : Histogram of a) the LLJ core height (Z_{LLJ}), b) the LLJ core wind direction (WD_{LLJ}), and c) the LLJ core wind speed (WS_{LLJ}). The colors of the bars represent the vertical mixing (σ_w^2) classes as defined in Fig. 3.3. In b) the gray bars denote the wind direction distribution at 400 m agl for all nocturnal periods between 15 June and 31 August 2022, and the dashed dark blue line represents the likelihood of a LLJ being detected from a given wind direction. In the legend class 1 (red), 2 (yellow) and 3 (blue) correspond to low, medium and strong vertical mixing classes, respectively.

The histogram of the LLJ core wind direction (WD_{LLJ}) (Fig. 3.4b), shows that LLJs are mostly observed under Easterly-Northeasterly flow during the study period in summer 2022. 66% of LLJs have a core wind direction between $0°$ and $105°$, with $30°$-$60°$ being the most common interval. LLJ profiles with northwesterly flow ($300° < WD_{LLJ} \leq 360°$) present an occurrence of 12%, while southeasterly flow ($105° < WD_{LLJ} \leq 180°$) contributes $\approx$ 14% of the observed jets. The remaining 8% of the profiles are distributed in the interval $180°$ to $300°$. To assess how the LLJ over Paris relates to the general regional flow, the overall nocturnal wind direction distribution at 400 m agl (i.e. the level of the median Z_{LLJ}) is compared to the wind direction occurrence of LLJ events. The wind direction distribution of the LLJ follows a similar pattern as observed for the wind during the entire study period, where the northeasterly-easterly flow is predominant (44% of 2375 profiles). The likelihood of observing a LLJ is also higher in this sector with a 60% probability between $0°$ and $105°$, and the highest occurrence (80%) in the $30°$-$45°$ interval. Note that only two out of 46 jets (4%) present a southwest ($190°$-$300°$) wind direction, a sector that usually has a much larger frequency during summer nights with respect to the long-term climatology (2006-2022, Section 3.2.1).

Fig. 3.4c show that the LLJ core wind speed (WS_{LLJ}) varies between 2 ms^{-1} and 19 ms^{-1}. For the majority of the jets (85%), the core wind speed ranges between 4 ms^{-1} and 12 ms^{-1}, with a median value of 8.3 ms^{-1}. This is again similar to the modeling results of the two-day case study in Paris reported by Klein et al. (2019), and comparable to a climatological study conducted in Jülich, Germany, a suburban area located 370 km from Paris in the northeasterly direction where the median summer value of WS_{LLJ} is 8.3 ms^{-1} (Marke et al., 2018). Similarities are also found with Cabauw, The Netherlands (Baas et al., 2009), which is located in a suburban area 200 km from Paris in the northeasterly direction where the median value of WS_{LLJ} for summer is $\approx$ 9 ms^{-1}. Given that both Cabauw and Jülich are located roughly upwind of Paris under Northeasterly flow, all these sites could be affected by the same LLJ event if the phenomenon has a large enough spatial extent as shown e.g. by Klein et al. (2019), which could explain these similarities in LLJ wind speed. However, the question of spatial extent goes beyond the scope of the current study. The median WS_{LLJ} found in this study is lower than the wind speeds reported for the summer in Utö, Finland, 11.6 ms^{-1} (Tuononen et al., 2017), and results from a study in Florida, USA $\approx$ 10 ms^{-1} (Karipot et al., 2009).

3.3.4 LLJ signature in the vertical wind profile

As introduced in Section 3.3.2, a σ_w^2-based classification system is used to identify LLJ events with common characteristics, and then study their potential impacts on the near-surface atmosphere. Fig. 3.4 shows that low σ_w^2 is mostly related to jets with a low core height between 238-350 m agl, which in turn present predominantly east-southeast wind direction ($90°$-$180°$), and low to intermediate core wind speed <

7 ms^{-1}. It should be noted, however, that LLJ events with core wind speed > 10 ms^{-1} are also found in the low σ_w^2 class. These outliers are later discussed in Section 3.3.5. Jets with intermediate σ_w^2 occur mostly in two wind direction sectors: 300°-345° and 45°-105°. Their core height presents intermediate altitudes between 300 and 450 m agl, and wind speeds between 5-12 ms^{-1}. In the strong σ_w^2 class, the core height tends to be > 450 m agl, with a predominant northeasterly wind direction (30°-60°), and wind speeds > 8.3 ms^{-1}.

Fig. 3.5a presents the mean LLJ horizontal wind speed profile for each σ_w^2 class. Consistently with the histograms (see Fig. 3.4), the low σ_w^2 class present rather low values of wind speed throughout the profile. The core height of this profile is observed at 350 m agl and the wind speed at this altitude is 5 ms^{-1}. The minimum wind speed above the core is 3.8 ms^{-1} and occurs at 1000 m agl, above this height the wind speed gradually increases. Similarly, the mean wind profile for the intermediate σ_w^2 class presents a core height at a slightly greater altitude of 400 m agl, but with a slightly higher wind speed, about 6.2 ms^{-1}. The minimum above the core is close to that of the low-variance class. The mean profile associated with the strong σ_w^2 class exhibits a distinctly different shape and stronger wind speeds. The core height is located at 475 m agl, i.e. 75 m higher than the moderate σ_w^2 profile. The core wind speed is about 9.2 ms^{-1}, which is 50% and 30% stronger than the core wind speed for the low and intermediate σ_w^2 class, respectively. The minimum above the core is about 3.8 ms^{-1} and located at 1750 m agl, i.e. at greater altitudes than for the other two classes.

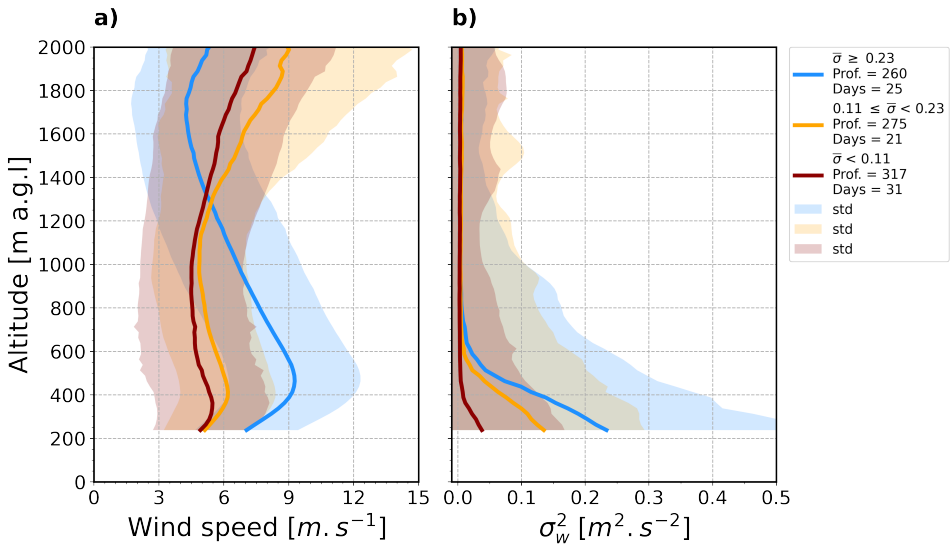

Figure 3.5 : Mean profiles of a) horizontal wind speed and b) median profiles of vertical velocity variance σ_w^2. The solid lines represent the composite profile with all 30-min profiles detected as LLJ, and the shadows denote 1±SD. Each panel presents the respective profiles for each σ_w^2 class: red is low σ_w^2, orange is moderate and blue is strong σ_w^2.

The respective median profiles of σ_w^2 for each class are presented in Fig. 3.5b, which illustrate that LLJ core height not only influences the horizontal wind speed

but also the vertical mixing. For all three median profiles, the strongest vertical mixing is retrieved from data recorded at the first range gate of the lidar (238 m agl), i.e. closer to ground level. Above this height, the median σ_w^2 values gradually decrease, reaching values close to zero, above the respective jet core shown in Fig. 3.5a. As the minimum recorded altitude of the vertical stare depends on the blind zone of the DWL, no information on the vertical velocity variance below 238 m agl is available. In general, the shape of the three median profiles agrees with those reported in previous studies (Banta et al., 2006; Bonin et al., 2015). In cities, unstable or neutral stratification and higher σ_w^2 are mantained by the added urban heat (Theeuwes et al., 2019).

To conclude, the classification system used here in this study allows us to identify the following trends: i) in the low σ_w^2 class the LLJ profiles are detected in a wind direction sector between $0°$ and $180°$. This class represents all the profiles detected in the southeast sector between $105°$ and $180°$, all the low altitude cases in the interval between 250 and 300 m agl, and is the dominant class for profiles with a core wind speed < 6 ms^{-1}. ii) The intermediate σ_w^2 class is detected in a wide wind direction sector between $300°$-$115°$, and dominates the northwest sector between $300°$-$360°$. The values of core height range between 300-450 m agl, while the core wind speed varies between 5-12 ms^{-1}. iii) Finally, profiles in the strong σ_w^2 class occur in the wind direction sector between $0°$-$115°$, but are usually found at the northeast sector between $30°$ and $60°$. LLJs in this category can present core height at high altitudes > 400 m agl with a strong core wind speed > 8.3 ms^{-1}.

3.3.5 LLJ nocturnal evolution

According to Stull (1988b), a LLJ typically forms during the night and reaches its maximum wind speed before dawn hours, between midnight and 4h local time. Fig. 3.6a presents an example of a well-defined nocturnal LLJ event observed in Paris during the night between the 16-17 July 2022, showing both the characteristics of the LLJ core and the minimum above. The WS_{LLJ} is about 7.5 ms^{-1} before sunset, then it increases and reaches its maximum (12.5 ms^{-1}) at 2.5 h after sunset (22h30 UTC and 00h30 LT), then starts to decrease again up from about 1 h before sunrise. The Z_{LLJ} is about 750 m agl at sunset when the convective boundary layer is still collapsing. When WS_{LLJ} starts to increase after sunset (21h UTC), Z_{LLJ} decreases to around 400 m agl and remains around this altitude throughout the night. At sunset, the jet core follows a northeasterly flow that veers toward the east over the course of the night by $90°$. The lack of sudden changes indicates that there are no changes in air mass.

The development of the wind speed minimum above the LLJ core (see Fig. 3.5a) and the evolution of its characteristics are in accordance with the momentum budget of the atmospheric column in the ABL during a LLJ event (Blackadar, 1957). The

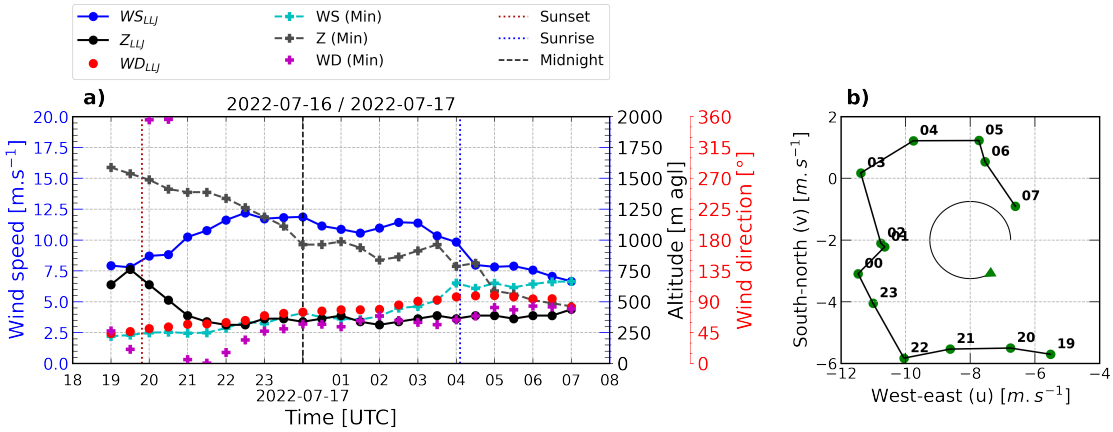

Figure 3.6 : Nocturnal evolution of an individual LLJ event (16-17 July 2022) with a) illustrating the jet characteristics: core wind speed (WS_{LLJ}) and the minimum above (WS_{Min}), core height (Z_{LLJ}) and the height of the minimum above (Z_{Min}), core wind direction (WD_{LLJ}) and wind direction of the minimum above (WD_{Min}); and b) the wind hodograph based on the meridional and zonal components of the wind (u, v) at the height of the core of the jet. The green arrow indicates the sense in which the wind is veering during the night (clockwise). Labels indicate the hour from 19h of 16 July to 07h of 17 July (UTC).

wind speed is weak ($\approx 2.5\,\mathrm{ms}^{-1}$) at sunset and then experiences a slight increase over the course of the night. The height of this minimum is located about 900 m above the LLJ core at sunset and then gradually decreases until it merges with the jet core at the time of the jet dissipation. The wind direction of the jet core and the minimum above differ by about $50°$ at sunset and then slowly converge over the course of the night before converging again at about 1 h past sunrise. Overall, the wind speed, wind direction and height in the jet core and the minimum above show distinct contrasts during the time of jet formation and then reach a common point at 7h UTC when the jet is completely dissipated and the momentum is distributed evenly over the entire column in the ABL.

This LLJ evolution (Fig. 3.6) suggests that the Inertial Oscillation (IO) is the formation mechanism of this event (Blackadar, 1957; Wiel et al., 2010). 28 out of 46 (61%) of the cloud-free detections reported in this study present a similar nocturnal evolution, which suggests that the IO is highly relevant for the jet dynamics in the Paris region. The IO is characterized by an oscillation of the wind above the elevated nocturnal temperature inversion with a period of $T = 2\pi/f$, where f is the Coriolis parameter ($f = 2\Omega \sin\theta$, with Ω and θ being the angular speed of the Earth's rotation and latitude, respectively). At the QUALAIR-SU latitude ($\theta \approx 48.84$), this gives $T \approx 16\,h$, which is approximately the duration of the most persistent LLJ events observed here, e.g. 7-10 August (see Fig. 3.8). The amplitude of this wind speed oscillation is related to the magnitude of the ageostrophic velocity component, and can cause the core wind speed to reach supergeostrophic magnitude. In addition to a gradual increase and decrease (*wind speed oscillation* hereafter) of the core wind

speed, the IO is associated with a clockwise change in wind direction, which is clearly evident from the time series (Fig. 3.6a) and also illustrated by the hodograph of the meridional and zonal wind components (u, v) (Fig. 3.6b).

Fig. 3.7 presents the nocturnal evolution of the core wind speed for the 46 jets observed under cloud-free conditions during the study period, classified into three groups of σ_w^2 intensity (section 3.3.2). In the low σ_w^2 class, 15 out of 19 (79%) cases do not show the wind speed oscillation, as opposed to four visible outliers (16 and 19 July, and 11 and 13 August). These outliers do not show common behavior in terms of duration, acceleration or peak wind speed. These cases are associated with a strong stable atmospheric stratification caused by the advection of hot air masses (Kotthaus et al., 2023), but these details are beyond the scope of this study and will be investigated elsewhere. Omitting those outliers, the behavior of the median wind speed curve for the low σ_w^2 class is rather flat with a mean value of 6.23 ms^{-1}. For the events with moderate σ_w^2 values (Fig. 3.7b), the median wind speed curve is stronger, with a mean value of 8.07 ms^{-1}. It increases slightly, starting from 2 h after sunset and reaches its maximum at about 4-5 h later, before starting to slowly decay until dissipation. Finally, for the strong σ_w^2 class (Fig. 3.7c) most of the events exhibit a clear wind speed oscillation in wind speed. The acceleration starts with the jet formation and lasts until 3 h after sunset. A peak in the core wind speed is observed at around midnight (±2 h), followed by a slow deceleration until dawn hours with a mean value of 10.2 ms^{-1}. The median WS_{LLJ} is 9 ms^{-1} at 1 h before sunset (i.e., in the order of magnitude as the peak of the wind speed median in the moderate σ_w^2 class) and then a gradual increase is produced until it reaches the maximum peak at 2 h after sunset, which lasts about 2 h. The WS_{LLJ} gradually starts to decay from about 4 h after sunset until it reaches a minimum right before sunrise, which is associated with the jet dissipation given.

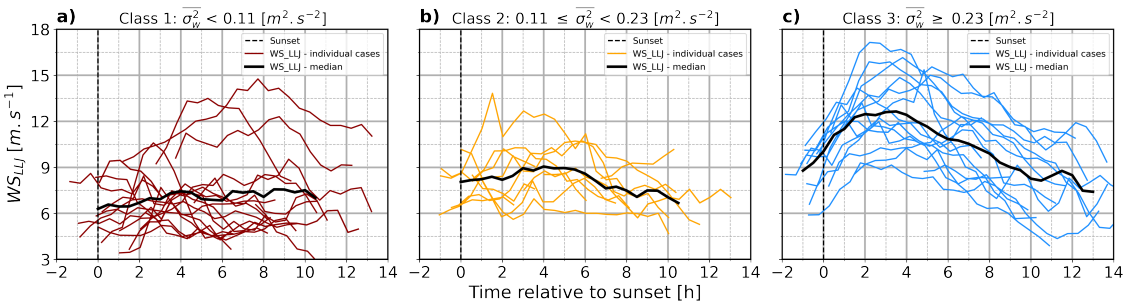

Figure 3.7 : The evolution of the core wind speed throughout the night for each LLJ event classified by a) low, b) intermediate, and c) strong vertical mixing. The black line represents the median for each group, which is calculated for times with a minimum of three samples.

3.3.6 Temporal distribution of the LLJ characteristics

Fig. 3.8 presents the time series of the nocturnal evolution for the three jet core characteristics (height, wind speed and wind direction) for each event during the

study period, including the cloudy nights. An amplitude in wind speed can clearly be identified for 25 out of 46 (i.e. 54%) jets, mainly observed for jets with strong vertical velocity variance (as shown in Fig. 3.7c) and high core height. This trend is also valid for short-duration cases (< 4 h), for example, 16 July. Nocturnal evolution of the core direction (Fig. 3.8b) shows that 28 out of 46 (i.e. 61%) of jets present a persistent clockwise veering with an average change in wind direction of $3.7° \, h^{-1}$. Two cases particularly stand out with a strong veering (> $5° \, h^{-1}$): 28 June and 21 August. They fall into the intermediate and low σ_w^2 class, respectively, and both emerge from a northwesterly direction ($322°$ and $282°$, respective initial core direction).

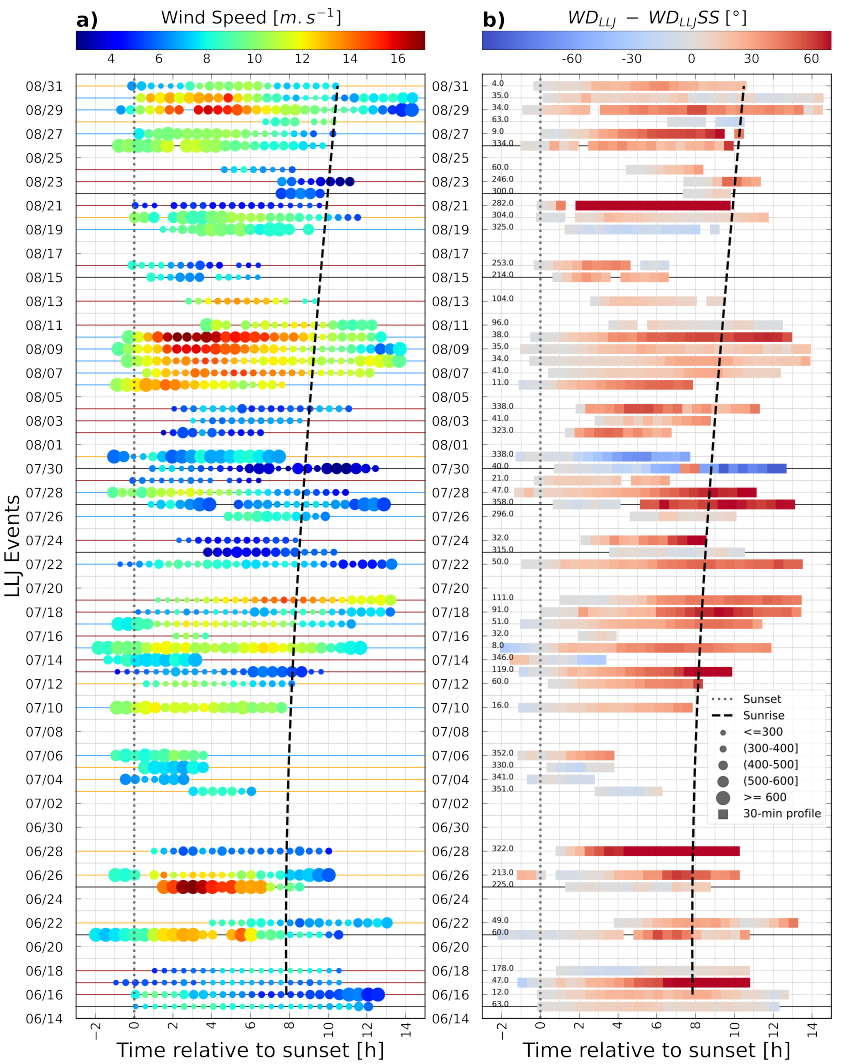

Figure 3.8 : Nocturnal evolution of the LLJ events during the study period 15 June - 31 August 2022 at 30 min resolution in time relative to sunset (dotted line). In a) dot size and color indicate the jet core altitude (Z_{LLJ}) and wind speed (WS_{LLJ}), respectively. Horizontal lines represent the vertical mixing category of each case: low (red), intermediate (orange), and strong vertical mixing (blue). b) Core wind direction (WD_{LLJ}) variability relative to the wind direction at sunset ($WD_{LLJ}SS$) or initial wind direction when the jet is formed in the middle of the night (indicated with the number inside the plot frame, at the left side). Horizontal black lines mark dates that are excluded from further analysis due to cloud conditions in a) and b). The dashed line marks the time of sunrise.

As discussed (Section 3.3.5), both the wind speed oscillation and the clockwise veering are signatures of the IO formation mechanism. However, not all cases with wind speed oscillation (Fig. 3.6a) present necessarily a strong clockwise veering (Fig. 3.6b). For example, jets detected between the 7 and 9 of August show the wind speed oscillation, but their change in core wind direction is less than $1°\,h^{-1}$, remaining almost constant in wind direction.

These time series showcase in detail the variability in the LLJ duration as well as the timing of both formation and dissipating. Results show that 29 out of 46

(i.e. 63%) jets last almost the entire night, emerging at sunset ±2 h and dissipating at sunrise ±2 h. However, jets can emerge in the middle of the night and continue even after sunrise. 31 out of 46 (i.e. 67%) cases last more than 8 h, including cases with late starting time (up to 4 h after sunset). During the study period, the maximum LLJ duration is 15 h, the minimum duration is 2 h (by conceptual definition), and the mean duration is 9.5 h.

The day-to-day variability highlighted in Fig. 3.8a reveals the influence of synoptic conditions for the LLJ characteristics. While some cases appear to be isolated (e.g. 28 June and, 10 July), during consecutive LLJ detection the characteristics of their core may vary night after night or may be similar each night. Ten events are detected between 10-19 July (heatwave period) with strong day-to-day variability in terms of σ_w^2 levels and the core characteristics. During this period, jets at high core height and strong wind speeds are associated with strong σ_w^2, while slow and low-altitude jets present weak σ_w^2. A different situation is observed for the seven jets detected between the 06-13 August. Persistent synoptic conditions prevail for the first five detections between 06-10 August, with similar nocturnal evolution of core characteristics and vertical mixing. However, the last two detections on the 11 and 13 August (outliers in Fig. 3.7) differ clearly from this period as they have short duration, low core height, weaker wind speed, and low vertical mixing.

The persistence of synoptic conditions results in a certain clustering of the LLJ events. For example between 15 and 18 June, four consecutive events present similar duration (10-12 h), with similar speeds (6-9 ms^{-1}), and similar core heights at altitudes (< 400 m agl). In the period between 6 and 10 August, the detected events present similar core characteristics with strong wind speed oscillation at high altitudes, occurring in the northeast flow with a wind direction veering becoming more pronounced from one night to the next. These cases present very similar nocturnal evolution and duration, and all of them fall into the same σ_w^2 class (strong vertical mixing). In the period between 3 and 6 July again, after four consecutive days with no detection, four short events (< 5 h) are found at medium to high altitudes between 400 and 600 m agl, with wind speeds between 10 and 12 ms^{-1}.

As discussed in Section 3.3.3, LLJ in a narrow easterly sector (80°-115°) are all associated with low vertical velocity variance. Fig. 3.8 reveals that these specific LLJ events (18 and 19 July, and 11 and 13 August) in fact present the high wind speed outliers detected in Section 3.3.5 with a distinct wind-speed amplitude (Figure 7a) and clockwise veering (Fig. 3.8b). It is further evident that these easterly jets are found at relatively low altitudes (< 350 m agl) suggesting a channeling along the low topography of the river Marne basin towards the East of Paris could play a role in the acceleration mechanisms. These processes will be investigated in future studies.

3.3.7 LLJ impacts on UHI

Cloudiness and wind are environmental variables that exert control on the intensity of the UHI and its nocturnal evolution. The UHI of the canopy layer is generally strongest during cloud-free nights and low wind speed conditions, following days with the same characteristics (Oke et al., 2017a). Fig 3.9a presents the relationship between the nocturnal mean surface wind speed at the urban park Montsouris and the nocturnal mean ΔUHI intensity in the Paris region, including only cloud-free nights after fair-weather days to focus the analysis on wind effects only.

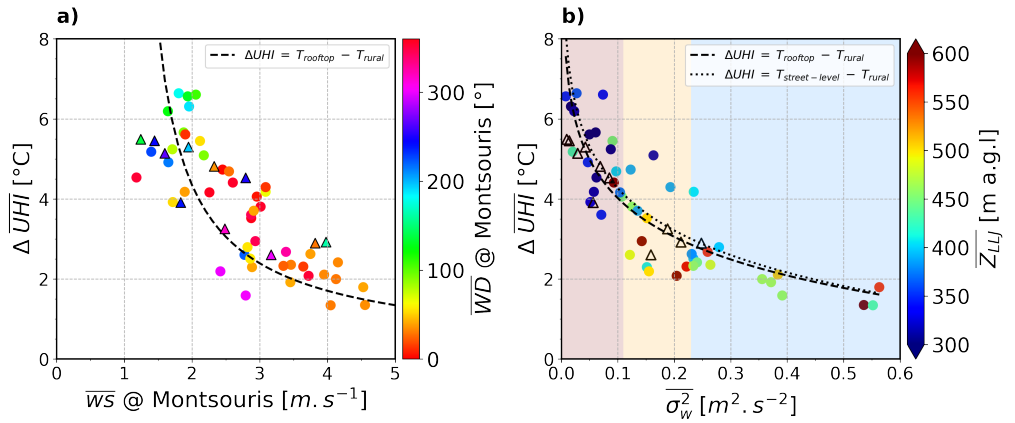

Figure 3.9 : Relations between nocturnal average of ΔUHI intensity for all cloud-free nights in the study period and a) 10 m agl wind speed at Montsouris park, an urban reference site. The dots are colored by surface wind direction at Montsouris. The dashed black curve is the best fit to the data: $y = 4((x - 1.1)^{-0.8})$, and it follows the empirical relationship described by Oke (1973) b) the vertical velocity variance (σ_w^2) at 238 m agl, dots are colored by the LLJ core height above the ground surface. The dashed black curve represent the best non-linear fit found for the data collected in the Paris region, and determining ΔUHI intensity with QUALAIR-SU data. The dotted black curve represents the same but using data collected by a surface-based station installed at Boulevard de Capucines for a shorter time period (see Section 3.2.4). Both curves represent the equation: $y = -1.39\log(x) + 0.84$. The background shading indicates the LLJ classes described in Section 3.3.2. In all subplots, dots and triangles represent nights with and without LLJ events, respectively.

Wind data at Montsouris park are observed at a tower 25 m agl, a measurement setting not often available in urban areas. The UHI intensity decreases exponentially with increasing wind speed. Based on observations from different cities in Canada, Oke (1973) proposed an empirical formulation where the mean ΔUHI is inversely proportional to the square root of the average regional nocturnal surface wind speed ($\Delta UHI \propto \overline{ws}^{-\kappa}$, κ being a dimensionless parameter often equal to 0.5). The urban wind direction at Montsouris suggests that weak values of ΔUHI are mostly found under northeasterly flow. This wind direction sector is characterized by LLJ with strong wind speeds and high σ_w^2 values. A best fit to the Paris data following this relation is included in Fig. 3.9a and describes a function that follows the drop in ΔUHI due to the increase in wind speed, with an asymptotic shape defined by

the threshold ΔUHI ∼1° C, which appears to be the baseline ΔUHI intensity for summertime cloud-free conditions.

The near-surface urban wind speed, sampled at a height (25 m agl) slightly above the mean building height of 20 m, provides insights on advection processes. However, to assess the role of vertical mixing on spatial contrasts in air temperature, the response of ΔUHI to the vertical velocity variance at 238 m agl is shown in Fig 3.9b. This relation is even more clearly pronounced as can be seen from the smaller error statistics listed in Table 3.2.

Table 3.2: Error metrics for prediction of ΔUHI intensity. In order of appearance from left to right: following the surface wind speed relationship proposed by Oke (1973), the best-fit model to urban and rural surface wind speed at Melun site and vertical velocity variance (σ_w^2) in the urban boundary layer above the roughness sublayer, respectively. The metrics are Mean Square Error (MSE), Root Mean Square Error (RMSE), Mean Absolute Error (MAE), and determination coefficient (R^2).

ΔUHI Estimator parameter	**urban surface wind**	**rural surface wind**	σ_w^2
MSE	2.18	2.89	0.65
RMSE	1.48	1.70	0.81
MAE	1.23	1.19	0.63
R^2	-0.18	-0.21	0.70

Given wind observations above the urban canopy layer (as here at Montsouris Park) are rarely available, the wind speed observations at the rural site Melun were also tested to have a full view of the ΔUHI response to the regional winds. As the rural near-surface wind speeds are associated with a higher uncertainty when predicting the ΔUHI, it is concluded that turbulence observations inside the urban boundary layer show a closer link to the processes that drive the UHI development. The curves in Fig 3.9b represents the best non-linear model fitted to the data collected during the nights with a LLJ event, using the T_{air} data collected at QUALAIR-SU. We also add the fit resulting from the data collected by the IOP station at Boulevard des Capucines (see Section 3.2.4). The similarity between the two curves shows that the relationship between ΔUHI and σ_w^2 is preserved even when using QUALAIR-SU data collected at roof-level.

These results are consistent with findings by Bonin et al. (2015) and Banta et al. (2006), who showed that the mixing below the LLJ core can affect the turbulent exchange processes near the surface. Table 3.3 presents a summary of the average values of ΔUHI and the LLJ characteristics, corresponding to each σ_w^2 class. Weak vertical mixing is associated with strong ΔUHI, calm winds and shallow core heights, whereas strong mixing relates to weak ΔUHI and strong wind speeds and greater core heights. Previous studies have shown that jets at low altitudes (up to 300 m agl) tend to present low to moderate core wind speeds (Banta et al., 2002;

Karipot et al., 2009; Carroll et al., 2019), so that weak wind shear only produces little mechanical turbulence.

The low-altitude jets are often associated with a strong temperature inversion over the rural surfaces, so that the stable stratification of the atmosphere leads to a more effective decoupling from the surface friction. For these conditions of strong atmospheric stratification and weak momentum transport by the LLJ, the cool air remains locally over the vegetated rural surfaces where it was generated through efficient radiative cooling during the cloud-free nights. Both advection and vertical mixing processes are weak and hence support the formation of very strong ΔUHI (Hu et al., 2013; Lin et al., 2022). Here we demonstrate that σ_w^2, obtained commonly at one measurement location at a height above the roughness sublayer but below the LLJ core, can be considered a representative indicator of the vertical mixing in the nocturnal urban boundary layer and hence a powerful predictor for the UHI intensity.

Table 3.3: Mean values of core height (Z_{LLJ}), core wind speed (WS_{LLJ}) and the corresponding ΔUHI for each class of vertical velocity variance (σ_w^2).

σ_w^2 **(m^{2}s^{-2})**	$<$ **0.11**	**0.11** $\leq \sigma_w^2 <$ **0.23**	$\geq$ **0.23**
WS_{LLJ} (m s^{-1})	6.2	8.0	10.1
Z_{LLJ} (m agl)	386	490	540
ΔUHI (C)	5.39	3.05	1.80

Note that the relation between ΔUHI and σ_w^2 remains valid even during nights when no consistent LLJ was detected by the automatic procedure (black triangles in Fig 3.9b), and other synoptic processes (such as fronts) are likely to modulate the atmospheric mixing. 53% of the jet-free nights fall into the low σ_w^2 class (red shading), and all show ΔUHI > 3.5° C. Future studies are going to investigate why there is no LLJ detected for some nights although a low σ_w^2 suggests a stable atmospheric stratification that is likely to favour decoupling.

3.4 Conclusions

This study presents the first comprehensive description of the characteristics of the summertime Low-Level Jet (LLJ) over the Paris region. LLJ events are detected automatically from continuous scanning Doppler Wind Lidar (DWL) measurements over the city centre, using a tailored algorithm amended from an existing method (Tuononen et al., 2017). A key feature of this study is the high temporal and spatial resolution of wind profile observations, which allow for LLJ variability to be captured in great detail. During the study period from June 15 to August 31, 2022,

LLJs were identified on 55 nights (70% of the nights). Notably, observations at an urban and a suburban sites reveal the regional nature of the LLJ, with 90% of events detected at both sites. This study focuses on nights with cloud-free conditions; hence, nine cloudy nights were excluded from the analysis, isolating 46 LLJ cases for detailed investigation.

As jets were rarely observed during the daytime, this work focuses on nocturnal jets between 18 and 09 UTC (20h and 11h local time). A comprehensive analysis of LLJ characteristics is presented here, including core height, wind speed, and wind direction. An exceptional predominant easterly and northeasterly flow during the summer of 2022 led to the detection of jets with mostly northeast flow origins (30°-60°), showing a mean core height of approximately 430 m agl. Very few LLJs were detected under a southeast and east flow (190° and 300°). On average the core wind speed is 8.9 ms^{-1} and in an range between 4 and 12 ms^{-1}.

To systematically assess the temporal variability of LLJs in the Paris region, both in terms of the nocturnal evolution and the night-to-night variability, we take a novel approach to classify LLJ events. Rather than grouping profiles according to the core wind speed, as is usually found in the literature, nocturnal events are defined with a certain continuity and then classified according to the magnitude of the vertical velocity variance (σ_w^2) below the jet core. Three LLJ classes (with weak, intermediate, and strong vertical mixing) were established based on the frequency distribution of σ_w^2.

It was found that these mixing classes are a clear indicator for the core characteristics (speed, height, temporal evolution) of most LLJ events, and tend to depend on the wind direction of the synoptic flow. Jets with low σ_w^2 are predominantly observed with flow from the south to southeast (105°-180°), at low altitudes (< 300 m agl) and with low to intermediate wind speeds (< 6 ms^{-1}). The intermediate σ_w^2 class is mainly found in the northwest sector (300°-360°), with intermediate core heights (< 450 m agl) and core wind speeds (< 8.3 ms^{-1}). Jets in the strong mixing class are primarily found under northeasterly flow, with most cases detected in a narrow sector (30°-60°) at high altitudes > 400 m agl and with strong wind speeds > 8.5 ms^{-1}.

The continuous DWL measurements and automatic detection provide novel insights into the nocturnal dynamics of the jets in the region. Most events persist from sunset to sunrise, with an average duration of ≈10 h, showcasing oscillations in core wind speeds that peak around midnight. Additionally, a prevalent clockwise wind direction veering was observed in 57% of cases, with an average change in wind direction of 3.7° h^{-1}. Notably, two outlier cases that fell into the intermediate σ_w^2 class exhibited a sharp eastward veering from the northwest, with low wind speeds and relatively low altitudes.

For LLJ events characterized by the distinct signature of oscillatory wind speed and core wind direction veering, the Inertial Oscillation (IO) formation mechanism is clearly evident. For others, changes in synoptic flow may cause variations in the geosptrophic wind that can mask this signature. The wind speed oscillation is found for most cases with strong σ_w^2 and medium to high wind speeds, while it hardly appears in weak LLJs with low σ_w^2. The wind direction veering occurs in all vertical mixing classes but is most pronounced in LLJs with strong σ_w^2. Four outliers with strong wind speeds and a late starting time in the low σ_w^2 class exhibit the oscillation signature. These cases, characterized by strong core wind speeds and low σ_w^2, are likely generated under very stable near-surface atmospheric stratification. Additionally, particularly low surface drag may favor the acceleration of these jets as they pass over a basin area of low topography east of Paris before reaching the urban site. Both the role of IO in LLJ formation over the Paris region and the impact of topography require further investigation.

In addition to the LLJ characterization, a key contribution of this work is the investigation of the impacts of the LLJ on the canopy layer Urban Heat Island (UHI) effect. The surface wind speed is a meaningful parameter that explains variations in UHI intensity, as they account for dynamic effects. Our results, however, reveal that σ_w^2 explains even more of the ΔUHI variability, as it also accounts for the mechanical mixing induced by the LLJ at the top of the nocturnal urban boundary layer. Using σ_w^2 as predictor results in a reduced Mean Absolute Error (MAE) of 0.63° C compared to the uncertainty when using surface wind speed to explain the ΔUHI variations (MAE = 1.23° C). The LLJ core wind speed does not sufficiently characterise the advection and mixing processes that reduce ΔUHI intensity, as highlighted by four outlier events (16 and 19 July, and 11 and 13 August) with strong core wind speeds and weak σ_w^2 that are among the nights with the strongest UHI. Although the LLJ is not the only source of mechanical turbulence, this nocturnal phenomenon certainly plays a key role in UHI development.

This study demonstrates that the regional-scale synoptic flow in form of the LLJ has clear implications for conditions in the urban boundary layer down to the surface. The mechanical turbulence driven by the LLJ significantly affects spatial contrasts in air temperature between the city and its surroundings and likely also influences the dispersion of atmospheric pollutants. In the summer of 2022, the LLJ was a very frequent phenomenon with variable characteristics that often suggest inertial oscillation plays a role in its formation. A better understanding of LLJ formation in response to synoptic pressure patterns and topography is required to fully grasp its interactions with the urban atmosphere.

Chapter 4

Impacts of topography and urban atmosphere on the LLJ

Contents

This chapter examines the spatial variation in the LLJ core characteristics induced by the surface properties of the Paris region. Two main drivers of the surface influence are considered here: topography and the enhanced buoyancy of the urban atmosphere. Topography acts as a natural barrier, mechanically altering both the horizontal and vertical wind flow (speed and orientation). While the surface of the Paris city is widely considered as flat (on average $30\,\mathrm{m\ asl}$), it is surrounded by plateaus with moderate elevations than are between 130-$150\,\mathrm{m}$ higher than the city (Fig. 2.1). Despite the low elevation of the Paris region, orographic conditions have been found to subtly influence the vertical movements of the ABL, particularly during springtime and when wind speeds are below $5\,\mathrm{m\,s^{-1}}$ (Troude et al., 2002). However, thermal forcing from the urban surface remains the dominant factor driving circulations within the city (Dupont et al., 1999; Lemonsu and Masson, 2002). Notably, no studies have assessed the combined effect of terrain and thermal forcing on the nocturnal summertime LLJ in the Paris region.

Case study analyses based on numerical simulations (Tsiringakis et al., 2022) and short periods of intensive observations using lidar or radar profiling (Wang et al., 2007; Barlow et al., 2014) have shown that the LLJ core height tends to be 20 to $100\,\mathrm{m}$ higher over urban areas compared to surrounding rural areas. Additionally,

LLJ wind speed near the urban surface can be lower than in suburban areas due to the enhanced surface roughness (Lemonsu et al., 2009). It should be noted that these studies find that the spatial variability of the LLJ core characteristics vary depending on the model used, and given these are case studies, the comparison of data collected between experimental sites is not representative of a general trend due to the limited dataset available for urban areas (Tsiringakis et al., 2022; Filioglou et al., 2022).

To assess the spatial variability of LLJ characteristics, DWL wind and turbulence observations collected during the summers of 2022 and 2023 are compared at two experimental sites: an urban location in the Paris city center and a suburban site at the SIRTA observatory (Section 2.2.1). Chapter 3 highlighted that the blind zone of the urban instrument ($150\,\mathrm{m}$ ($238\,\mathrm{m\ agl}$)) may limit the detection of shallow jets. In the Paris region, shallow jets occur predominantly from the east and southeast, under specific stable atmospheric conditions, often associated with strong UHI effects. To address this limitation, the vertical profile of horizontal wind within the DWL blind zone at the urban site was sampled using the novel shallow DBS scan (Section 2.2.4) during 2023.

This chapter is structured into four major sections. Firstly (Section 4.1), results from the shallow DBS are compared to those from the standard DBS and an approach is developed for the consistent concatenation of the two data sources. Secondly (Section 4.2) the LLJ characteristics at the two observational sites during the summers of 2022 and 2023 are summarised. Thirdly (Section 4.3) the spatial variations in LLJ core characteristics are assessed through a comparison between results obtained at the central urban and the suburban location on the Plateau Saclay. Finally (Section 4.4), key findings are summarised.

4.1 The shallow DBS evaluation

This section presents an evaluation of the novel shallow DBS retrieval results (effective display resolution $4.4\,\mathrm{m}$; first gate at $26\,\mathrm{m}$) against the standard DBS (display resolution $25\,\mathrm{m}$; first gate at $150\,\mathrm{m}$; see Section 2.2.4).

To exploit the Shallow DBS retrieval, the two profiles are concatenated at $150\,\mathrm{m}$ above the instrument. Given the low elevation angle of the shallow DBS, at this height the probed volume of air ($\approx 0.17\,\mathrm{km}^3$) and the scanned area ($\approx 2.28\,\mathrm{km}^2$) are considerably larger for the shallow DBS than for the standard DBS ($\approx 0.0003\,\mathrm{km}^3$ and $\approx 0.005\,\mathrm{km}^2$) (Fig 2.6c). The increased area coverage is likely to result in different levels of retrieval uncertainty. This is because it can lead to violations of the assumption of homogeneous flow, especially under unstable conditions, thereby increasing measurement uncertainty with height.

The wind flow in the sampled air volume can be influenced by the surface roughness heterogeneity, an effect that increases towards the ground and with the increased horizontal beam divergence (see Fig.2.6). This effect is presumably more important for the shallow DBS geometry. Therefore, the elevation angle used in this scan can introduce significant uncertainties in the wind profile product (Teschke and Lehmann, 2017; Tuononen et al., 2017; Rahlves et al., 2022). However, an in-depth, quantitative assessment of these uncertainties is beyond the scope of this study. Instead, a first-order evaluation comparing the horizontal wind products from both scans up to a height between 238 and $500\,\mathrm{m}$ agl is presented here.

Fig. 4.1 presents a comparison between wind measurements collected using the standard DBS at the first available gate ($150\,\mathrm{m}$ above the instrument and $238\,\mathrm{m}$ agl) and winds measured using the shallow DBS at the nearest corresponding height ($151\,\mathrm{m}$ above the instrument). The profiles were collected from June 1 to September 30, 2023. On average the comparison reveals a very good agreement between the two products (Root-Mean-Square Error-RMSE = $0.8\,\mathrm{m\,s^{-1}}$) with a slight underestimation of the horizontal wind speed by the shallow DBS (bias = $-0.26\,\mathrm{m\,s^{-1}}$). The small discrepancy is likely linked to the larger atmospheric volume and area probed by the shallow DBS.

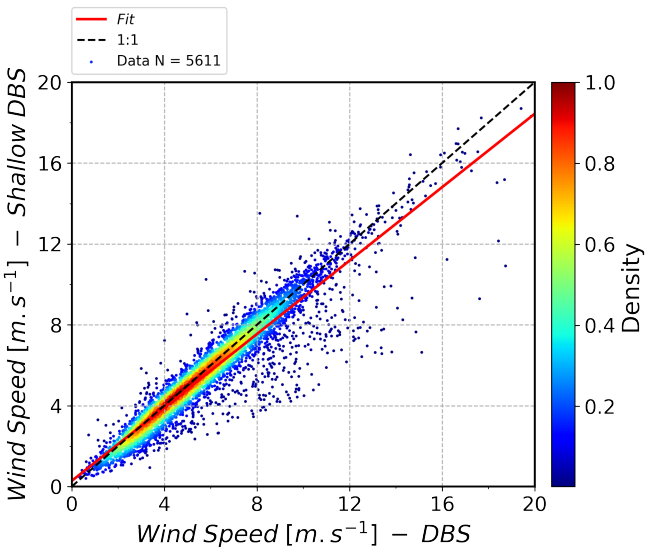

Figure 4.1 : 30-min averaged wind speeds recorded by the Shallow DBS and the standard DBS of the WindCube Scan 400s, at a height of $150\,\mathrm{m}$ above the instrument. The color scale represent the data density, the red solid line represent the linear fit to the data, and the dashed line represent the 1:1 diagonal of an ideal linear fit.

To assess whether the increasing volume and area of sampling with height affect the retrieval uncertainty of the shallow DBS, Fig 4.2 compares wind profiles obtained using the novel shallow DBS and the standard DBS up to a height of $500\,\mathrm{m}$ agl. The results indicate that the shallow DBS constantly underestimates wind speeds during daytime across the entire altitude range. This underestimation

is most pronounced between 8h and 15h UTC, when ΔWS start to show lower magnitude and variability in altitude due to changes in sunset time. To isolate the effect of atmospheric stability during the day, Fig. 4.2b presents the average daytime and night-time profiles. While the nocturnal differences are consistenly close to zero, the average daytime profile is negative and very slightly increases with height and beam divergence. This confirms that during unstable daytime conditions the assumption of homogeneous flow is less appropriate across the large area sampled with the shallow DBS.

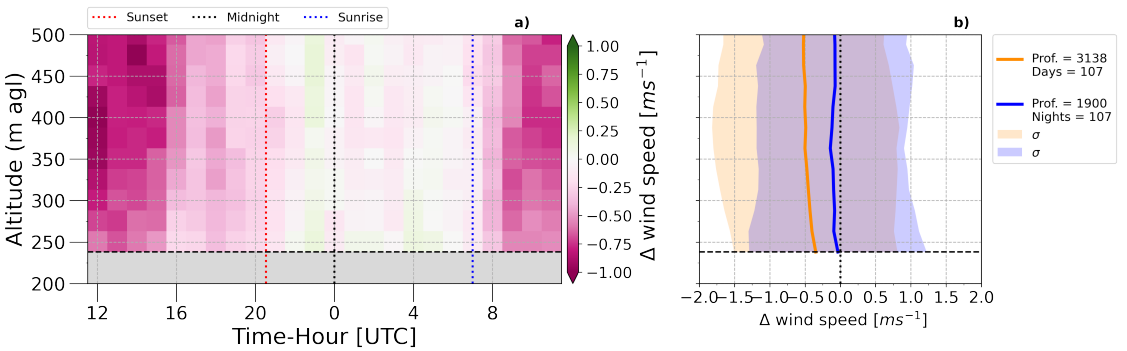

Figure 4.2 : Difference in wind speed (WS) profiles measured by the Shallow DBS and the standard DBS (ΔWS = Shallow DBS WS - DBS WS). a) A time-height diagram of the hourly average ΔWS profiles, and b) average daytime (orange solid line) and nighttime (blue solid line) ΔWS profiles, with shaded areas representing one standard deviation (σ). In both a) and b), the horizontal dashed black line indicates the first available measurement above the ground at $238\,\mathrm{m\ agl}$. Comparison period: June 1 2023 to September 30 2023. In total, 107 days included with 3138 (1900) profiles sampled during daytime (night time).

In contrast at night, the time-height diagram (Fig. 4.2a) shows that the shallow DBS retrieval can either underestimated or overestimated the wind speed regarding the standard DBS product. The values of ΔWS present a lower magnitude and can range between $-0.25\,\mathrm{m\,s^{-1}}$ and $0.25\,\mathrm{m\,s^{-1}}$. Unlike the daytime profiles, the ΔWS magnitude of the nighttime profiles does not increase with altitude. The average nocturnal profile (Fig. 4.2b) shows the values of ΔWS remaining very close to zero, with a maximum standard deviation of approximately $\pm 1.3\,\mathrm{m\,s^{-1}}$. These results indicate that the new shallow DBS presents a better performance during the night. Given this study focuses on nocturnal conditions and the shallow DBS profiles are intended for the automatic detection of the LLJ, the novel product is considered to provide valuable new data for LLJ analysis.

The shallow DBS profiles are concatenated with the standard DBS output to provide additional information within the blind zone of the latter, specifically between $26\,\mathrm{m}$ ($114\,\mathrm{m\ agl}$) and $150\,\mathrm{m}$ ($238\,\mathrm{m\ agl}$) above the sensor. In this study, the entire profile measured by the standard DBS scan mode is utilized, as it is the result of a well-tested scanning technique (Pearson et al., 2009; Drew et al., 2013; Liu et al., 2019; Thobois et al., 2019). Fig. 4.3 represent an example of concatenated profiles

during an episode of a shallow LLJ in the early morning of September 5, 2023. During the formation of the LLJ between 1h and 2h UTC, the shallow DBS profiles are slightly noisy, but exhibit wind speed magnitudes highly similar to those of the standard DBS profiles. During the peak of the LLJ, between 2h30 and 3h30 UTC, the shallow DBS profiles are smoother but tend to overestimate the wind speed at the height of the LLJ core.

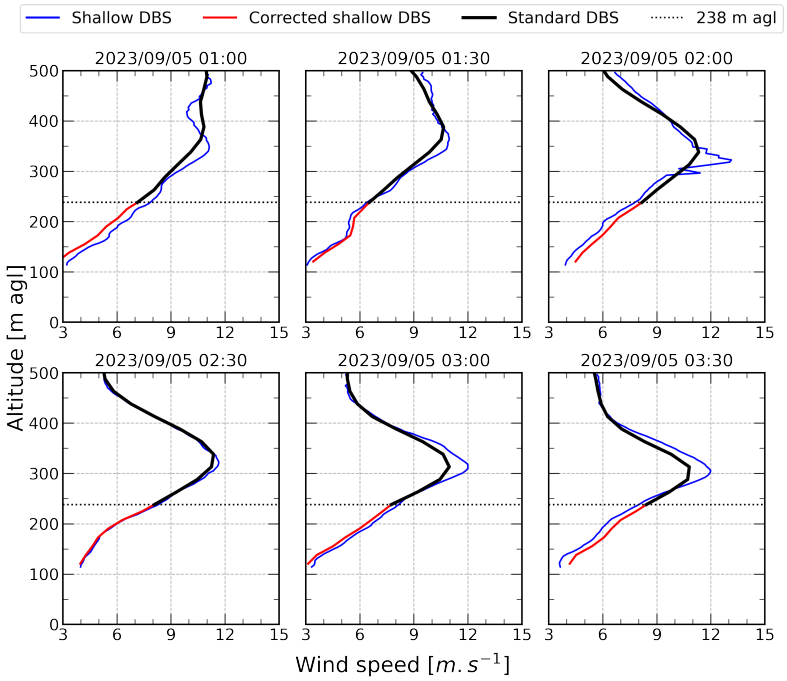

Figure 4.3 : Horizontal wind speed profile extended downward, resulting from the concatenation between the output of the standard DBS (black solid line) and the Shallow DBS (blue solid line). The red solid line represents the fraction of the Shallow DBS profile used for the extension of the horizontal wind speed profile. The profiles are measured during a Low-Level Jet episode. The horizontal dotted black line represents the first gate of the standard DBS outflow profile at 238 m agl.

To account for the small differences between the retrieval results (red line in Fig. 4.3) and to ensure continuity between the profiles, an additional minor correction is applied to the profiles obtained by the shallow DBS at the height of concatenation. The bias relative to the standard DBS at 150 m is subtracted from the shallow DBS profile, ensuring that the shallow DBS profiles are corrected according to this bias down to 238 m agl. The final step before concatenation involves smoothing the adjusted portion of the Shallow DBS profile. This smoothing is achieved by coarsening the spatial resolution of the profile using a moving average filter with a four-gate window (i.e., ≈17 m). The result is a concatenated profile that provides wind profile information within the blind zone of the lidar system.

4.2 The urban and suburban LLJ characteristics

This section provides an overview of the nocturnal summertime LLJ characteristics in the Paris region. Jet events detected during cloudy nights are excluded from further analysis, as the presence of clouds can disrupt the stable stratification of the near-surface atmosphere, thereby inhibiting the reduction of the frictional force exerted by the surface that drives the LLJ formation (Baas et al., 2009). Table 4.1 summarizes the cloud-free LLJ events detected at the two experimental sites.

Table 4.1: Summary of LLJ event detection frequency during summer 2022: June 15-August 31, and summer 2023: June 1-September 30.

LLJ frequency	**Summer 2022**	**Summer 2023**	**Total**
Number of nights	77	121	198
Site	Urban		
Number of jets	46 (60%)	41 (34%)	87
Number of 30-min profiles	852	646	1498
Number of hours	426	335.5	749
Average Duration (h)	8.7	7.3	–
Site	Suburban		
Number of jets	53 (69%)	58 (48%)	111
Number of 30-min profiles	998	1173	2171
Number of hours	499	586.5	1085.5
Average Duration (h)	8.9	9.6	–

The LLJ is a frequent nocturnal atmospheric phenomenon observed at both experimental sites. During the study period of 2022, more than 60% of the nights present a LLJ event with persistent characteristics over the course of the night (see Section 3.2.3), with an average duration exceeding $8.7\,\mathrm{h}$. However, during the 2023 study period, the frequency of LLJ events decreased compared to 2022, with notable differences between the sites. At the urban site, 34% of the nights exhibited an LLJ event with an average duration of $7.3\,\mathrm{h}$. In contrast, at the suburban site LLJ events were detected on 48% of the nights, with an average duration of $9.6\,\mathrm{h}$. These results suggest that LLJs are more likely to be detected at the suburban site, where they also tend to persist longer than at the urban site.

Fig. 4.4 presents the histograms for the three LLJ characteristics: core height (Z_{LLJ}), core wind direction (WD_{LLJ}), and core wind speed (WS_{LLJ}) observed at the two experimental sites. In the Paris region, the Z_{LLJ} ranges from 200 to $950\,\mathrm{m}$ above sea level (asl) (Fig. 4.4a). The minimum possible value of Z_{LLJ} is limited by the first gate level of the observations, which is determined by the blind zone of each instrument. At the suburban site, $\approx 1\%$ of profiles are detected at the height of the first measurement level ($256\,\mathrm{m}$ asl ($103\,\mathrm{m}$ agl)). At the urban site, during the summer

of 2022, ≈ 6% of profiles were detected at the height of the first measurement level (278 m asl (238 m agl)). After the implementation of the Shallow DBS, during the summer of 2023, 5.4% of jets were detected below this height and 0.6% at the first measurement level of the shallow DBS (154 m asl (114 m agl). This highlights the added value of the shallow DBS for a more accurate detection and characterisation of the Paris LLJ events that occur in the blind zone of the standard DBS.

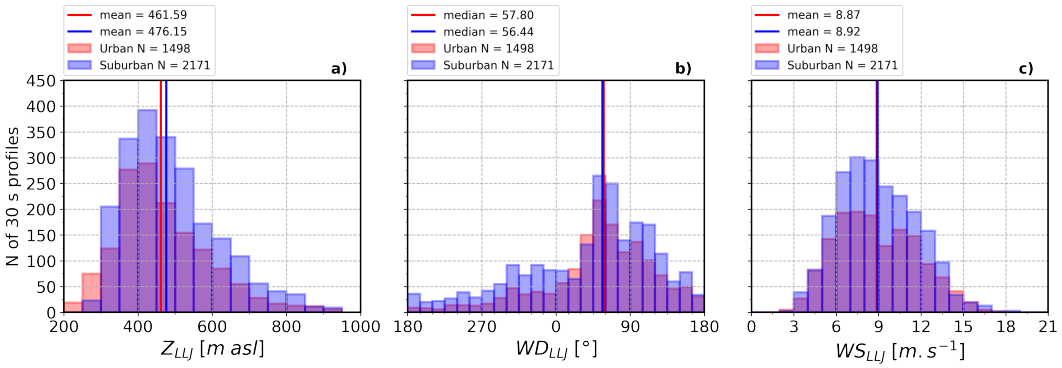

Figure 4.4 : Histogram of a) the LLJ core height (Z_{LLJ}), b) the LLJ core wind direction (WD_{LLJ}), and c) the LLJ core wind speed (WS_{LLJ}). Red and blue bars represent the data collected at the urban and suburban sites, respectively.

Fig. 4.4a shows that most jets at both experimental sites are observed between 300-550 m asl (≈ 250-500 m agl), a trend consistent with the observations at the urban site during the summer of 2022 as reported in Chapter 3. Despite the similarities, a slight difference is noted between the two sites: the Z_{LLJ} distribution at the suburban site tends to have higher values than at the urban site, with mean values of approximately 476 m asl for the suburban site and 460 m asl for the urban site. On average, the Z_{LLJ} is 16 m higher at the suburban site, a difference that is analyzed in detail further below (Section 4.3). This range of differences is similar to findings from a study conducted in the Greater London region, where the Z_{LLJ} at the urban site was observed to be approximately 20 m higher than at the rural site (Tsiringakis et al., 2022).

Fig. 4.4b show the occurrence of the WD_{LLJ}. The wind direction distributions are nearly identical at both experimental sites, indicating that the regional circulation patterns remain consistent across both sites, which are separated by 25 km. In general, the WD_{LLJ} distribution at both sites for 2022 and 2023 summer periods are similar to that found in 2022 for the urban site (Chapter 3). Most jet profiles are detected in northeasterly winds, with a median direction of 61°, accounting for about 1000 individual 30-minute jet profiles (≈25% of profiles at both urban and suburban) detected between 45°-75°. Northeasterly and northerly winds (300°-45°) are also frequent, contributing with approximately 30% of the profiles, similar to the contributions from easterly and southeasterly winds (75°-135°), which account for about 900 profiles (≈28%).

Notably, the detection of jets originating from the southwesterly (180°-270°) direction is quite rare, with this sector contributing the fewest jet-like profiles during the two study periods. This is particularly interesting given that southwesterly winds are typically prevalent during summer nights in the study area (Fig. 2.2a). While the summer of 2022 was notable for the absence of winds from this direction, the summer of 2023 followed the expected wind climatology (Fig. 2.2c), with a high frequency of southwesterly winds. Despite this, no significant increase in the frequency of jets from the southwest sector was observed, indicating that this sector is not representative for the formation of the regional jet.

Fig. 4.4c shows the WS_{LLJ} distribution. As for the WD_{LLJ}, the mean values of wind speed ($8.8\,\mathrm{m\,s^{-1}}$ for urban and $8.9\,\mathrm{m\,s^{-1}}$for suburban) suggest highly similar values for both experimental sites. The regional wind speed ranges between $3\,\mathrm{m\,s^{-1}}$ and $18\,\mathrm{m\,s^{-1}}$ with most profiles between $5\,\mathrm{m\,s^{-1}}$ and $13\,\mathrm{m\,s^{-1}}$. However, slight differences can be observed. A notable characteristic of the urban site is the lower occurrence of speeds in the 9-$10\,\mathrm{m\,s^{-1}}$ interval compared to adjacent intervals and the same range of speeds but at the suburban site. This pattern was already discussed for the WS_{LLJ} distribution reported for the summer 2022 (Chapter 3). In contrast, the WS_{LLJ} at the suburban site peaks between 6-$9\,\mathrm{m\,s^{-1}}$ and then it decreases monotonically.

4.3 The spatial variability of the LLJ characteristics

While LLJ characteristics are overall similar, the comparison of individual time periods (Section 4.3.1) reveals certain differences between the LLJ observed at the two sites. These differences are further examined and explained through a detailed wind sector analysis (Section 4.3.2).

4.3.1 Do the LLJ characteristics vary between the two experimental sites?

This comparative analysis focuses only on events detected simultaneously at both experimental sites. Fig. 4.5 presents a timeline of the detections under clear-sky conditions during the study period of 2022 and 2023, highlighting when simultaneous detection occurs. The LLJ cases from September 17, 18, and 20 were not detected at the urban site due to a lack of data caused by power and Ethernet network issues that occasionally disrupted the system's normal operation. To exclude potential effects associated with convective boundary layer dynamics during evening and morning transitions, only times between one hour past sunset and one hour before sunrise are considered. This results in a total of 2,596 individual 30-minute LLJ profiles, representing $1298\,\mathrm{h}$ of observations.

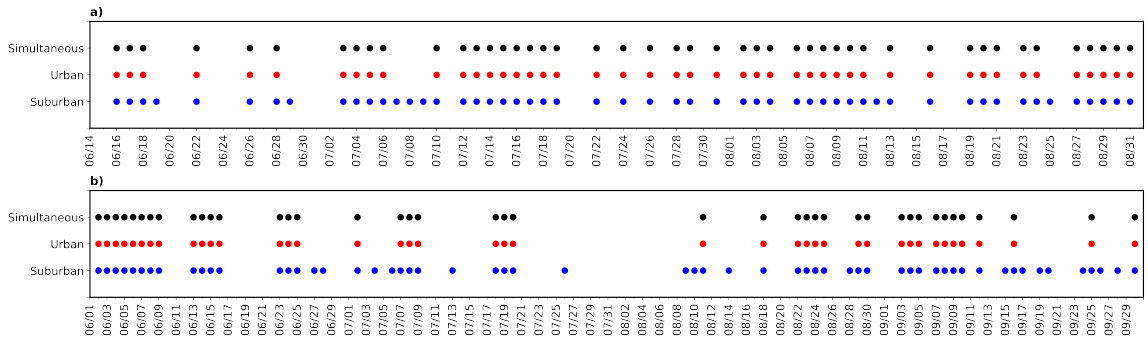

Figure 4.5 : LLJ events detected at the suburban site (blue dots), urban site (red dots) and simultaneous detections at both experimental sites (black dots) during a) the summer of 2022 and b) the summer of 2023.

Fig. 4.6 compares the three LLJ core characteristics for those selected profiles. Fig. 4.6a compares the values of Z_{LLJ} above the sea level, revealing differences in the LLJ core height between the two sites. Although there is high data dispersion (coefficient of determination R^2: 0.41), the density color map and the linear fit suggest that the LLJ core height tends to be observed at higher altitudes over the suburban site (Plateau Paris-Saclay) compared to the Paris city center. This result implies that some LLJs experience changes in Z_{LLJ} along its trajectory. As shown in Fig. 4.6b, the values of WD_{LLJ} are nearly identical at the two sites (R^2: 0.98), which means that the variability in Z_{LLJ} is not a result of sudden changes of the wind direction or possible detection of two different events. Finally, Fig. 4.6c compares the values of WS_{LLJ}. While there is a general tendency for the wind speed to be similar at both sites (R^2: 0.88), a slight variability is observed. Between 3 and $9\,\mathrm{m\,s^{-1}}$, winds are slightly stronger at the suburban site, whereas above $9\,\mathrm{m\,s^{-1}}$ winds tends to be slightly stronger in the city center.

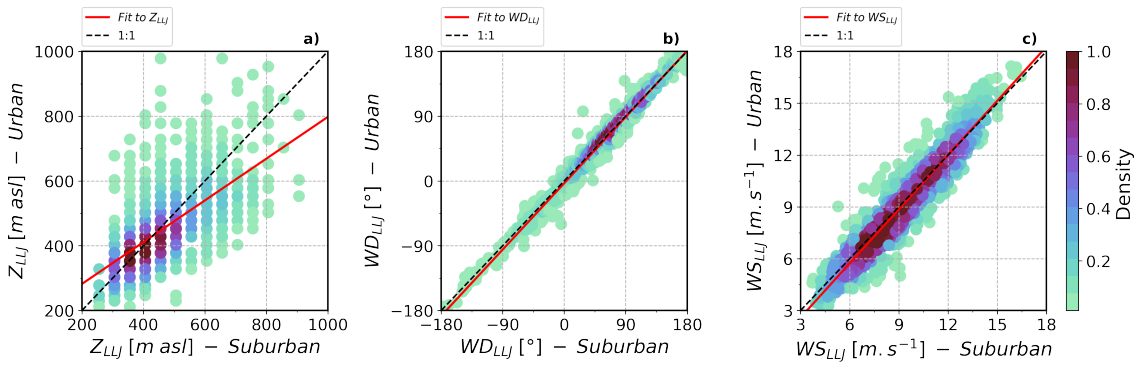

Figure 4.6 : Comparison of the LLJ core characteristics simultaneously detected at the suburban and suburban sites (see Fig. 2.1). The color scale represent the density of the data, the solid red line is the linear fit to the data ($y = ax + b$), and the dashed black line is expected perfect linear correlation 1:1. In a) the LLJ core height (Z_{LLJ}) with linear parameters of a: 0.64, b:155.21, in b) the LLJ core wind direction (WD_{LLJ}) with a: 1.02, b:-3.15, and in c) the LLJ core wind speed (WS_{LLJ}) with a: 1.04, b:-0.55.

Chapter 3 concluded that wind direction is a critical parameter as it influences not only the frequency of the LLJ but also its characteristics, which can vary depending on the wind direction. Moreover, previous studies have found that it is also important in determining how different surface types affect the magnitude of variations in LLJ characteristics (Pichugina et al., 2023). Although no changes are observed in the values of WD_{LLJ} between the two sites (Fig. 4.6b), further assessment is presented in Section 4.3.2 to investigate whether specific wind direction sectors can explain the observed variations in Z_{LLJ}.

4.3.2 Implications of the topography and the urban atmosphere

Four wind direction sectors (Fig. 2.1) are defined to simplify this assessment: northeast-east (NE) (blue shadow in Fig. 4.7), southeast-south (SE) (green shadow in Fig. 4.7), southwest-west (SW) (yellow shadow in Fig. 4.7), and west-northeast (NW) (red shadow in Fig. 4.7). These sectors have been defined based on the prevailing synoptic circulations (see Fig.2.2a), which determine specific patterns of atmospheric stability conditions and the regional LLJ core characteristics. Another criterion for defining these sectors is the spatial distribution of topography, which is mostly flat but shows a plateau of moderate elevation southwest of the city, and finally the spatial distribution of urban land cover fraction also plays a role in defining the sectors (Fig. 2.1).

Fig. 4.7a present the absolute Z_{LLJ} values for both experimental sites and Fig 4.7b presents the difference in Z_{LLJ} between the two sites ($\Delta Z_{LLJ} = Z_{LLJ}$ (Urban) $- Z_{LLJ}$ (Suburban)), both as a function of the urban wind direction. Results show that northern wind directions (i.e., west-north-east) are associated with high Z_{LLJ} values, exceeding the regional mean of $\approx$450 m asl (Fig. 4.4a), while southern sectors are below this regional value.

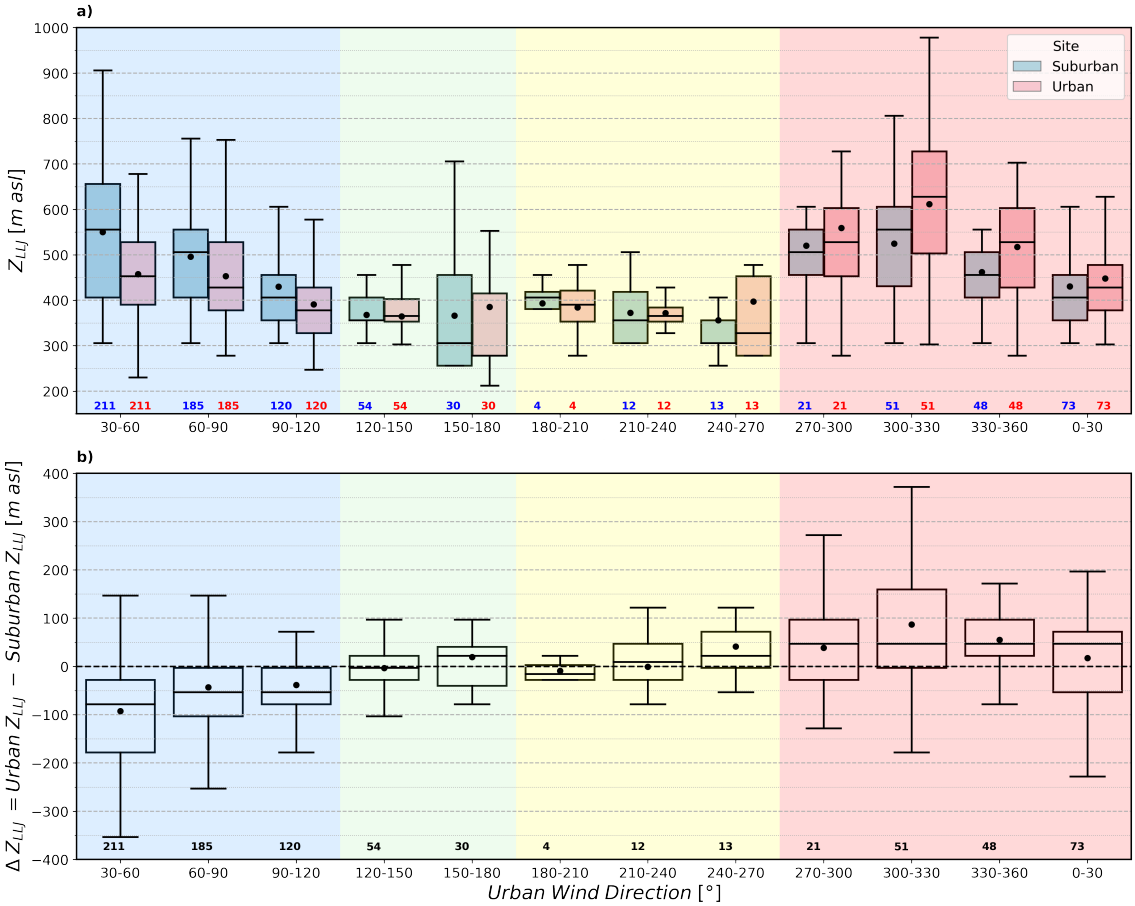

Figure 4.7 : Box plot diagram for a) absolute values of LLJ core height (Z_{LLJ}) above sea level (asl) at the urban and the suburban sites as a function of the urban wind direction, and b) differences (Δ) in Z_{LLJ} between the experimental sites. The colored number at the bottom indicate the sample size for each box: red for the urban site and blue for the suburban site. In b) the number at the bottom indicate the sample size for each box. In a) and b) the colored shadows represent the wind direction sectors previously defined in Fig. 2.1.

Although jets from the SW sector are observed much less frequently, this sector has been considered to assess whether the jet core height changes after moving across the entire Plateau Paris-Saclay to later interact with the urban atmosphere. As shown in Fig 4.7 (yellow shaded area), the ΔZ_{LLJ} values are close to zero, indicating no meaningful variation in the core height between the two experimental sites. Observed cases in this sector are characterized by low speeds and intermediate to high values of core height and vertical mixing (Chapter 3).

In the NE sector (blue shadow in Fig 4.7), the LLJ core height is higher at the suburban site, especially between 30°-60°. This interval also corresponds to the sector with the highest LLJ frequency and strongest core wind speeds (Fig. 3.4). Jets from this direction flow over the urban surface with relatively flat terrain and then interact with the edge of the Plateau Paris-Saclay, which presents a difference in ground height between 110 m and 130 m over a horizontal distance of less than

8 km (Fig. 2.1). After this interaction, the core of these jets, characterized by intermediate heights between 400-500 m asl (Fig. 4.7a), are shifted upwards due to vertical momentum transport. This interaction not only affects the height of the core but also its speed, resulting in a reduction of the LLJ core wind speed at the suburban site. However, the variability in both core height and speed is highly dependent on the absolute values of wind speed. Fig 4.8 shows that at the suburban site, for jets with speeds above $10\,\mathrm{m\,s^{-1}}$, the Z_{LLJ} values increase while the WS_{LLJ} values decrease as the wind speed increases. For speeds below $10\,\mathrm{m\,s^{-1}}$ differences in Z_{LLJ} and WS_{LLJ} are rather small. These results contrast with results of previous case-studies that concluded that jets are higher and slower over urban areas compared to suburban surroundings (Wang et al., 2007; Lemonsu et al., 2009; Barlow et al., 2014; Tsiringakis et al., 2022).

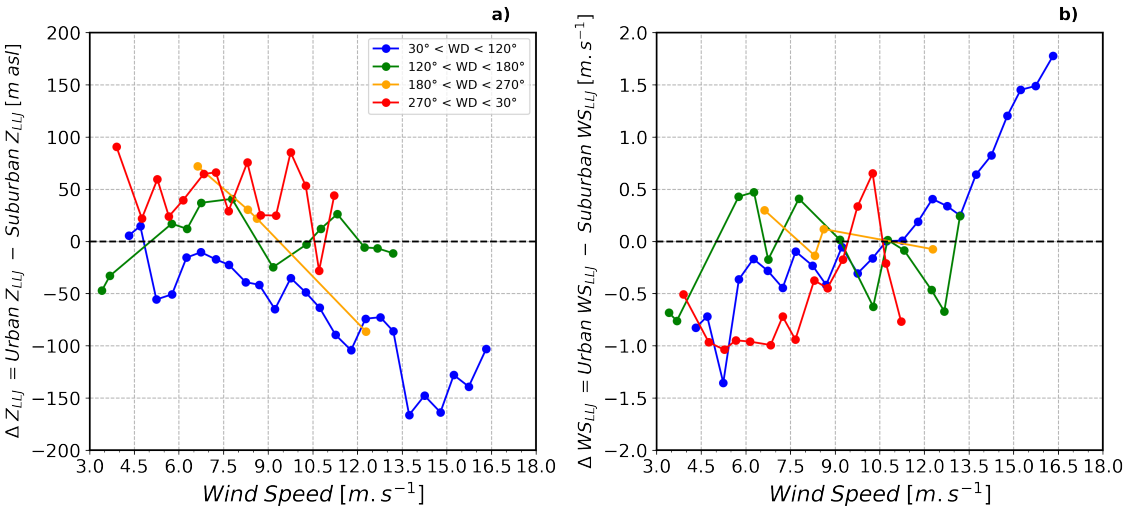

Figure 4.8 : Differences (Δ) in a) LLJ core height Z_{LLJ} and b) LLJ core wind speed WS_{LLJ} between the experimental sites as a function of the wind speed. Each line represent a wind direction sector.

Jet-like profiles observed in the SE sector (green shaded area in Fig. 4.7), are characterized by shallow core heights, typically falling within the low to intermediate range (Fig. 4.7a). Both Fig. 4.7 and Fig 4.8 show that the values of ΔZ_{LLJ} and ΔWS_{LLJ} are close to zero, as the LLJ core height and wind speed are similar at both experimental sites. This consistency holds even when occasional LLJs with strong wind speeds exceeding $9\,\mathrm{m\,s^{-1}}$. For instance, during the summer of 2022, cases on 16 and 19 July, and 11 and 13 August, presented strong wind speeds above $9\,\mathrm{m\,s^{-1}}$ with very shallow core heights below. These cases developed under similar conditions, characterized by a nocturnal stable layer (Chapter 3). When strong jets from this direction occur, regional atmospheric conditions are typically marked by strong stratification, leading to an almost complete detachment between the jet core and the near-surface atmosphere. This detachment occurs at a height that the topographical features of the region have little influence on the LLJ core

characteristics. This explains the lack of variability in the LLJ core height between the two sites.

In contrast to the NE and SE sectors, the NW sector (red shaded area in Fig. 4.7) exhibits LLJ-like profiles where the core height is higher at the urban site. This is particularly evident for wind directions between $300°$ and $330°$, where the highest Z_{LLJ} values ($> 400\,\mathrm{m\ asl}$) are observed. These elevated core heights might suggest minimal interaction between the LLJ core and the terrain. As shown in Fig. 3.1, jets from this direction pass over different terrain conditions before being observed at both experimental sites. At the suburban site, the jet predominantly crosses the Plateau, which presents a mix of urban and vegetated land cover. In contrast, at the urban site, the jet moves over flat terrain but is subject to the thermal forcing and enhanced surface roughness of the city. In addition, Fig 4.8a reveals that ΔZ_{LLJ} values exhibit little variability with increasing wind speed, indicating that jets from this sector are consistently higher at the urban site, which means that the wind speed do not affect the potential influence of the surface in the core height. However, Fig 4.8b shows that for wind speeds below $8\,\mathrm{m\,s^{-1}}$, these jets are always faster at the suburban site, while above this threshold, jets can be faster at the urban site. Previous studies concluded that urban buoyancy can lead to an increase in LLJ core height and a decrease of the LLJ core wind speed (Wang et al., 2007; Barlow et al., 2014; Tsiringakis et al., 2022). This effect may explain the spatial variability in ΔZ_{LLJ} and ΔWS_{LLJ} observed in this sector, where higher and slower jets are present over the urban site compared to the suburban location.

Through average profiles of wind speed and vertical velocity variance (σ_w^2) (Section 2.3.2), Fig. 4.9 summarizes the impacts of topography and the urban atmosphere on the spatial variation of LLJ characteristics. As previously mentioned, there is insufficient samples for the SW sector to conduct a thorough analysis. However, the average wind speed and the σ_w^2 profiles for both experimental sites are shown in Fig. 4.9e and Fig. 4.9f, respectively. In this sector, the wind speed profiles are quite noisy, and a clear average core is not discernible at either experimental site.

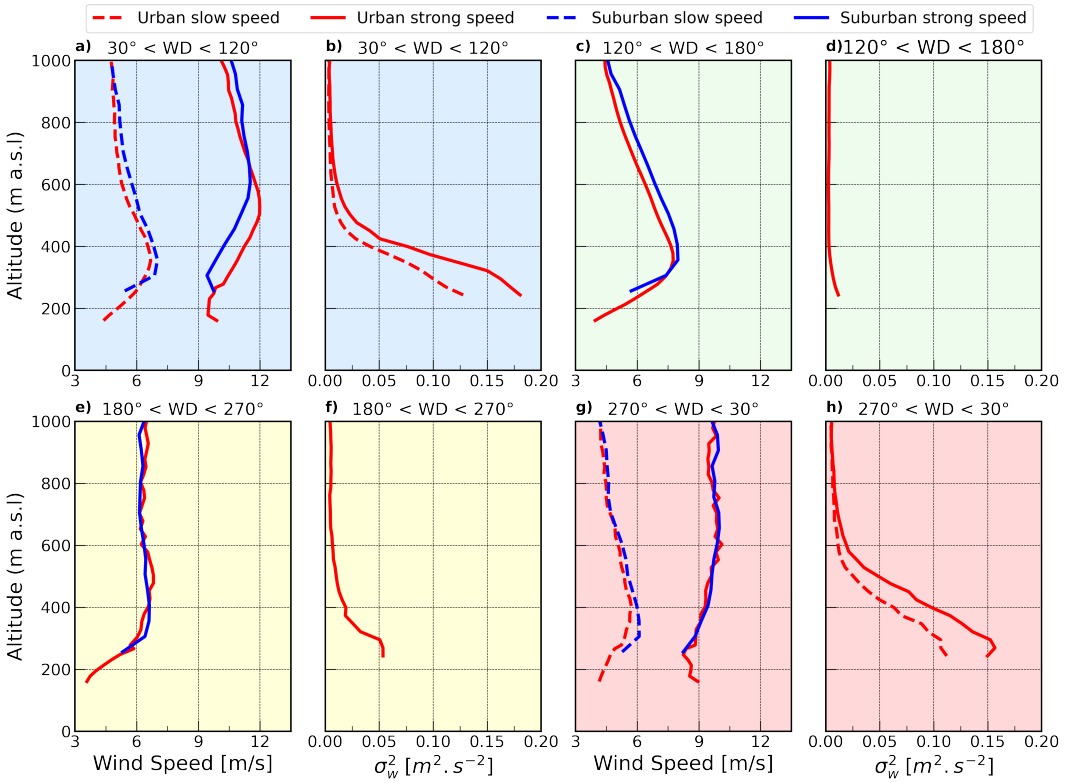

Figure 4.9 : Average profiles of the LLJ horizontal wind speed and vertical velocity variance (σ_w^2) for each experimental site and each wind direction sector for 2022 and 2023, only cloud free and simultaneous samples. In a) and b) the profiles are separated by wind speed values, the solid lines represent the group of strong winds above $9\,\mathrm{m\,s^{-1}}$ and the dashed line the group of speed below the threshold. In g) and h) the same but the threshold is $8\,\mathrm{m\,s^{-1}}$. The colored shadows represent the wind direction sectors previously defined in Fig. 2.1.

The mean wind speed profiles for the NE sector (Fig. 4.9a) show distinct behavior depending on wind speed. For wind speeds above $9\,\mathrm{m\,s^{-1}}$, the LLJ exhibits stronger wind speeds and a lower core height at the urban site compared to the suburban site, while the differences are minimal for slower jets. The stronger LLJs are associated with stronger vertical mixing, but also the slower jets still show considerable values of $\sigma^2 w$ (Fig. 4.9b). In both cases, the σ_w^2 profiles decrease gradually above the their maximum values at the lowest available measurement level ($238\,\mathrm{m\ agl}$). As discussed in Chapter 3, jets from the NE sector are associated with strong mechanically induced vertical mixing beneath the core.

In the SE sector, the average wind speed profiles at both sites are much sharper (Fig. 4.9c), with wind speeds decreasing more abruptly below the core height as they approach the surface. This indicates that, although strong horizontal shear is present, it has little impact on winds beneath the core due to decoupling caused by surface-based stable atmosphere conditions (Banta et al., 2006), resulting in very small values of the average σ_w^2 profile (Fig. 4.9d). On average, wind speeds are slightly stronger at the suburban site, with the profile's maximum also occurring at

a slightly higher altitude. This may be due to the temperature inversion defining the stable boundary layer being slightly higher at the suburban site, which is $140\,\mathrm{m}$ higher in elevation than the urban site.

Fig. 4.9g shows the mean wind speed profiles for the NW sector, grouped by wind speed intensity, with a threshold of $8\,\mathrm{m\,s^{-1}}$ based on the trend observed in Fig 4.8b. For profiles where the LLJ core wind speed is below this threshold, the suburban wind speed profile exhibits a stronger wind shear, with a maximum that is about $1\,\mathrm{m\,s^{-1}}$ stronger than the urban profile. However, the urban profile has a higher average core height, approximately $150\,\mathrm{m}$ above that of the suburban site. This difference can be attributed to the fact that the suburban atmosphere in the Paris region tends to exhibit nocturnal stable conditions (Dupont et al., 1999), resulting in a distinct average height where the jet core is unaffected by surface friction, whereas the LLJ core height at the urban site is influenced by urban thermal buoyancy. In contrast, for jets with core wind speeds exceeding $8\,\mathrm{m\,s^{-1}}$, there is no clear maximum wind speed, probably because there is more diversity of core heights. The profiles at both the urban and suburban sites are nearly identical, with no spatial variability in the LLJ core characteristics. The average σ_w^2 profiles (Fig. 4.9h) show higher values for stronger wind speeds, similar to those observed in the NE sector, suggesting significant thermally induced vertical mixing.

4.4 Conclusions

The analysis in this chapter shows that the topography and the enhanced buoyancy of the urban surface of the Paris region induce spatial variations in both the height of the summertime LLJ core and its wind speed. This surface influence is highly dependent on the wind direction, four wind direction sectors were found to define the different impacts of the surface on the LLJ core characteristics: northeast-east (NEE) (30°-120°), southeast-south (SES) (120°-180°), southwest-west (SWW) (180°-270°), and west-northeast (WNE) (270°-30°). It was found that σ_w^2 provides additional insights to explain why the topography effect expresses considerable variations.

Continuous observations of the horizontal wind collected by two Doppler Wind Lidars (DWL) and vertical velocity profiles collected at the urban site, were utilized to investigate the spatial variability of the LLJ core characteristics. One instrument, the WindCube Scan 400s, is located in the Paris city center (urban site) on the roof of a tall tower, while the other is situated $25\,\mathrm{km}$ southeast of the city at the SIRTA observatory (suburban site). This chapter evaluates two periods: summer 2022 (June 15 to August 31) and summer 2023 (June 1 to September 30), focusing exclusively on nocturnal measurements under cloud-free conditions.

Firstly, this chapter reports on the implementation of the novel shallow DBS. This technique, inspired by the standard DBS of the WindCube Scan 400s, extends the vertical profile of horizontal wind measurements downward by capturing radial velocity at an elevation angle of $10°$. The observations obtained using this method enabled the detection of jets with core heights below $\approx 280\,\mathrm{m\ asl}$, which is the lowest height measurable by the standard DBS technique due to the instrument's blind zone.

Jets originating from the NE sector exhibit a higher core height and reduced wind speed at the suburban site compared to the urban site. The difference in core height and wind speed between the sites increases as the wind speed increases. This effect is particularly pronounced in the wind direction sector between $30°$ and $60°$, where intermediate core heights (400–$500\,\mathrm{m\ asl}$) with strong speeds ($> 9\,\mathrm{m\,s^{-1}}$) are frequently observed. Under these conditions, after the LLJ core flows downwind over the city, it directly interacts with the natural barrier formed by the Plateau Paris-Saclay. This interaction causes vertical transport of momentum that shifts the jet core upward, while reducing the intensity of its horizontal wind speed. Additionally, the jets in this sector are characterized by efficient vertical mixing ($\sigma_w^2 \approx 0.335\,\mathrm{m^2 s^{-2}}$), driven by horizontal wind shear, which facilitates interaction between the jet core and surface features.

In contrast, jets originating from the SE sector typically exhibit shallow core heights (300–$400\,\mathrm{m\ asl}$) and low to intermediate wind speeds, which do not present high variability between the two experimental sites. Occasionally, jets with strong speeds ($> 9\,\mathrm{m\,s^{-1}}$) are observed in this sector, however, these are formed under stable atmospheric stratification with very weak average values of σ_w^2 ($\approx 0.051\,\mathrm{m^2 s^{-2}}$). This results in the jet becoming almost completely decoupled from the surface. In such cases, the jet core maintains a steady height without experiencing surface influence, as the maximum ground elevation in the study area is approximately $180\,\mathrm{m\ asl}$—well below the core height. Moreover, the buoyancy force of the urban surface is insufficient to disrupt the stable stratification.

The urban atmosphere was found to be an important factor in driving spatial variability in the LLJ core characteristics observed in the NW sector. In this sector, very high jets ($> 600\,\mathrm{m\ asl}$) with intermediate to low speeds ($< 9\,\mathrm{m\,s^{-1}}$) were detected at greater heights over the urban site compared to the suburban site, despite the urban site being located approximately $160\,\mathrm{m}$ below the highest ground level of the Plateau. The enhanced buoyancy force of the urban surface surpasses the mechanical turbulence generated by horizontal wind shear from these intermediate-speed jets, causing the jet core to rise above the urban surface.

Although winds from the SW sector are common in the study area, the proportion of observed jets in this sector is quite low, the synoptic conditions do not seem to be favourable for the LLJ formation. Due to the limited number of samples,

it is not possible to draw meaningful conclusions about the interaction of jet winds with the surface in this sector.

The findings presented in this chapter are a meaningful contribution to improve the understanding of the interaction between the summertime mesoscale Low-Level Jet, topography, and the urban atmosphere. Given the jet core characteristics can have substantial impacts on the regional distribution of heat, these results are also relevant to two potential fields of research: regional pollutant transport and the effects on wind energy production.

Chapter 5

Conclusions and Perspectives

Contents

This thesis examines the interactions between the nocturnal mesoscale flow and the Paris urban atmosphere. Results show that the nocturnal Low-Level Jet (LLJ) is a frequent phenomenon in the region during summer. It influences the canopy layer Urban Heat Island (UHI) intensity (i.e. the spatial air temperature contrast between the city and its rural surroundings), while urban-induced buoyancy can alter the height of the LLJ core and its wind speed. The detailed analysis of novel high-resolution wind profile observations highlights that atmospheric stability and vertical mixing play a major role in modulating the interactions between the regional winds, the topography and the urban atmosphere.

This chapter outlines the novel contributions of this thesis, which have a two-fold impact on both the experimental and scientific aspects, and can be described as follows:

1. Novel observations and methodological advances (Section 5.1): Multiple years of continuous wind and turbulence profile observations in a central urban setting were collected with high temporal and spatial resolution. This novel dataset was successfully developed based on multiple operational strategies applied to a scanning Doppler Wind Lidar (DWL) to monitor the urban wind field, along with the implementation of tools for geophysical parameter retrieval and data analysis.

2. Improved monitoring and process-understanding of the dynamics in the nocturnal urban boundary layer were achieved, with important implications for urban heat risk and pollution transport (Section 5.2).

Lastly, perspectives for future research are outlined. This thesis provides recommendations on experimental methodology and suggests new directions for applying the quantitative knowledge acquired, particularly in the fields of air quality and fog dynamics.

5.1 Novel observations and methodological advances

In the framework of this thesis, a high-power scanning DWLVaisala WindCube Scan (WCS) 400s was operated in the center of Paris, France, at the QUALAIR-SU supersite. Data have been collected continuously since January 12, 2022, using a combination of scanning modes: Doppler Beam Swinging (DBS), Plan Position Indicator (PPI), and fixed vertical stare. The scientific analysis in this thesis focused on two summertime study periods: June 15 – August 31, 2022, and June 1 – September 30, 2023. In addition to the central urban measurements, observations from a profiler DWL WLS70 were also utilized. This instrument has been continuously operating for over 10 years at the SIRTA atmospheric observatory, a suburban location $25\,\mathrm{km}$.

The deployment of the scanning DWL WCS 400s in the city marked a significant milestone in the development of the Paris region's Atmospheric Boundary Layer (ABL) observation network. Capturing continuous wind and turbulence profiles in the urban environment represents an essential step toward improving our understanding of the three-dimensional flow within the ABL and the variations between rural and urban settings. The continuous operation of this instrument resulted in a multi-year dataset now available for scientific analysis in various fields (e.g., supporting model evaluation or data assimilation activities by project partners, and development of material for teaching activities). The results of this thesis highlight the added value of continuous wind profile observations in urban settings, with the aim to extend these measurements in the framework of future projects. Given the collaborative nature of this thesis—engaging stakeholders from the public sector, academia, and industry—the collected data is publicly available, enabling broader impact on research and applications.

A comprehensive measurement strategy was designed to create a **novel dataset** capable of serving multiple research purposes. The resulting products include:

- 15-minute average vertical profiles of horizontal wind speed and direction, with the first measurement level above the instrument set at $150\,\mathrm{m}$ from January to October 2022, and at $26\,\mathrm{m}$ from November 2022 to the present.

- Two-dimensional horizontal maps of wind speed and direction at the height of the instrument (26 m above sea level (asl)), with four maps per hour from January to October 2022, and two maps per hour from November 2022 to the present.
- Average vertical profiles of vertical velocity and the corresponding variance, with two profiles per hour based on 5-minute sampling windows between January and October 2022; four profiles per hour based on 3-minute sampling windows from November 2022 to June 2024; and two profiles per hour based on 5-minute sampling windows from June 2024 onward.

The **methodological advances** of this thesis include:

1. The careful design and assessment of a multi-purpose scan strategy
2. The development of the new shallow DBS scan approach to sample the horizontal wind within the instrument's blind zone.
3. The development and implementation of an automatic tool for the detection and characterisation of the LLJ in vertical profile observations of horizontal wind.

The scan strategy implemented in this thesis involved capturing wind data using different scan patterns, including Doppler Beam Swinging (DBS), Plan Position Indicator (PPI), and vertical stare. Alternating between these scan patterns formed an hourly measurement schedule, enabling the three-dimensional dynamics of the Paris urban atmosphere to be recorded. A series of tests were conducted to evaluate the novel Volume Wind (VW) retrieval algorithm, developed by the manufacturer Vaisala (Thobois et al., 2015), for processing PPI observations. Findings and recommendations from this evaluation continue to support the advancement of the tool (Toupoint et al., 2024).

The novel shallow DBS scan reduced the limitations imposed by the lidar's blind zone (which spans 150 m in the setup used). This new approach involves sampling the atmosphere using the same geometrical composition of Lines of Sight (LOS) as the standard DBS but with a reduced elevation angle of 10°. With this technique, the horizontal wind profile can be sampled from a height of 26 m above the instrument (114 m above ground level (agl)), providing a 124 m downward vertical extension of the horizontal wind profile compared to standard DBS scan. This allowed for the detection of very shallow jets (< 240 m agl), which account for 7% of the LLJ events detected in this thesis. This new product can be implemented in any DWL WCS 400s installation or in any DWL equipped with a scanning head.

An automatic tool for the detection and characterization of the LLJ was developed based on the existing approach by Tuononen et al. (2017). A Python script was created to process data from any DWL in three steps:

1. Detection of LLJ signatures in the profiles of horizontal wind speed.
2. Determination of consistent LLJ events.
3. Extraction of LLJ core characteristics (height, direction and speed).

This tool will be integrated into the SIRTA operational processing system to further explore the LLJ occurrences in long-term historical data (with the WLS70 operational at SIRTA since 2012) and to provide near-real-time results on a daily basis.

5.2 Scientific achievements

The new data and methodological advances (Section 5.1) enabled an in-depth investigation of the nocturnal summertime LLJ in the Paris region to address key research questions (Section 1.6).

5.2.1 The summertime LLJ characteristics in the Paris region

The LLJ is a frequent nocturnal atmospheric phenomenon in the Paris region, though it exhibits significant inter-annual variability. During the summer of 2022, LLJ events were detected on 70% of the nights over the city, with 90% of these cases simultaneously observed at the suburban site, where seven additional cases were recorded. In contrast, the occurrence of LLJs was notably lower in the summer of 2023, with a higher frequency observed at the suburban sites (48% of nights) compared to the urban site (41%).

These inter-annual differences are largely explained by the synoptic flow conditions. Based on a 10-year climatology, the Paris region experiences two predominant wind directions at night: winds from the southwest carrying maritime air and winds from the northeast with a more continental influence. In summer 2023, winds were consistent with this climatology. However, summer 2022 exhibited an anomalous pattern dominated by a series of synoptic blocking events, leading to extreme heat waves over central and western Europe. During this period in the Paris region, winds predominantly came from the north to northeast, with minimal southwestern flow. It is hence concluded that the northerly and easterly flows, associated with high-pressure systems, not only favored the development of heat waves but also increased the occurrence of LLJ events.

At both sites, the LLJ core height ranged from $200\,\mathrm{m\ asl}$ to $950\,\mathrm{m\ asl}$. While the average heights were similar overall, jets were slightly higher above the city when considering ground level as a reference, due to the suburban site being located on a plateau approximately $130\,\mathrm{m}$ higher than the city. The minimum detected height is influenced by the instrument's blind zone, but the implementation of the shallow DBS technique improved the monitoring of shallower jets in summer 2023. LLJ

core wind speeds ranged from approximately $3\,\mathrm{m\,s^{-1}}$ to $18\,\mathrm{m\,s^{-1}}$, with most jets exhibiting speeds around $9\,\mathrm{m\,s^{-1}}$. The regional LLJ has an average duration of $8.6\,\mathrm{h}$, with most jets forming around sunset and dissipating after sunrise.

The analysis of the LLJ core wind direction revealed that most jets originated from the northeast (primarily between $30°$ and $60°$), followed by jets from the southeast and northwest. Fewer than 7% of jets were observed under southwesterly flow, even during the summer of 2023, when winds from these directions were generally more frequent. This suggests that the synoptic conditions associated with southwesterly winds are the least favourable for the formation of low-level jets.

Wind direction was found to not only modulate the frequency of LLJ occurrence but also has a strong influence on the core height, core wind speed, and the intensity of vertical mixing below the jet core (see Section 5.2.2). The latter is here quantified through the vertical velocity variance (σ_w^2) estimated by the vertical velocity profiles collected by the DWL at the urban site. Related studies, which also exploited the DWL observations gathered as part of this research (Haeffelin et al., 2024; Kotthaus et al., 2024), demonstrated that this indicator of vertical mixing aligns well with thermodynamic variables related to atmospheric stability. As expected, σ_w^2 was weaker under stable atmospheric stratification. A novel LLJ classification approach was developed in this thesis, based on the σ_w^2 values obtained at the first measurement level of the DWL in the urban setting. This method was found to be the most suitable in classifying LLJ events into distinct groups that were consistent with respect to their core height and velocity.

In the summer of 2022, LLJ events in the high vertical velocity variance class (nocturnal average $\sigma_w^2 \geq 0.23\,\mathrm{m^2 s^{-2}}$) were generally strong ($> 9\,\mathrm{m\,s^{-1}}$) and occurred at higher altitudes ($> 450\,\mathrm{m\,asl}$). Jets in the medium variance class ($0.11\,\mathrm{m^2 s^{-2}} \leq \sigma_w^2 < 0.23\,\mathrm{m^2 s^{-2}}$) presented core heights between 350 and $450\,\mathrm{m\,asl}$, with wind speeds ranging from $5\,\mathrm{m\,s^{-1}}$ to $12\,\mathrm{m\,s^{-1}}$. Lastly, events in the low variance class ($\sigma_w^2 < 0.11\,\mathrm{m^2 s^{-2}}$) were dominated by weaker winds ($< 8\,\mathrm{m\,s^{-1}}$) at lower altitudes ($< 350\,\mathrm{m\,asl}$). The frequency of these variance classes varied significantly with wind direction. LLJ events with high variance were almost exclusively associated with northeasterly flow, while those with medium variance occurred under northwesterly to northeasterly circulations. Low variance events were observed across a broader sector, between $0°$ and $180°$.

LLJ events in the high-variance class particularly exhibited characteristics typical of the inertial oscillation formation mechanism (Blackadar, 1957). Their wind speed showed oscillations during nocturnal evolution, with a rapid increase in speed, reaching a peak around midnight, followed by a slower weakening of the flow until the jet dissipated after sunrise. These oscillations were often accompanied by a clockwise veering of the wind direction, averaging $3.7\,°\,\mathrm{h^{-1}}$. In some cases,

changes in synoptic flow likely altered the geostrophic wind, which may have masked the characteristic signatures of inertial oscillation.

5.2.2 The LLJ impact on nocturnal urban heat

A series of extreme heat events affected the Paris region during the study periods of summer 2022 and 2023. At night, air temperatures in central Paris were up to ≈ 8°C higher (hourly maximum) than those at a rural reference site, showing the formation of the canopy layer UHI (ΔUHI = T_{urban} - T_{rural}) (Section 1.3). During these heat waves, LLJ events were frequent, and a clear relationship was established between LLJ characteristics and night-to-night variations in ΔUHI. The σ_w^2-based classification system demonstrated that UHI intensity increased as σ_w^2 values decreased. Strong ΔUHI was detected only in cases of LLJs with extremely weak vertical mixing. These conditions were predominantly observed under southeasterly flow, whereas LLJs with high variance and lower UHI intensities occurred under northeasterly winds.

The LLJ can influence the spatial temperature contrasts through different processes, such as horizontal advection of cooler rural air, entrainment, and mixing. The impact of these processes depends on the attachment between the LLJ core and the surface, which is governed by atmospheric stability conditions. Under increased atmospheric stratification, the LLJ flow detaches from the rough urban surface, allowing high LLJ velocities to occur while near-surface winds remain calm during stable conditions. As a result, the cooler air transported by the jet stays aloft and is neither advected to ground level nor mixed downward into the urban canopy layer. As a result, the LLJ core wind speed alone does not fully characterize the advection and mixing processes that modulate ΔUHI. Certain cases revealed strong core wind speeds paired with weak σ_w^2, leading to strong UHI intensities.

Thus, σ_w^2 is a significant parameter for explaining variations in UHI intensity, reducing the Mean Absolute Error (MAE) to 0.63°C, compared to an MAE of 1.23°C when using surface wind speed as a predictor for temperature contrasts. Although the LLJ is not the only source of mechanical turbulence in the ABL, these findings highlight the critical role this nocturnal phenomenon plays in contributing to stagnation in the near-surface atmosphere. This has important implications for urban heat risks and beyond (implications for e.g. air quality will be investigated in future studies).

5.2.3 The response of the LLJ to topography and urban buoyancy

As concluded for the LLJ's impact on urban heat island intensity (Section 5.2.2), the response of the LLJ to spatial variations in topography or the presence of the urban boundary layer also depends partly on the degree of vertical momentum exchange between the near-surface atmosphere and the LLJ. By grouping LLJ events into wind

direction sectors aligned with the topographical features of the Paris region, the following conclusions were drawn regarding the surface's influence on the LLJ flow speed and core height, the latter serving as a proxy for the nocturnal boundary layer height (with implications, for example, for processes such as pollutant transport and mixing).

Jets from the northeast sector exhibited higher core heights and lower wind speeds at the suburban site (downwind of the city) compared to the urban site. These differences increased as LLJ core wind speed increased. This effect was particularly pronounced in the $30°$ to $60°$ wind direction range, where intermediate core heights (400–$500\,\mathrm{m\ asl}$) with strong speeds ($> 9\,\mathrm{m\,s^{-1}}$) were common, producing high values of σ_w^2. As the LLJ core encounters the edge of the Plateau Paris-Saclay downwind of the city, momentum is transported vertically, whereby elevating the jet core height and reducing its horizontal wind speed.

Jets from the southeast sector generally exhibit minimal variation between the two experimental sites. Occasionally, stronger jets occur, but they form under very stable stratification with extremely weak vertical mixing ($\sigma_w^2 \approx 0.051\,\mathrm{m^2 s^{-2}}$), resulting in the LLJ flow being strongly detached from the surface (as discussed in Section 5.2.2). In such cases, the jet core remains unaffected by topography, as the maximum ground elevation ($180\,\mathrm{m\ asl}$) is well below the core height, which ranges between 250 and $350\,\mathrm{m\ asl}$. Additionally, the urban surface buoyancy is too weak to break the atmospheric stratification.

In the northwest sector, the urban atmosphere plays a role in driving spatial variability in the LLJ core characteristics. In this sector, very high jets ($> 600\,\mathrm{m\ asl}$) with intermediate to low speeds were detected at greater heights over the urban site compared to the suburban site, even though the urban site is approximately $150\,\mathrm{m}$ lower than the highest ground level of the Plateau. For LLJs with moderate wind shear and variance conditions, the added nocturnal buoyancy over the urban surface causes the jet core to be at a higher height above the city. As a result, pollutants in the nocturnal urban boundary layer can disperse over a larger volume compared to the suburban location, where the LLJ core height difference is about $100\,\mathrm{m\ asl}$ and $60\,\mathrm{m\ asl}$.

5.3 Perspectives

This thesis, through a field experiment using two DWL systems, advanced the quantitative knowledge of the feedback interactions between summertime LLJ characteristics, topography, and the urban atmosphere. A key finding is that the vertical transport of momentum below the jet core plays a significant role in influencing the dynamics of the LLJ's interaction with its environment. As this

vertical mixing is largely driven by synoptic conditions (e.g., subsidence), LLJ characteristics vary highly with wind direction.

One DWL system was installed in central Paris, while the other is located $25\,\mathrm{km}$ southeast, downwind of the city center. These instruments are aligned along the transect of the region's prevailing winds. However, additional spatial coverage, particularly in the upwind northeast sector where most jets originate, could further strengthen the analysis. It is therefore recommended to exploit data collected by another DWL system installed at the Roissy airport supersite, located northeast of the city. This would provide a valuable opportunity to investigate the spatial variability of LLJ characteristics in greater detail, particularly along the direction of the highest LLJ occurrence during summer.

Future investigations should consider that jets originating from the southeast sector exhibit different dynamics compared to other wind directions. In the southeast sector, atmospheric stability plays a more meaningful role in influencing the LLJ core characteristics, while the northeast sector is more affected by topography. A key question arising from the presented analysis is: What are the different physical mechanisms behind the formation of the observed LLJ in the Paris region? Addressing this question could provide further valuable quantitative knowledge of the formation of southeast-originating LLJs and improve the understanding of their impact on near-surface processes, such as heat distribution. Therefore, it is recommended to deploy a DWL in the southeast region, given it would provide an opportunity for detailed study of the complex dynamics of jets in this area.

Beyond the LLJ's impact on the spatial contrast of heat between urban and rural areas, there are additional research tracks that could be explored to enhance the understanding of the LLJ's relationship with the urban environment, particularly in critical fields of environmental health and human activities. These include:

- **Implications of LLJ and ABL dynamics for pollutant transport:** while a vast body of scientific literature focuses on urban air quality by examining wind dynamics below the urban canopy layer, less attention has been given to the influence of ABL dynamics on this issue. The ABL forms in response of a combination of both synoptic meteorological conditions and surface-induced processes. Therefore, to better understand pollutant transport in cities, it is essential to consider mesoscale circulations, such as the LLJ.

  The LLJ can enhance both horizontal and vertical transport, influencing the dilution of pollutants in urban areas through advection and vertical mixing. Therefore, it is crucial to quantify the LLJ's impact on vertical dilution and the entrainment of air from the free troposphere, upper layers, or residual layers into the urban boundary layer. Additionally, the role of horizontal advection of fresh or polluted air must be explored. This is particularly relevant for a city

like Paris, which frequently experiences long-range transport of aerosols from biomass burning, desert dust storms, industrial emissions, and agricultural activities. The presence of urban breezes and natural ventilation corridors, such as the Seine River basin, should also be quantified, potentially using the volume wind algorithm retrieval (Thobois et al., 2015).

To quantify the relevance of various atmospheric transport mechanisms, a methodology focused on the three-dimensional variability of the ABL is required, with similar attention to its temporal evolution. Key quantitative indicators include atmospheric stability, mixing, entrainment, ABL height, and horizontal advection. These indicators must account for responses to a combination of surface-induced processes—such as the heterogeneity of built-up areas, urban green spaces, suburban land use, and rural surroundings—and synoptic-scale meteorological conditions (e.g., the low-level jet). The dataset and data analysis methods developed in the framework of this thesis provide a solid basis for this potential future investigation.

- **The LLJ implications for fog dynamics:** one of the key research topics at the SIRTA observatory is fog dynamics. The SIRTA research team has conducted numerous studies to better understand the physical processes governing the formation, evolution, and dissipation of continental fog events. Improving the understanding of these processes is critical, as fog significantly impacts visibility, leading to human and economic losses due to increased delays and accident risks in both air and land transportation. Radiation fog forms under clear-sky conditions by radiative cooling of the surface, leading to a surface-based temperature inversion and cooling of a shallow layer of air near the ground. When supersaturation conditions are reached, aerosols activate into fog droplets. The fog layers remain shallow while stable atmospheric conditions persist. Occasionally, the radiative fog can evolve into a deeper fog layer that becomes unstable. Temperature profiles and liquid water profiles become adiabatic in the deeper fog layer. Based on over 12 years of fog observations at the SIRTA observatory, this transition from stable to adiabatic fog has been successfully linked to an abrupt increase in turbulence. However, the source of this turbulence remains unclear.

  The LLJ forms under stable atmospheric conditions and acts as a source of mechanical turbulence. Since fog and the LLJ share similar physical processes in their genesis, future fog research must consider the potential role of the LLJ in transforming stable radiation fog into adiabatic fog. As discussed in this thesis (Section 1.5), the DWL is unable to provide wind measurements in deep fog layers, posing a technical limitation for this quantitative assessment. However, the SIRTA observatory is equipped with several instruments that can be used to determine whether a relationship exists between these two boundary layer phenomena. For instance, the SIRTA observatory has UHF

wind profiling radar measurements enabling an assessment of whether both phenomena occur simultaneously, and, if so, whether the LLJ influences fog transition through mechanical turbulence. Nevertheless, DWL measurements can provide valuable data before the fog formation, particularly during the evening transition when surface-induced temperature inversions begin to develop, along with the formation of the LLJ. SIRTA has been collecting DWL WLS70 data for approximately 12 years, providing a rich dataset that is available for further analysis.

Appendices

Appendix A

The inertial oscillation

Blackadar, 1957 described the Inertial Oscillations (IO) in his pioneering theory as an undamped oscillation around the geostrophic wind vector near the elevated nocturnal temperature inversion height.

The IO is driven by the Coriolis force and the collapse of the convective boundary layer during the late evening, when the surface frictional forces are reduced through the atmospheric decoupling. The oscillation presents an amplitude equivalent to the ageostrophic wind (i.e. imbalance between the coriolis force and the pressure gradient) component with a period defined by:

$$T = 2\pi f^{-1}, \tag{A.1}$$

where f is the Coriolis parameter ($f = 2\Omega \sin\theta$, with Ω and θ being the angular speed of the Earth's rotation and latitude of the geographic location of interest, respectively). Blackadar's (1957) model is based on the homogeneous momentum ABL equations for the mean wind components u and v:

$$\frac{\partial u}{\partial t} = fv + \frac{\partial \tau_x/\rho}{\partial z} \tag{A.2}$$

and

$$\frac{\partial v}{\partial t} = f(G - u) + \frac{\partial \tau_y/\rho}{\partial z}, \tag{A.3}$$

where τ_x and τ_y represent the horizontal Reynolds stress divergence (friction) terms which are function of the air density ρ (kgm^{-3}). The x axis is aligned with the geostrophic wind, whose magnitude is written G. Given that any surface-driven turbulent mixing is suppressed, and the turbulent components can be neglected in the initial equations because they no longer affect motions at those heights over the course of the night. Hence, the Reynolds stresses become 0 and Eq. A.2 and Eq. A.3 become:

$$\frac{\partial u}{\partial t} = fv \tag{A.4}$$

and

$$\frac{\partial v}{\partial t} = f(G - u). \tag{A.5}$$

It is possible to find a solution to this system by differentiating Eq. A.4 and substituting Eq. A.5 into Eq. A.4. Assuming an initial wind profile at the onset of the IO, and to obtain equations expressed in terms of the geostrophic wind (i.e., u_0 and v_0, given $u = u_0$ and $v = v_0$ when $t = 0$) the solution is expressed as:

$$u - G = (v_0 - 0)\sin(T) + (u_0 - G)\cos(T) \tag{A.6}$$

and

$$v - 0 = (v_0 - 0)\cos(T) - (u_0 - G)\sin(T). \tag{A.7}$$

This solution assumes that over the course of the night the friction terms remain negligible and winds evolve with an *inertial period* T (Eq. A.1). Equations A.6 and A.7 show the undamped oscillations around the equilibrium (u_{eq} and v_{eq}, with eq being *equilibrium*) solution for equations A.4 ($u_{eq} = G$) and A.5 ($v_{eq} = 0$), so that the LLJ winds can be supergeostrophic and oscillate around G without collapsing. Near the top of the temperature inversion where the IO theory is valid, equations A.6 and A.7 present solutions that are height independent and equals to the intial magnitude of G at sunset.

Appendix B

Supplementary figures of Chapter 3

The following figures are supplementary material for Chapter 3, which presents the scientific article entitled "*The Paris Low-Level Jet During PANAME 2022 and its Impact on the Summertime Urban Heat Island*" (Céspedes et al., 2024).

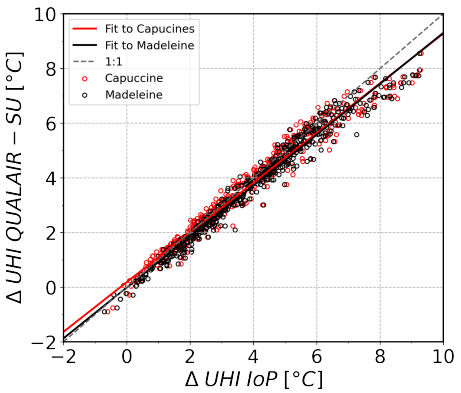

Figure B.1 : Comparison of ΔUHI = T_{urban} - T_{rural} calculated using a rooftop site at QUALAIR-SU (20 m agl) against ΔUHI determined for two street-level: Boulevard des Capucines and Place de la Madeleine. Solid lines represent the best linear fit for each group of data.

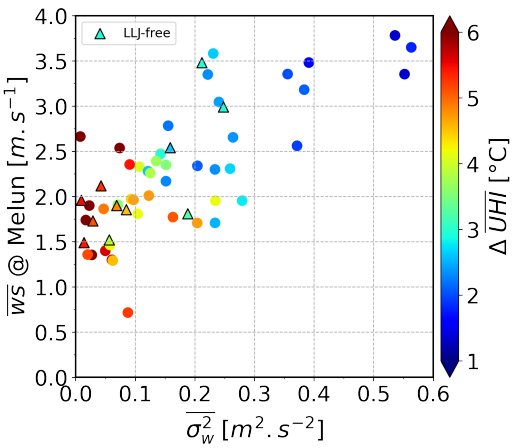

Figure B.2 : Nocturnal average of $10\,\mathrm{m\ agl}$ wind speed at Melun (rural site) as function of the nocturnal average vertical velocity variance (σ_w^2) at $238\,\mathrm{m\ agl}$ in the urban boundary layer, for all cloud-free nights in the study period. Data are colored by the the nocturnal average of ΔUHI. Dots represent nights with LLJ and the triangles the LLJ-free events.

List of abbreviations

LLJ Low-Level Jet

DWL Doppler Wind Lidar

ABL Atmospheric Boundary Layer

CBL Convective Boundary Layer

SBL Stable Boundary Layer

RL Residual Layer

EZ Entrainment Zone

CI Capping Inversion

FT Free Troposphere

UBL Urban Boundary Layer

UCL Urban Canopy Layer

ISL Inertial Sublayer

SL Surface Layer

ML Mixed Layer

UHI Urban Heat Island

IO Inertial Oscillation

NWP Numerical Weather Prediction

SODAR Sonic Detection and Ranging

RWP Radar Wind Profiling

LIDAR Light Detection and Ranging

FOV Field of View

LOS Line Of Sight

DOF Degrees of Freedom

PPI Plan-Position Indicator

RHI Range Height Indicator

VAD Velocity Azimuth Display

VVP Volume Velocity Processing

VW Volume Wind

DBS Doppler Beam Swinging

SIRTA Site Instrumental de Recherche par Télédétection Atmosphérique

PANAME PAris Region Urban Atmospheric Observations and Models for Multidisciplinary Research

ALC Automatic Lidars and Ceilometers

MWR Microwave Radiometer

Bibliography

Adegoke, J. O., R. Pielke, and A. M. Carleton (Feb. 2007). "Observational and modeling studies of the impacts of agriculture-related land use change on planetary boundary layer processes in the central U.S." In: Agricultural and Forest Meteorology 142 (2-4), pp. 203–215. DOI: 10.1016/J.AGRFORMET.2006.07.013 (cit. on p. 3).

Algarra, I., J. Eiras-Barca, R. Nieto, and L. Gimeno (Nov. 2019). "Global climatology of nocturnal low-level jets and associated moisture sources and sinks". In: Atmospheric Research 229, pp. 39–59. DOI: 10.1016/J.ATMOSRES.2019.06.016 (cit. on p. 43).

Andreas, E. L., K. J. Claffey, and A. P. Makshtas (Dec. 2000). "Low-Level Atmospheric Jets And Inversions Over The Western Weddell Sea". In: Boundary-Layer Meteorology 2000 97:3 97 (3), pp. 459–486. DOI: 10.1023/A:1002793831076 (cit. on p. 50).

Arfeuille, G., A. L. Quintanilla-Montoya, F. C. V. González, and L. Z. Villarreal (June 2015). "Observational Characteristics of Low-Level Jets in Central Western Mexico". In: Boundary-Layer Meteorology 155 (3), pp. 483–500. DOI: 10.1007/S10546-015-0005-0/METRICS (cit. on p. 43).

Baas, P., F. C. Bosveld, H. K. Baltink, and A. A. Holtslag (Aug. 2009). "A Climatology of Nocturnal Low-Level Jets at Cabauw". In: Journal of Applied Meteorology and Climatology 48 (8), pp. 1627–1642. DOI: 10.1175/2009JAMC1965.1 (cit. on pp. 11, 18, 37, 43, 45, 50, 55, 56, 74).

Banta, R. M., R. K. Newsom, J. K. Lundquist, Y. L. Pichugina, R. L. Coulter, and L. Mahrt (Nov. 2002). "Nocturnal Low-Level Jet Characteristics Over Kansas During Cases-99". In: Boundary-Layer Meteorology 2002 105:2 105 (2), pp. 221–252. DOI: 10.1023/A:1019992330866 (cit. on pp. 12, 18, 19, 43, 44, 50, 53, 65).

Banta, R. M., Y. L. Pichugina, and W. A. Brewer (Nov. 2006). "Turbulent Velocity-Variance Profiles in the Stable Boundary Layer Generated by a Nocturnal Low-Level Jet". In: Journal of the Atmospheric Sciences 63 (11), pp. 2700–2719. DOI: 10.1175/JAS3776.1 (cit. on pp. 6, 19, 39, 54, 58, 65, 82).

Banta, R. M., Y. L. Pichugina, and R. K. Newsom (2003). "Relationship between Low-Level Jet Properties and Turbulence Kinetic Energy in the Nocturnal Stable Boundary Layer". In: Journal of the Atmospheric Sciences 60 (20), pp. 2549 –2555. DOI: https://doi.org/10.1175/1520-0469(2003)060<2549:RBLJPA>2.0.CO;2 (cit. on pp. 12, 19, 44, 53).

Barlow, J. F., C. H. Halios, S. E. Lane, and C. R. Wood (Feb. 2014). "Observations of urban boundary layer structure during a strong urban heat island event". In: Environmental Fluid Mechanics 2014 15:2 15 (2), pp. 373–398. DOI: 10.1007/S10652-014-9335-6 (cit. on pp. 19, 69, 80, 81).

Barlow, J. F. (Dec. 2014). "Progress in observing and modelling the urban boundary layer". In: Urban Climate 10 (P2), pp. 216–240. DOI: 10.1016/J.UCLIM.2014.03.011 (cit. on pp. 4, 5, 8, 19, 44).

Bedoya-Velásquez, A. E., G. Titos, J. A. Bravo-Aranda, M. Haeffelin, O. Favez, J. E. Petit, J. A. Casquero-Vera, F. J. Olmo-Reyes, E. Montilla-Rosero, C. D. Hoyos, L. Alados-Arboledas, and J. L. Guerrero-Rascado (June 2019). "Long-term aerosol optical hygroscopicity study at the ACTRIS SIRTA observatory: Synergy between ceilometer and in situ measurements". In: Atmospheric Chemistry and Physics 19 (11), pp. 7883–7896. DOI: 10.5194/ACP-19-7883-2019 (cit. on p. 21).

Blackadar, A. K. (May 1957). "Boundary Layer Wind Maxima and Their Significance for the Growth of Nocturnal Inversions". In: Bulletin of the American Meteorological Society 38 (5), pp. 283–290. DOI: 10.1175/1520-0477-38.5.283 (cit. on pp. 11, 13, 18, 43, 58, 59, 91, 99).

Bonin, T. A., W. G. Blumberg, P. M. Klein, and P. B. Chilson (Dec. 2015). "Thermodynamic and Turbulence Characteristics of the Southern Great Plains Nocturnal Boundary Layer Under Differing Turbulent Regimes". In: Boundary-Layer Meteorology 157 (3), pp. 401–420. DOI: 10.1007/S10546-015-0072-2/METRICS (cit. on pp. 17, 43, 53, 58, 65).

Bonin, T. A., B. J. Carroll, R. M. Hardesty, W. A. Brewer, K. Hajny, O. E. Salmon, and P. B. Shepson (Mar. 2018). "Doppler Lidar Observations of the Mixing Height in Indianapolis Using an Automated Composite Fuzzy Logic Approach". In: Journal of Atmospheric and Oceanic Technology 35 (3), pp. 473–490. DOI: 10.1175/JTECH-D-17-0159.1 (cit. on p. 17).

Bonner, W. D. (1968). "Climatology of the Low Level Jet". In: Monthly Weather Review 96 (12), pp. 833 –850. DOI: https://doi.org/10.1175/1520-0493(1968)096<0833:COTLLJ>2.0.CO;2 (cit. on p. 50).

Bossioli, E., M. Tombrou, A. Dandou, E. Athanasopoulou, and K. V. Varotsos (Jan. 2009). "The role of planetary boundary-layer parameterizations in the air quality of an urban area with complex topography". In: Boundary-Layer Meteorology 131 (1), pp. 53–72. DOI: 10.1007/S10546-009-9349-7/METRICS (cit. on p. 3).

Bosveld, F. C., P. Baas, A. C. Beljaars, A. A. Holtslag, J. V. G. de Arellano, and B. J. van de Wiel (Dec. 2020). "Fifty Years of Atmospheric Boundary-Layer Research at Cabauw Serving Weather, Air Quality and Climate". In: Boundary-Layer Meteorology 177 (2-3), pp. 583–612. DOI: 10.1007/S10546-020-00541-W/FIGURES/11 (cit. on p. 3).

Brunsell, N. A., D. A. Rahn, and D. B. Mechem (Apr. 2021). "Impact of a Nocturnal Low-Level Jet on Surface-Layer Turbulent Characteristics". In: Journal of Geophysical Research: Atmospheres 126 (7), e2020JD034083. DOI: 10.1029/2020JD034083 (cit. on p. 12).

Builes-Jaramillo, A., J. Yepes, and H. D. Salas (Feb. 2022). "The Orinoco Low-Level Jet and Its Association with the Hydroclimatology of Northern South America". In: Journal of Hydrometeorology 23 (2), pp. 209–223. DOI: 10.1175/JHM-D-21-0073.1 (cit. on p. 18).

Cai, X., J. Yang, Y. Zhang, X. Xiao, and J. C. Xia (Oct. 2023). "Cooling island effect in urban parks from the perspective of internal park landscape". In: Humanities and Social Sciences Communications 2023 10:1 10 (1), pp. 1–12. DOI: 10.1057/s41599-023-02209-5 (cit. on p. 2).

Canouï-Poitrine, F., E. Cadot, A. Spira, I. Gremy, A. Lefranc, P. Pépin, H. Isnard, and L. Mandereau-Bruno (Apr. 2006). "Excess deaths during the August 2003 heat wave in Paris, France". In: Revue d'Épidémiologie et de Santé Publique 54 (2), pp. 127–135. DOI: 10.1016/S0398-7620(06)76706-2 (cit. on p. 1).

Cariou, J. P., M. Boquet, S. Lolli, R. Parmentier, and L. Sauvage (Oct. 2009). "Validation of the new long range 1.5µm wind lidar WLS70 for atmospheric dynamics studies". In: https://doi.org/10.1117/12.830292 7479, pp. 180–189. DOI: 10.1117/12.830292 (cit. on p. 49).

Carroll, B. J., B. B. Demoz, and R. Delgado (Aug. 2019). "An Overview of Low-Level Jet Winds and Corresponding Mixed Layer Depths During PECAN". In: Journal of Geophysical Research: Atmospheres 124 (16), pp. 9141–9160. DOI: 10.1029/2019JD030658 (cit. on pp. 43, 66).

Cheliotis, I., E. Dieudonné, H. Delbarre, A. Sokolov, E. Dmitriev, P. Augustin, M. Fourmentin, F. Ravetta, and J. Pelon (Nov. 2021). "Properties of Coherent Structures over Paris: A Study Based on an Automated Classification Method for Doppler Lidar Observations". In: Journal of Applied Meteorology and Climatology 60 (11), pp. 1545–1559. DOI: 10.1175/JAMC-D-21-0014.1 (cit. on pp. 19, 45, 55).

Chen, Y.-L., C.-C. Tu, F. Hsiao, C.-S. Chen, P.-L. Lin, and P.-H. Lin (Mar. 2022). "An Overview of Low-Level Jets (LLJs) and Their Roles in Heavy Rainfall over the Taiwan Area during the Early Summer Rainy Season". In: Meteorology 2022, Vol. 1, Pages 64-112 1 (1), pp. 64–112. DOI: 10.3390/METEOROLOGY1010006 (cit. on p. 43).

Cheng, V., E. Ng, C. Chan, and B. Givoni (Jan. 2012). "Outdoor thermal comfort study in a sub-tropical climate: A longitudinal study based in Hong Kong". In: International Journal of Biometeorology 56 (1), pp. 43–56. DOI: 10.1007/S00484-010-0396-Z/FIGURES/16 (cit. on pp. 11, 44).

Chiriaco, M., J. C. Dupont, S. Bastin, J. Badosa, J. Lopez, M. Haeffelin, H. Chepfer, and R. Guzman (May 2018). "ReOBS: A new approach to synthesize long-term multi-variable dataset and application to the SIRTA supersite". In: Earth System Science Data 10 (2), pp. 919–940. DOI: 10.5194/ESSD-10-919-2018 (cit. on pp. 25, 46).

Cimini, D., M. Haeffelin, S. Kotthaus, U. Löhnert, P. Martinet, E. O'Connor, C. Walden, M. C. Coen, and J. Preissler (Apr. 2020). "Towards the profiling of the atmospheric boundary layer at European scale—introducing the COST Action PROBE". In: Bulletin of Atmospheric Science and Technology 1 (1), pp. 23–42. DOI: 10.1007/S42865-020-00003-8/FIGURES/5 (cit. on pp. 3, 14).

Climate Change, U. U. N. F. C. on (2015). "The Paris Agreement". In: (cit. on p. 20).

Comerón, A., C. Muñoz-Porcar, A. Rodríguez-Gómez, M. Sicard, F. Dios, C. Gil-Díaz, D. C. F. dos Santos Oliveira, and F. Rocadenbosch (2023). "An explicit formulation for the retrieval of the overlap function in an elastic and Raman aerosol lidar". In: Atmospheric Measurement Techniques 16 (11), pp. 3015–3025. DOI: 10.5194/AMT-16-3015-2023 (cit. on p. 15).

Conangla, L. and J. Cuxart (Feb. 2006). "On the turbulence in the upper part of the low-level jet: An experimental and numerical study". In: Boundary-Layer Meteorology 118 (2), pp. 379–400. DOI: 10.1007/S10546-005-0608-Y/METRICS (cit. on p. 53).

Céspedes, J, S Kotthaus, J Preissler, C Toupoint, L Thobois, M.-A. Drouin, J.-C. Dupont, A Faucheux, and M Haeffelin (2024). "The Paris Low-Level Jet During PANAME 2022 and

its Impact on the Summertime Urban Heat Island". In: EGUsphere 2024, pp. 1–31. DOI: 10.5194/egusphere-2024-520 (cit. on pp. 41, 101).

Céspedes, J., S. Kotthaus, L. Thobois, and M. Haeffelin (June 2022). "Deriving 3D wind fields in the Paris urban atmosphere from scanning Doppler lidar observations". In: EMS2022. DOI: 10.5194/EMS2022-676 (cit. on p. 15).

Dabberdt, W. F., D. H. Lenschow, T. W. Horst, P. R. Zimmerman, S. P. Oncley, and A. C. Delany (June 1993). "Atmosphere-Surface Exchange Measurements". In: Science 260 (5113), pp. 1472–1481. DOI: 10.1126/SCIENCE.260.5113.1472 (cit. on p. 3).

Dieudonné, E., H. Delbarre, A. Sokolov, F. Ebojie, P. Augustin, and M. Fourmentin (July 2023). "Characteristics of the low-level jets observed over Dunkerque (North Sea French coast) using 4 years of wind lidar data". In: Quarterly Journal of the Royal Meteorological Society 149 (754), pp. 1745–1768. DOI: 10.1002/QJ.4480 (cit. on pp. 12, 45).

Dione, C., M. Haeffelin, F. Burnet, C. Lac, G. Canut, J. Delanoë, J. C. Dupont, S. Jorquera, P. Martinet, J. F. Ribaud, and F. Toledo (Dec. 2023). "Role of thermodynamic and turbulence processes on the fog life cycle during SOFOG3D experiment". In: Atmospheric Chemistry and Physics 23 (24), pp. 15711–15731. DOI: 10.5194/ACP-23-15711-2023 (cit. on pp. 21, 28).

Doick, K. J., A. Peace, and T. R. Hutchings (Sept. 2014). "The role of one large greenspace in mitigating London's nocturnal urban heat island". In: Science of The Total Environment 493, pp. 662–671. DOI: 10.1016/J.SCITOTENV.2014.06.048 (cit. on p. 2).

Dolfi-Bouteyre, A., B. Augère, C. Besson, G. Canat, D. Fleury, T. Gaudo, D. Goular, L. Lombard, C. Planchat, M. Valla, et al. (2008). "1.5 μm all fiber pulsed lidar for wake vortex monitoring". In: Conference on Lasers and Electro-Optics. Optica Publishing Group, CMQ3 (cit. on p. 48).

Drew, D. R., J. F. Barlow, and S. E. Lane (Oct. 2013). "Observations of wind speed profiles over Greater London, UK, using a Doppler lidar". In: Journal of Wind Engineering and Industrial Aerodynamics 121, pp. 98–105. DOI: 10.1016/J.JWEIA.2013.07.019 (cit. on p. 72).

Du, Y. and G. Chen (Dec. 2019). "Climatology of Low-Level Jets and Their Impact on Rainfall over Southern China during the Early-Summer Rainy Season". In: Journal of Climate 32 (24), pp. 8813–8833. DOI: 10.1175/JCLI-D-19-0306.1 (cit. on p. 43).

Duarte, H. F., M. Y. Leclerc, G. Zhang, D. Durden, R. Kurzeja, M. Parker, and D. Werth (Sept. 2015). "Impact of Nocturnal Low-Level Jets on Near-Surface Turbulence Kinetic Energy". In: Boundary-Layer Meteorology 156 (3), pp. 349–370. DOI: 10.1007/S10546-015-0030-Z/METRICS (cit. on pp. 12, 19, 37, 50, 55).

Dupont, E., L. Menut, B. Carissimo, J. Pelon, and P. Flamant (Mar. 1999). "Comparison between the atmospheric boundary layer in Paris and its rural suburbs during the ECLAP experiment". In: Atmospheric Environment 33 (6), pp. 979–994. DOI: 10.1016/S1352-2310(98)00216-7 (cit. on pp. 21, 69, 83).

Dupont, J. C., M. Haeffelin, J. Badosa, T. Elias, O. Favez, J. E. Petit, F. Meleux, J. Sciare, V. Crenn, and J. L. Bonne (Sept. 2016). "Role of the boundary layer dynamics effects on an extreme air pollution event in Paris". In: Atmospheric Environment 141, pp. 571–579. DOI: 10.1016/J.ATMOSENV.2016.06.061 (cit. on pp. 21, 28, 49).

Emeis, S. (2021). "Sodar and RASS". In: Springer Handbooks, pp. 663–684. DOI: 10.1007/978-3-030-52171-4_23/FIGURES/10 (cit. on p. 14).

ESA (2023). Copernicus DEM - Global and European Digital Elevation Model (COP-DEM). DOI: https://doi.org/10.5270/ESA-c5d3d65 (cit. on pp. 24, 47).

Fenner, D., A. Christen, S. Grimmond, F. Meier, W. Morrison, M. Zeeman, J. Barlow, J. Birkmann, L. Blunn, N. Chrysoulakis, M. Clements, R. Glazer, D. Hertwig, S. Kotthaus, K. König, D. Looschelders, Z. Mitraka, D. Poursanidis, D. Tsirantonakis, B. Bechtel, K. Benjamin, F. Beyrich, F. Briegel, G. Feigel, C. Gertsen, N. Iqbal, J. Kittner, H. Lean, Y. Liu, Z. Luo, M. McGrory, S. Metzger, M. Paskin, M. Ravan, T. Ruhtz, B. Saunders, D. Scherer, S. T. Smith, M. Stretton, K. Trachte, and M. V. Hove (July 2024). "urbisphere-Berlin campaign: Investigating multi-scale urban impacts on the atmospheric boundary layer". In: Bulletin of the American Meteorological Society -1 (aop). DOI: 10.1175/BAMS-D-23-0030.1 (cit. on p. 19).

Filioglou, M., J. Preissler, A. Troiville, L. Thobois, V. Vakkari, M. Auvinen, C. Fortelius, E. Gregow, K. Hämäläinen, A. Hellsten, L. Järvi, E. O'Connor, D. Schönach, and A. Hirsikko (Mar. 2022). "Evaluating modelled winds over an urban area using ground-based Doppler lidar observations". In: Meteorological Applications 29 (2), e2052. DOI: 10.1002/MET.2052 (cit. on pp. 17, 19, 70).

Foken, T. and J. Bange (2021). "Wind Sensors". In: Springer Handbooks, pp. 243–272. DOI: 10.1007/978-3-030-52171-4_9/FIGURES/24 (cit. on p. 13).

Foret, G., V. Michoud, S. Kotthaus, J. E. Petit, A. Baudic, G. Siour, Y. Kim, J. F. Doussin, J. C. Dupont, P. Formenti, C. Gaimoz, V. Ghersi, A. Gratien, V. Gros, J. L. Jaffrezo, M. Haeffelin, M. Kreitz, F. Ravetta, K. Sartelet, L. Simon, Y. Té, G. Uzu, S. Zhang, O. Favez, and M. Beekmann (Dec. 2022). "The December 2016 extreme weather and particulate matter pollution episode in the Paris region (France)". In: Atmospheric Environment 291, p. 119386. DOI: 10.1016/J.ATMOSENV.2022.119386 (cit. on pp. 21, 28).

Garratt, J. R. (Oct. 1994). "Review: the atmospheric boundary layer". In: Earth-Science Reviews 37 (1-2), pp. 89–134. DOI: 10.1016/0012-8252(94)90026-4 (cit. on p. 3).

Goger, B., I. Stiperski, L. Nicholson, and T. Sauter (Apr. 2022). "Large-eddy simulations of the atmospheric boundary layer over an Alpine glacier: Impact of synoptic flow direction and governing processes". In: Quarterly Journal of the Royal Meteorological Society 148 (744), pp. 1319–1343. DOI: 10.1002/QJ.4263 (cit. on p. 6).

Grimmond, C. S. B. and T. R. Oke (2002). "Turbulent Heat Fluxes in Urban Areas: Observations and a Local-Scale Urban Meteorological Parameterization Scheme (LUMPS)". In: Journal of Applied Meteorology 41.7, pp. 792 –810. DOI: 10.1175/1520-0450(2002)041<0792:THFIUA>2.0.CO;2 (cit. on p. 2).

Gultepe, I., R. Sharman, P. D. Williams, B. Zhou, G. Ellrod, P. Minnis, S. Trier, S. Griffin, S. S. Yum, B. Gharabaghi, W. Feltz, M. Temimi, Z. Pu, L. N. Storer, P. Kneringer, M. J. Weston, H. ya Chuang, L. Thobois, A. P. Dimri, S. J. Dietz, G. B. França, M. V. Almeida, and F. L. Neto (May 2019). "A Review of High Impact Weather for Aviation Meteorology". In: Pure and Applied Geophysics 176 (5), pp. 1869–1921. DOI: 10.1007/S00024-019-02168-6/METRICS (cit. on pp. 3, 43).

Haeffelin, M., L. Barthès, O. Bock, C. Boitel, S. Bony, D. Bouniol, H. Chepfer, M. Chiriaco, J. Cuesta, J. Delanoë, P. Drobinski, J. L. Dufresne, C. Flamant, M. Grall, A. Hodzic, F.

Hourdin, F. Lapouge, Y. Lemaître, A. Mathieu, Y. Morille, C. Naud, V. Noël, W. O'Hirok, J. Pelon, C. Pietras, A. Protat, B. Romand, G. Scialom, and R. Vautard (Feb. 2005). "SIRTA, a ground-based atmospheric observatory for cloud and aerosol research". In: Annales Geophysicae 23 (2), pp. 253–275. DOI: 10.5194/ANGEO-23-253-2005 (cit. on pp. 21, 25, 28, 46, 49).

Haeffelin, M, J.-F. Ribaud, J Céspedes, J.-C. Dupont, A Lemonsu, V Masson, T Nagel, and S Kotthaus (2024). "Impact of boundary layer stability on urban park cooling effect intensity". In: EGUsphere 2024, pp. 1–47. DOI: 10.5194/egusphere-2024-1777 (cit. on pp. 2, 19, 91).

Hartman, A. T. (May 2018). "An analysis of the effects of temperatures and circulations on the strength of the low-level jet in the Turkana Channel in East Africa". In: Theoretical and Applied Climatology 132 (3-4), pp. 1003–1017. DOI: 10.1007/S00704-017-2121-X/METRICS (cit. on p. 43).

He, Y., C. Yuan, C. Ren, W. Wang, Y. Shi, and E. Ng (May 2022). "Urban ventilation assessment with improved vertical wind profile in high-density cities – Investigations in nighttime extreme heat". In: Building and Environment 216, p. 109018. DOI: 10.1016/J.BUILDENV.2022.109018 (cit. on pp. 10, 11, 43, 44).

Hogan, R. J., A. L. Grant, A. J. Illingworth, G. N. Pearson, and E. J. O'Connor (Apr. 2009). "Vertical velocity variance and skewness in clear and cloud-topped boundary layers as revealed by Doppler lidar". In: Quarterly Journal of the Royal Meteorological Society 135 (640), pp. 635–643. DOI: 10.1002/QJ.413 (cit. on pp. 5, 6, 17).

Holton, J. R. (Jan. 1967). "The diurnal boundary layer wind oscillation above sloping terrain". In: http://dx.doi.org/10.3402/tellusa.v19i2.9766 19 (2), pp. 200–205. DOI: 10.3402/TELLUSA.V19I2.9766 (cit. on pp. 12, 43).

Holtslag, A. A., G. Svensson, P. Baas, S. Basu, B. Beare, A. C. Beljaars, F. C. Bosveld, J. Cuxart, J. Lindvall, G. J. Steeneveld, M. Tjernström, and B. J. V. D. Wiel (Nov. 2013). "Stable Atmospheric Boundary Layers and Diurnal Cycles: Challenges for Weather and Climate Models". In: Bulletin of the American Meteorological Society 94 (11), pp. 1691–1706. DOI: 10.1175/BAMS-D-11-00187.1 (cit. on pp. 3, 8, 19).

Hu, X. M., P. M. Klein, M. Xue, J. K. Lundquist, F. Zhang, and Y. Qi (Aug. 2013). "Impact of Low-Level Jets on the Nocturnal Urban Heat Island Intensity in Oklahoma City". In: Journal of Applied Meteorology and Climatology 52 (8), pp. 1779–1802. DOI: 10.1175/JAMC-D-12-0256.1 (cit. on pp. 12, 19, 43, 44, 66).

Illingworth, A. J., D. Cimini, A. Haefele, M. Haeffelin, M. Hervo, S. Kotthaus, U. Löhnert, P. Martinet, I. Mattis, E. J. O'Connor, and R. Potthast (2019). "How Can Existing Ground-Based Profiling Instruments Improve European Weather Forecasts?" In: Bulletin of the American Meteorological Society 100.4, pp. 605 –619. DOI: 10.1175/BAMS-D-17-0231.1 (cit. on p. 14).

Jiménez-Sánchez, G., P. M. Markowski, V. Jewtoukoff, G. S. Young, and D. J. Stensrud (Oct. 2019). "The Orinoco Low-Level Jet: An Investigation of Its Characteristics and Evolution Using the WRF Model". In: Journal of Geophysical Research: Atmospheres 124 (20), pp. 10696–10711. DOI: 10.1029/2019JD030934 (cit. on p. 43).

Johansson, B. and D. Chen (Oct. 2003). "The influence of wind and topography on precipitation distribution in Sweden: statistical analysis and modelling". In:

International Journal of Climatology 23 (12), pp. 1523–1535. DOI: 10.1002/JOC.951 (cit. on p. 13).

Kalapureddy, M. C., D. N. Rao, A. R. Jain, and Y. Ohno (Nov. 2007). "Wind profiler observations of a monsoon low-level jet over a tropical Indian station". In: Annales Geophysicae 25 (10), pp. 2125–2137. DOI: 10.5194/ANGEO-25-2125-2007 (cit. on p. 14).

Kallistratova, M. A. and R. D. Kouznetsov (Apr. 2012). "Low-Level Jets in the Moscow Region in Summer and Winter Observed with a Sodar Network". In: Boundary-Layer Meteorology 143 (1), pp. 159–175. DOI: 10.1007/S10546-011-9639-8/METRICS (cit. on pp. 12, 43, 44).

Kallistratova, M. A., R. D. Kouznetsov, V. F. Kramar, and D. D. Kuznetsov (Sept. 2013). "Profiles of Wind Speed Variances within Nocturnal Low-Level Jets Observed with a Sodar". In: Journal of Atmospheric and Oceanic Technology 30 (9), pp. 1970–1977. DOI: 10.1175/JTECH-D-12-00265.1 (cit. on pp. 12, 43, 44).

Karipot, A., M. Y. Leclerc, and G. Zhang (Aug. 2009). "Characteristics of Nocturnal Low-Level Jets Observed in the North Florida Area". In: Monthly Weather Review 137 (8), pp. 2605–2621. DOI: 10.1175/2009MWR2705.1 (cit. on pp. 18, 37, 43, 45, 50, 55, 56, 65).

Karipot, A., M. Y. Leclerc, G. Zhang, K. F. Lewin, J. Nagy, G. R. Hendrey, G. Starr, C. Karipot, M. Y. Leclerc, G Zhang, K. F. Lewin, J Nagy, G. R. Hendrey, and G Starr (May 2008). "Influence of nocturnal low-level jet on turbulence structure and CO2 flux measurements over a forest canopy". In: Journal of Geophysical Research: Atmospheres 113 (D10), p. 10102. DOI: 10.1029/2007JD009149 (cit. on p. 12).

Kent, C. W., S. Grimmond, J. Barlow, D. Gatey, S. Kotthaus, F. Lindberg, and C. H. Halios (Aug. 2017). "Evaluation of Urban Local-Scale Aerodynamic Parameters: Implications for the Vertical Profile of Wind Speed and for Source Areas". In: Boundary-Layer Meteorology 164 (2), pp. 183–213. DOI: 10.1007/S10546-017-0248-Z/TABLES/5 (cit. on pp. 5, 19).

Klein, A., F. Ravetta, J. L. Thomas, G. Ancellet, P. Augustin, R. Wilson, E. Dieudonné, M. Fourmentin, H. Delbarre, and J. Pelon (Jan. 2019). "Influence of vertical mixing and nighttime transport on surface ozone variability in the morning in Paris and the surrounding region". In: Atmospheric Environment 197, pp. 92–102. DOI: 10.1016/J.ATMOSENV.2018.10.009 (cit. on pp. 43, 45, 55, 56).

Kong, F., W. Yan, G. Zheng, H. Yin, G. Cavan, W. Zhan, N. Zhang, and L. Cheng (Feb. 2016). "Retrieval of three-dimensional tree canopy and shade using terrestrial laser scanning (TLS) data to analyze the cooling effect of vegetation". In: Agricultural and Forest Meteorology 217, pp. 22–34. DOI: 10.1016/J.AGRFORMET.2015.11.005 (cit. on pp. 10, 44).

Kotroni, V. and K. Lagouvardos (July 1993). "Low-level jet streams associated with atmospheric cold fronts: Seven case studies from the Fronts 87 Experiment". In: Geophysical Research Letters 20 (13), pp. 1371–1374. DOI: 10.1029/93GL01701 (cit. on p. 12).

Kotthaus, S., J. A. Bravo-Aranda, M. C. Coen, J. L. Guerrero-Rascado, M. J. Costa, D. Cimini, E. J. O'Connor, M. Hervo, L. Alados-Arboledas, M. Jiménez-Portaz, L. Mona, D. Ruffieux, A. Illingworth, and M. Haeffelin (Jan. 2023). "Atmospheric boundary layer

height from ground-based remote sensing: a review of capabilities and limitations". In: Atmospheric Measurement Techniques 16 (2), pp. 433–479. DOI: 10.5194/AMT-16-433-2023 (cit. on pp. 6, 7, 14, 21, 60).

Kotthaus, S. and C. S. Grimmond (Dec. 2014). "Energy exchange in a dense urban environment – Part I: Temporal variability of long-term observations in central London". In: Urban Climate 10 (P2), pp. 261–280. DOI: 10.1016/J.UCLIM.2013.10.002 (cit. on pp. 3–5).

Kotthaus, S. and C. S. B. Grimmond (July 2018). "Atmospheric boundary-layer characteristics from ceilometer measurements. Part 1: A new method to track mixed layer height and classify clouds". In: Quarterly Journal of the Royal Meteorological Society 144 (714), pp. 1525–1538. DOI: 10.1002/QJ.3299 (cit. on p. 52).

Kotthaus, S., M. Haeffelin, J. Céspedes, J.-F. Ribaud, J.-C. Dupont, M.-A. Drouin, P. Martinet, and A. Lemonsu (Mar. 2024). "Linking synoptic flow and city dynamics: PANAME observations of the Paris urban boundary layer". In: EGU24. DOI: 10.5194/EGUSPHERE-EGU24-18040 (cit. on p. 91).

Lane, S. E., J. F. Barlow, and C. R. Wood (Aug. 2013). "An assessment of a three-beam Doppler lidar wind profiling method for use in urban areas". In: Journal of Wind Engineering and Industrial Aerodynamics 119, pp. 53–59. DOI: 10.1016/J.JWEIA.2013.05.010 (cit. on p. 17).

Lehmann, V. and G. Teschke (May 2008). "Advanced intermittent clutter filtering for radar wind profiler: signal separation through a Gabor frame expansion and its statistics". In: Annales Geophysicae 26 (4), pp. 759–783. DOI: 10.5194/ANGEO-26-759-2008 (cit. on p. 14).

Lemonsu, A., J. Alessandrini, J. Capo, M. Claeys, E. Cordeau, C. de Munck, S. Dahech, J. Dupont, F. Dugay, V. Dupuis, G. Forceville, S. Garrigou, O. Garrouste, M. Goret, S. Goria, M. Haeffelin, S. Host, C. Joly, P. Keravec, S. Kotthaus, N. Laruelle, M. Madelin, V. Masson, C. Mauclair, T. Nagel, M. Pascal, J. Ribaud, G. Roberts, A. Rosso, A. Roy, M. Sabre, O. Sanchez, M. Stempfelet, W. Wei, R. Wilson, and J. Wurtz (Apr. 2024a). "The heat and health in cities (H2C) project to support the prevention of extreme heat in cities". In: Climate Services 34, p. 100472. DOI: 10.1016/J.CLISER.2024.100472 (cit. on pp. 1, 3, 19, 21).

Lemonsu, A., S. Barrau, J. Capo, J. Céspedes, S. Dahech, C. de Munck, G. Dumas, J.-C. Dupont, V. Dupuis, J.-C. Etienne, O. Garrouste, M. Goret, M. Haeffelin, P. Keravec, S. Kotthaus, M. Madelin, P. Martinet, V. Masson, T. Nagel, J. Price, J.-F. Ribaud, M. Rivollet, G. Roberts, A. Roy, V. Unger, R. Wilson, S. Wallois, and J. Wurtz (2024b). "Multi-scale study of urban-atmosphere interactions in the Paris region (France) in the framework of the PANAME experiment". In: Submitted to Bulletin of the American Meteorological Society (cit. on pp. 20, 26).

Lemonsu, A., S. Belair, and J. Mailhot (Oct. 2009). "The new canadian urban modelling system: Evaluation for two cases from the joint urban 2003 Oklahoma City experiment". In: Boundary-Layer Meteorology 133 (1), pp. 47–70. DOI: 10.1007/S10546-009-9414-2/METRICS (cit. on pp. 70, 80).

Lemonsu, A. and V. Masson (Sept. 2002). "Simulation of a Summer Urban Breeze Over Paris". In: Boundary-Layer Meteorology 2002 104:3 104 (3), pp. 463–490. DOI: 10.1023/A:1016509614936 (cit. on pp. 10, 19, 44, 46, 69).

Li, D. and E. Bou-Zeid (Sept. 2013). "Synergistic Interactions between Urban Heat Islands and Heat Waves: The Impact in Cities Is Larger than the Sum of Its Parts". In: Journal of Applied Meteorology and Climatology 52 (9), pp. 2051–2064. DOI: 10.1175/JAMC-D-13-02.1 (cit. on p. 2).

Li, X. and Y. Du (Nov. 2021). "Statistical Relationships between Two Types of Heavy Rainfall and Low-Level Jets in South China". In: Journal of Climate 34 (21), pp. 8549–8566. DOI: 10.1175/JCLI-D-21-0121.1 (cit. on p. 43).

Li, X., C. Zhang, W. Li, R. O. Anyah, and J. Tian (June 2019). "Exploring the trend, prediction and driving forces of aerosols using satellite and ground data, and implications for climate change mitigation". In: Journal of Cleaner Production 223, pp. 238–251. DOI: 10.1016/J.JCLEPRO.2019.03.121 (cit. on pp. 10, 44).

Li, Z., J. Guo, A. Ding, H. Liao, J. Liu, Y. Sun, T. Wang, H. Xue, H. Zhang, and B. Zhu (Nov. 2017). "Aerosol and boundary-layer interactions and impact on air quality". In: National Science Review 4 (6), pp. 810–833. DOI: 10.1093/NSR/NWX117 (cit. on p. 3).

Lin, Y., C. Wang, J. Yan, J. Li, and S. He (Aug. 2022). "Observation and Simulation of Low-Level Jet Impacts on 3D Urban Heat Islands in Beijing: A Case Study". In: Journal of the Atmospheric Sciences 79 (8), pp. 2059–2073. DOI: 10.1175/JAS-D-21-0245.1 (cit. on pp. 2, 10, 12, 19, 43, 44, 66).

Liu, H., M. He, B. Wang, and Q. Zhang (Apr. 2014). "Advances in low-level jet research and future prospects". In: Journal of Meteorological Research 28 (1), pp. 57–75. DOI: 10.1007/S13351-014-3166-8/METRICS (cit. on p. 43).

Liu, Z., J. F. Barlow, P. W. Chan, J. C. H. Fung, Y. Li, C. Ren, H. W. L. Mak, and E. Ng (Oct. 2019). "A Review of Progress and Applications of Pulsed Doppler Wind LiDARs". In: Remote Sensing 2019, Vol. 11, Page 2522 11 (21), p. 2522. DOI: 10.3390/RS11212522 (cit. on pp. 16, 48, 72).

Luiz, E. W. and S. Fiedler (July 2022). "Spatiotemporal observations of nocturnal low-level jets and impacts on wind power production". In: Wind Energy Science 7 (4), pp. 1575–1591. DOI: 10.5194/WES-7-1575-2022 (cit. on p. 43).

Lundquist, J. K. (2021). "Wind Shear and Wind Veer Effects on Wind Turbines". In: Handbook of Wind Energy Aerodynamics, pp. 1–22. DOI: 10.1007/978-3-030-05455-7_44-1 (cit. on p. 43).

Marke, T., S. Crewell, V. Schemann, J. H. Schween, and M. Tuononen (May 2018). "Long-Term Observations and High-Resolution Modeling of Midlatitude Nocturnal Boundary Layer Processes Connected to Low-Level Jets". In: Journal of Applied Meteorology and Climatology 57 (5), pp. 1155–1170. DOI: 10.1175/JAMC-D-17-0341.1 (cit. on p. 56).

Mauritsen, T. and G. Svensson (Feb. 2007). "Observations of Stably Stratified Shear-Driven Atmospheric Turbulence at Low and High Richardson Numbers". In: Journal of the Atmospheric Sciences 64 (2), pp. 645–655. DOI: 10.1175/JAS3856.1 (cit. on p. 8).

Menut, L., R. Vautard, C. Flamant, C. Abonnel, M. Beekmann, P. Chazette, P. H. Flamant, D. Gombert, D. Guédalia, D. Kley, M. P. Lefebvre, B. Lossec, D. Martin, G. Mégie, P. Perros, M. Sicard, and G. Toupance (Nov. 2000). "Measurements and modelling of atmospheric pollution over the Paris area: an overview of the ESQUIF Project". In:

Annales Geophysicae 18 (11), pp. 1467–1481. DOI: 10.1007/S00585-000-1467-Y (cit. on p. 8).

Michael H. Jain, K. W. H. and R. A. M. D. J. Stensrud (1990). "Operational Systems for Observing the Lower Atmosphere: Importance of Data Sampling and Archival Procedures". In: Journal of Atmospheric and Oceanic Technology 7, pp. 930–937. DOI: https://doi.org/10.1175/1520-0426(1990)007<0930:OSFOTL>2.0.CO;2 (cit. on p. 14).

Miralles, D. G., A. J. Teuling, C. C. V. Heerwaarden, and J. V. G. D. Arellano (Apr. 2014). "Mega-heatwave temperatures due to combined soil desiccation and atmospheric heat accumulation". In: Nature Geoscience 2014 7:5 7 (5), pp. 345–349. DOI: 10.1038/ngeo2141 (cit. on p. 3).

Monin, A. S. (Jan. 1970). "The Atmospheric Boundary Layer". In: Annual Review of Fluid Mechanics 2 (Volume 2, 1970), pp. 225–250. DOI: 10.1146/ANNUREV.FL.02.010170.001301 (cit. on p. 4).

Morris, C. J. G., I. Simmonds, and N. Plummer (2001). "Quantification of the Influences of Wind and Cloud on the Nocturnal Urban Heat Island of a Large City". In: Journal of Applied Meteorology 40.2, pp. 169 –182. DOI: 10.1175/1520-0450(2001)040<0169:QOTIOW>2.0.CO;2 (cit. on p. 2).

Morrison, W., D. Looschelders, B Claxton, M.-A. Drouin, J. Céspedes, J.-C. Dupont, A Faucheux, C Holst, M Haeffelin, S Kotthaus, V. Masson, J McGregor, J Price, M Zeeman, A Christen, and S Grimmond (In preparation). "Harmonised boundary layer wind profile dataset from six ground-based doppler wind lidars across Paris, France." In: To be submitted to Earth System Science Data (cit. on p. 26).

Newman, J. F., P. M. Klein, S. Wharton, A. Sathe, T. A. Bonin, P. B. Chilson, and A. Muschinski (May 2016). "Evaluation of three lidar scanning strategies for turbulence measurements". In: Atmospheric Measurement Techniques 9 (5), pp. 1993–2013. DOI: 10.5194/AMT-9-1993-2016 (cit. on p. 17).

Ng, C. W. and K. K. Hon (Apr. 2022). "Fast dual-doppler LiDAR retrieval of boundary layer wind profiles". In: Weather 77 (4), pp. 134–142. DOI: 10.1002/WEA.3800 (cit. on p. 17).

Ng, E. (July 2009). "Policies and technical guidelines for urban planning of high-density cities – air ventilation assessment (AVA) of Hong Kong". In: Building and Environment 44 (7), pp. 1478–1488. DOI: 10.1016/J.BUILDENV.2008.06.013 (cit. on p. 19).

Noel, V., H. Chepfer, M. Haeffelin, and Y. Morille (Nov. 2006). "Classification of Ice Crystal Shapes in Midlatitude Ice Clouds from Three Years of Lidar Observations over the SIRTA Observatory". In: Journal of the Atmospheric Sciences 63 (11), pp. 2978–2991. DOI: 10.1175/JAS3767.1 (cit. on p. 21).

Ohya, Y., R. Nakamura, and T. Uchida (Mar. 2008). "Intermittent bursting of turbulence in a stable boundary layer with low-level jet". In: Boundary-Layer Meteorology 126 (3), pp. 349–363. DOI: 10.1007/S10546-007-9245-Y/METRICS (cit. on p. 12).

Oke, T. R. (Aug. 1973). "City size and the urban heat island". In: Atmospheric Environment (1967) 7 (8), pp. 769–779. DOI: 10.1016/0004-6981(73)90140-6 (cit. on pp. 11, 44, 64, 65).

Oke, T. R., G. Mills, A. Christen, and J. A. Voogt (2017a). "Urban Heat Island". In: Urban Climates. Cambridge University Press, 197–237. DOI: 10.1017/9781139016476.008 (cit. on pp. 10, 11, 42, 44, 64).

Oke, T. R., G. Mills, A. Christen, and J. A. Voogt (2017b). Urban climates. Cambridge University Press (cit. on pp. 2, 4, 8, 9, 19, 27).

Pal, S., I. Xueref-Remy, L. Ammoura, P. Chazette, F. Gibert, P. Royer, E. Dieudonné, J. C. Dupont, M. Haeffelin, C. Lac, M. Lopez, Y. Morille, and F. Ravetta (Dec. 2012). "Spatio-temporal variability of the atmospheric boundary layer depth over the Paris agglomeration: An assessment of the impact of the urban heat island intensity". In: Atmospheric Environment 63, pp. 261–275. DOI: 10.1016/J.ATMOSENV.2012.09.046 (cit. on pp. 25, 46).

Parish, T. R., R. D. Clark, and T. D. Sikora (Nov. 2020). "Nocturnal Destabilization Associated with the Summertime Great Plains Low-Level Jet". In: Monthly Weather Review 148 (11), pp. 4641–4656. DOI: 10.1175/MWR-D-19-0394.1 (cit. on p. 12).

Parish, T. R. and L. D. Oolman (Aug. 2010). "On the Role of Sloping Terrain in the Forcing of the Great Plains Low-Level Jet". In: Journal of the Atmospheric Sciences 67 (8), pp. 2690–2699. DOI: 10.1175/2010JAS3368.1 (cit. on p. 12).

Pearson, G., F. Davies, and C. Collier (Feb. 2009). "An Analysis of the Performance of the UFAM Pulsed Doppler Lidar for Observing the Boundary Layer". In: Journal of Atmospheric and Oceanic Technology 26 (2), pp. 240–250. DOI: 10.1175/2008JTECHA1128.1 (cit. on pp. 16, 17, 48, 72).

Petit, J.-E., V. Gros, O. Favez, L. Simon, C. Kalalian, E. Brugère, A. Borbon, J.-C. Dupont, G. Abbou, V. Ghersi, et al. (2023). "Forest fire plumes in the Paris region (France) during summer 2022, the spoor of a schorching summer". In: Copernicus Meetings (cit. on pp. 1, 2, 26, 46).

Peña, A., R. Floors, A. Sathe, S. E. Gryning, R. Wagner, M. S. Courtney, X. G. Larsén, A. N. Hahmann, and C. B. Hasager (Jan. 2016). "Ten Years of Boundary-Layer and Wind-Power Meteorology at Høvsøre, Denmark". In: Boundary-Layer Meteorology 158 (1), pp. 1–26. DOI: 10.1007/S10546-015-0079-8/FIGURES/9 (cit. on p. 3).

Pichugina, Y. L., R. M. Banta, W. A. Brewer, D. D. Turner, V. O. Wulfmeyer, E. J. Strobach, S. Baidar, and B. J. Carroll (Aug. 2023). "Doppler Lidar Measurements of Wind Variability and LLJ Properties in Central Oklahoma during the August 2017 Land–Atmosphere Feedback Experiment". In: Journal of Applied Meteorology and Climatology 62 (8), pp. 947–969. DOI: 10.1175/JAMC-D-22-0128.1 (cit. on p. 78).

Qi, L, L. M. Leslie, and S. X. Zhao (1999). "Cut-off low pressure systems over southern australia: climatology and case study". In: INTERNATIONAL JOURNAL OF CLIMATOLOGY Int. J. Climatol 19, pp. 1633–1649. DOI: 10.1002/(SICI)1097-0088(199912)19:15 (cit. on p. 43).

Qualair (2022). Site Qualair. Accessed: 2022-06-11. URL: http://qualair.aero.jussieu.fr/qualair.php?menu=present (cit. on p. 48).

Rahlves, C, F Beyrich, and S Raasch (2022). "Scan strategies for wind profiling with Doppler lidar – an large-eddy simulation (LES)-based evaluation". In: Atmospheric Measurement Techniques 15 (9), pp. 2839–2856. DOI: 10.5194/amt-15-2839-2022 (cit. on p. 71).

Rajewski, D. A., E. S. Takle, J. K. Lundquist, S. Oncley, J. H. Prueger, T. W. Horst, M. E. Rhodes, R. Pfeiffer, J. L. Hatfield, K. K. Spoth, and R. K. Doorenbos (May 2013). "Crop Wind Energy Experiment (CWEX): Observations of Surface-Layer, Boundary Layer, and Mesoscale Interactions with a Wind Farm". In: Bulletin of the American Meteorological Society 94 (5), pp. 655–672. DOI: 10.1175/BAMS-D-11-00240.1 (cit. on p. 3).

Region, L. P. (2023). "Ilots de chaleur Urbains (ICU) : classification des IMU en zone climatique locale (LCZ) , Aléas et Vulnérabilités à la chaleur de Jour et de Nuit en Île-de-France". In: (cit. on p. 47).

Reitebuch, O. and R. M. Hardesty (2021). "Doppler Wind Lidar". In: Springer Handbooks, pp. 759–797. DOI: 10.1007/978-3-030-52171-4_27/FIGURES/16 (cit. on p. 15).

Rennie, M. P., L. Isaksen, F. Weiler, J. de Kloe, T. Kanitz, and O. Reitebuch (Oct. 2021). "The impact of Aeolus wind retrievals on ECMWF global weather forecasts". In: Quarterly Journal of the Royal Meteorological Society 147 (740), pp. 3555–3586. DOI: 10.1002/QJ.4142 (cit. on p. 13).

Ridder, K. D., B. Maiheu, D. Lauwaet, I. A. Daglis, I. Keramitsoglou, K. Kourtidis, P. Manunta, and M. Paganini (Nov. 2016). "Urban Heat Island Intensification during Hot Spells—The Case of Paris during the Summer of 2003". In: Urban Science 2017, Vol. 1, Page 3 1 (1), p. 3. DOI: 10.3390/URBANSCI1010003 (cit. on pp. 10, 44).

Robine, J. M., S. L. K. Cheung, S. L. Roy, H. V. Oyen, C. Griffiths, J. P. Michel, and F. R. Herrmann (Feb. 2008). "Death toll exceeded 70,000 in Europe during the summer of 2003". In: Comptes Rendus Biologies 331 (2), pp. 171–178. DOI: 10.1016/J.CRVI.2007.12.001 (cit. on pp. 10, 44).

Rojas-Rueda, D., E. Morales-Zamora, W. A. Alsufyani, C. H. Herbst, S. M. AlBalawi, R. Alsukait, and M. Alomran (Jan. 2021). "Environmental Risk Factors and Health: An Umbrella Review of Meta-Analyses". In: International Journal of Environmental Research and Public Health 2021, Vol. 18, Page 704 18 (2), p. 704. DOI: 10.3390/IJERPH18020704 (cit. on pp. 1, 3).

Roy, S., A. Sentchev, M. Fourmentin, and P. Augustin (Nov. 2022). "Machine Learning and Deterministic Methods for Detection Meteorological Phenomena from Ground Measurements: Application for Low-Level Jet and Sea-Breeze Identification in Northern France". In: Atmosphere 2022, Vol. 13, Page 1873 13 (11), p. 1873. DOI: 10.3390/ATMOS13111873 (cit. on p. 45).

Roy, S., A. Sentchev, F. G. Schmitt, P. Augustin, and M. Fourmentin (June 2021). "Impact of the Nocturnal Low-Level Jet and Orographic Waves on Turbulent Motions and Energy Fluxes in the Lower Atmospheric Boundary Layer". In: Boundary-Layer Meteorology 2021 180:3 180 (3), pp. 527–542. DOI: 10.1007/S10546-021-00629-X (cit. on pp. 43, 45, 55).

Rubio, H., M. Kühn, and J. Gottschall (Dec. 2022). "Evaluation of low-level jets in the southern Baltic Sea: a comparison between ship-based lidar observational data and numerical models". In: Wind Energy Science 7 (6), pp. 2433–2455. DOI: 10.5194/WES-7-2433-2022 (cit. on p. 43).

Sathe, A., J. Mann, J. Gottschall, and M. S. Courtney (July 2011). "Can Wind Lidars Measure Turbulence?" In: Journal of Atmospheric and Oceanic Technology 28 (7), pp. 853–868. DOI: 10.1175/JTECH-D-10-05004.1 (cit. on p. 14).

Shapiro, A. and E. Fedorovich (July 2010). "Analytical description of a nocturnal low-level jet". In: Quarterly Journal of the Royal Meteorological Society 136 (650), pp. 1255–1262. DOI: 10.1002/QJ.628 (cit. on p. 12).

Shapiro, A., E. Fedorovich, and S. Rahimi (Aug. 2016). "A Unified Theory for the Great Plains Nocturnal Low-Level Jet". In: Journal of the Atmospheric Sciences 73 (8), pp. 3037–3057. DOI: 10.1175/JAS-D-15-0307.1 (cit. on p. 43).

Shashua-Bar, L. and M. E. Hoffman (Apr. 2000). "Vegetation as a climatic component in the design of an urban street: An empirical model for predicting the cooling effect of urban green areas with trees". In: Energy and Buildings 31 (3), pp. 221–235. DOI: 10.1016/S0378-7788(99)00018-3 (cit. on p. 2).

Stewart, I. D. and T. R. Oke (Dec. 2012). "Local Climate Zones for Urban Temperature Studies". In: Bulletin of the American Meteorological Society 93 (12), pp. 1879–1900. DOI: 10.1175/BAMS-D-11-00019.1 (cit. on p. 27).

Stoffelen, A., A. Benedetti, R. Borde, A. Dabas, P. Flamant, M. Forsythe, M. Hardesty, L. Isaksen, E. Källén, H. Körnich, T. Lee, O. Reitebuch, M. Rennie, L. P. Riishøjgaard, H. Schyberg, A. G. Straume, and M. Vaughan (Nov. 2020). "Wind Profile Satellite Observation Requirements and Capabilities". In: Bulletin of the American Meteorological Society 101 (11), E2005–E2021. DOI: 10.1175/BAMS-D-18-0202.1 (cit. on p. 13).

Stull, R. B. (1988a). "Mean Boundary Layer Characteristics". In: An Introduction to Boundary Layer Meteorology, pp. 1–27. DOI: 10.1007/978-94-009-3027-8_1 (cit. on pp. 3, 4, 6, 18).

– (1988b). "Stable Boundary Layer". In: An Introduction to Boundary Layer Meteorology, pp. 499–543. DOI: 10.1007/978-94-009-3027-8_12 (cit. on pp. 5, 43, 50, 58).

Sánchez, M. P., A. Pereira de Oliveira, R. P. Varona, J. V. Tito, G. Codato, R. Y. Ynoue, F. N. D. Ribeiro, E. P. Marques Filho, and L. C. da Silveira (2022a). "Observational Investigation of the Low-Level Jets in the Metropolitan Region of São Paulo, Brazil". In: Earth and Space Science 9.9, e2021EA002190. DOI: https://doi.org/10.1029/2021EA002190. eprint: https://agupubs.onlinelibrary.wiley.com/doi/pdf/10.1029/2021EA002190 (cit. on pp. 12, 44, 50).

Sánchez, M. P., A. P. de Oliveira, R. P. Varona, J. V. Tito, G. Codato, F. N. D. Ribeiro, E. P. M. Filho, and L. C. da Silveira (Feb. 2020). "Rawinsonde-Based Analysis of the Urban Boundary Layer in the Metropolitan Region of São Paulo, Brazil". In: Earth and Space Science 7 (2), e2019EA000781. DOI: 10.1029/2019EA000781 (cit. on p. 50).

Sánchez, M. P., A. P. de Oliveira, R. P. Varona, J. V. Tito, G. Codato, R. Y. Ynoue, F. N. D. Ribeiro, E. P. M. Filho, and L. C. da Silveira (Sept. 2022b). "Observational Investigation of the Low-Level Jets in the Metropolitan Region of São Paulo, Brazil". In: Earth and Space Science 9 (9). DOI: 10.1029/2021EA002190 (cit. on pp. 12, 18).

Taylor, J., P. Wilkinson, M. Davies, B. Armstrong, Z. Chalabi, A. Mavrogianni, P. Symonds, E. Oikonomou, and S. I. Bohnenstengel (Dec. 2015). "Mapping the effects of urban heat

island, housing, and age on excess heat-related mortality in London". In: Urban Climate 14, pp. 517–528. DOI: 10.1016/J.UCLIM.2015.08.001 (cit. on pp. 10, 44).

Teschke, G. and V. Lehmann (Sept. 2017). "Mean wind vector estimation using the velocity-Azimuth display (VAD) method: An explicit algebraic solution". In: Atmospheric Measurement Techniques 10 (9), pp. 3265–3271. DOI: 10.5194/AMT-10-3265-2017 (cit. on pp. 17, 71).

Theeuwes, N. E., J. F. Barlow, A. J. Teuling, C. S. B. Grimmond, and S. Kotthaus (May 2019). "Persistent cloud cover over mega-cities linked to surface heat release". In: npj Climate and Atmospheric Science 2019 2:1 2 (1), pp. 1–6. DOI: 10.1038/s41612-019-0072-x (cit. on pp. 6, 58).

Thobois, L., J. P. Cariou, and I. Gultepe (Dec. 2018). "Review of Lidar-Based Applications for Aviation Weather". In: Pure and Applied Geophysics 2018 176:5 176 (5), pp. 1959–1976. DOI: 10.1007/S00024-018-2058-8 (cit. on pp. 15, 16).

– (May 2019). "Review of Lidar-Based Applications for Aviation Weather". In: Pure and Applied Geophysics 176 (5), pp. 1959–1976. DOI: 10.1007/S00024-018-2058-8/FIGURES/12 (cit. on pp. 48, 72).

Thobois, L. P., R. Krishnamurty, J. P. Cariou, A. Dolfi-Bouteyre, and M. Valla (2015). "Wind and EDR measurements with scanning doppler LIDARS for preparing future weather dependent separation concepts". In: 7th AIAA Atmospheric and Space Environments Conference, 2015. DOI: 10.2514/6.2015-3317 (cit. on pp. 17, 31, 36, 89, 95).

Toledo, F, M Haeffelin, E Wærsted, and J.-C. Dupont (2021). "A new conceptual model for adiabatic fog". In: Atmospheric Chemistry and Physics 21 (17), pp. 13099–13117. DOI: 10.5194/acp-21-13099-2021 (cit. on p. 21).

Toupoint, C., J. Cespedes, S. Kotthaus, J. Preissler, L. Thobois, and M. Haeffelin (July 2024). "Mapping horizontal wind speed using a single Doppler Wind Lidar scanning horizontally: a test case over Paris". In: EMS2024. DOI: 10.5194/EMS2024-419 (cit. on pp. 31, 89).

Troude, F., E. Dupont, B. Carissimo, and A. I. Flossmann (June 2002). "Relative influence of urban and orographic effects for low wind conditions in the Paris area". In: Boundary-Layer Meteorology 103 (3), pp. 493–505. DOI: 10.1023/A:1014903627803/METRICS (cit. on p. 69).

Tsiringakis, A., N. E. Theeuwes, J. F. Barlow, and G. J. Steeneveld (May 2022). "Interactions Between the Nocturnal Low-Level Jets and the Urban Boundary Layer: A Case Study over London". In: Boundary-Layer Meteorology 183 (2), pp. 249–272. DOI: 10.1007/S10546-021-00681-7/FIGURES/9 (cit. on pp. 19, 44, 55, 69, 70, 75, 80, 81).

Tucker, S. C., W. A. Brewer, R. M. Banta, C. J. Senff, S. P. Sandberg, D. C. Law, A. M. Weickmann, and R. M. Hardesty (Apr. 2009). "Doppler Lidar Estimation of Mixing Height Using Turbulence, Shear, and Aerosol Profiles". In: Journal of Atmospheric and Oceanic Technology 26 (4), pp. 673–688. DOI: 10.1175/2008JTECHA1157.1 (cit. on p. 6).

Tuononen, M., V. A. Sinclair, and T. Vihma (Oct. 2015). "A climatology of low-level jets in the mid-latitudes and polar regions of the Northern Hemisphere". In: Atmospheric Science Letters 16 (4), pp. 492–499. DOI: 10.1002/ASL.587 (cit. on pp. 18, 50).

Tuononen, M., E. J. O'Connor, V. A. Sinclair, and V. Vakkari (Sept. 2017). "Low-Level Jets over Utö, Finland, Based on Doppler Lidar Observations". In: Journal of Applied Meteorology and Climatology 56 (9), pp. 2577–2594. DOI: 10.1175/JAMC-D-16-0411.1 (cit. on pp. 12, 18, 37, 43, 50–52, 55, 56, 66, 71, 89).

Turner, D. D., J. E. M. Goldsmith, and R. A. Ferrare (Apr. 2016). "Development and Applications of the ARM Raman Lidar". In: Meteorological Monographs 57 (1), pp. 18.1–18.15. DOI: 10.1175/AMSMONOGRAPHS-D-15-0026.1 (cit. on p. 16).

Ulpiani, G. (Jan. 2021). "On the linkage between urban heat island and urban pollution island: Three-decade literature review towards a conceptual framework". In: Science of The Total Environment 751, p. 141727. DOI: 10.1016/J.SCITOTENV.2020.141727 (cit. on p. 43).

Vanderwende, B. J., J. K. Lundquist, M. E. Rhodes, E. S. Takle, and S. L. Irvin (June 2015). "Observing and Simulating the Summertime Low-Level Jet in Central Iowa". In: Monthly Weather Review 143 (6), pp. 2319–2336. DOI: 10.1175/MWR-D-14-00325.1 (cit. on p. 43).

Waldteufel, P and H Corbin (1979). "On the Analysis of Single-Doppler Radar Data". In: Journal of Applied Meteorology and Climatology 18 (4), pp. 532 –542. DOI: 10.1175/1520-0450(1979)018<0532:OTAOSD>2.0.CO;2 (cit. on p. 17).

Wang, Y., C. L. Klipp, D. M. Garvey, D. A. Ligon, C. C. Williamson, S. S. Chang, R. K. Newsom, and R. Calhoun (Dec. 2007). "Nocturnal Low-Level-Jet-Dominated Atmospheric Boundary Layer Observed by a Doppler Lidar over Oklahoma City during JU2003". In: Journal of Applied Meteorology and Climatology 46 (12), pp. 2098–2109. DOI: 10.1175/2006JAMC1283.1 (cit. on pp. 69, 80, 81).

Wei, W., B. G. Wu, X. X. Ye, H. X. Wang, and H. S. Zhang (Dec. 2013). "Characteristics and Mechanisms of Low-Level Jets in the Yangtze River Delta of China". In: Boundary-Layer Meteorology 149 (3), pp. 403–424. DOI: 10.1007/S10546-013-9852-8/FIGURES/13 (cit. on p. 43).

Wei, W., H. Zhang, X. Zhang, and H. Che (Jan. 2023). "Low-level jets and their implications on air pollution: A review". In: Frontiers in Environmental Science 10, p. 1082623. DOI: 10.3389/FENVS.2022.1082623/BIBTEX (cit. on pp. 19, 43).

Whiteman, C. D., X. Bian, and S. Zhong (1997). "Low-Level Jet Climatology from Enhanced Rawinsonde Observations at a Site in the Southern Great Plains". In: Journal of Applied Meteorology 36 (10), pp. 1363 –1376. DOI: https://doi.org/10.1175/1520-0450(1997)036<1363:LLJCFE>2.0.CO;2 (cit. on p. 50).

Wiegner, M. (2012). "Lidar for Aerosol Remote Sensing". In: pp. 449–464. DOI: 10.1007/978-3-642-30183-4_27 (cit. on pp. 14, 15).

Wiel, B. J. van de, A. F. Moene, G. J. Steeneveld, P. Baas, F. C. Bosveld, and A. A. Holtslag (Aug. 2010). "A Conceptual View on Inertial Oscillations and Nocturnal Low-Level Jets". In: Journal of the Atmospheric Sciences 67 (8), pp. 2679–2689. DOI: 10.1175/2010JAS3289.1 (cit. on pp. 12, 59).

WMO (2018). "The Rolling Review of Requirements process | World Meteorological Organization". In: Accessed: 2022-12-11 (cit. on p. 13).

Wouters, H., K. D. Ridder, M. Demuzere, D. Lauwaet, and N. P. V. Lipzig (2013). "The diurnal evolution of the urban heat island of Paris: A model-based case study during

Summer 2006". In: Atmospheric Chemistry and Physics 13 (17), pp. 8525–8541. DOI: 10.5194/ACP-13-8525-2013 (cit. on pp. 8, 45).

Wulfmeyer, V. and T. Janjić (Nov. 2005). "Twenty-Four-Hour Observations of the Marine Boundary Layer Using Shipborne NOAA High-Resolution Doppler Lidar". In: Journal of Applied Meteorology and Climatology 44 (11), pp. 1723–1744. DOI: 10.1175/JAM2296.1 (cit. on p. 17).

Wærsted, E. G., M. Haeffelin, J. C. Dupont, J. Delanoë, and P. Dubuisson (Sept. 2017). "Radiation in fog: Quantification of the impact on fog liquid water based on ground-based remote sensing". In: Atmospheric Chemistry and Physics 17 (17), pp. 10811–10835. DOI: 10.5194/ACP-17-10811-2017 (cit. on p. 21).

Yin, Z., Q. Chen, Y. Yi, Z. Bu, L. Wang, and X. Wang (Sept. 2023). "Low Blind Zone Atmospheric Lidar Based on Fiber Bundle Receiving". In: Remote Sensing 2023, Vol. 15, Page 4643 15 (19), p. 4643. DOI: 10.3390/RS15194643 (cit. on p. 15).

Zhang, Y., M. Xue, K. Zhu, and B. Zhou (Mar. 2019). "What Is the Main Cause of Diurnal Variation and Nocturnal Peak of Summer Precipitation in Sichuan Basin, China? The Key Role of Boundary Layer Low-Level Jet Inertial Oscillations". In: Journal of Geophysical Research: Atmospheres 124 (5), pp. 2643–2664. DOI: 10.1029/2018JD029834 (cit. on p. 18).

Zhu, W., J. Sun, C. Yang, M. Liu, X. Xu, and C. Ji (Aug. 2021). "How to Measure the Urban Park Cooling Island? A Perspective of Absolute and Relative Indicators Using Remote Sensing and Buffer Analysis". In: Remote Sensing 2021, Vol. 13, Page 3154 13 (16), p. 3154. DOI: 10.3390/RS13163154 (cit. on p. 2).

ECOLE DOCTORALE

Titre : Jet de basse couche nocturne en été dans la région parisienne : interactions avec la chaleur urbaine et les caractéristiques de surface

Mots clés : Couche limite atmosphérique, Jet de basse couche, Chaleur urbaine, Lidar Doppler à vent

Résumé : L'environnement urbain induit des modifications structurelles profondes dans la couche limite atmosphérique (ABL). Les surfaces urbaines, marquées par des émissions de chaleur, des matériaux imperméables et une rugosité accrue, retiennent efficacement la chaleur et modifient les flux d'air. Cela crée des microclimats distincts, comme l'îlot de chaleur urbain (UHI) nocturne, aggravant les risques thermiques pour les citadins. En plus de ces processus de surface, la météorologie synoptique influence les microclimats urbains et le transport de la pollution via son impact sur la dynamique de l'ABL. Cependant, la compréhension de ces interactions surface-atmosphère reste limitée en raison du manque d'observations détaillées.
Cette thèse étudie l'interaction entre les courants-jets nocturnes de basse altitude (LLJ) et l'atmosphère urbaine en région parisienne, à partir de deux ans d'observations Doppler Wind Lidar (DWL) en milieux urbain et périurbain. Un nouvel algorithme a été développé pour détecter les LLJ, et une stratégie innovante de balayage Doppler Beam Swinging (DBS) a été introduite pour améliorer leur suivi. Les résultats montrent que les LLJ sont fréquents en été et que leurs caractéristiques varient selon la direction du vent (e.g. forts LLJ majoritairement du nord-est). Ils se forment après le coucher du soleil et atteignent des altitudes maximales de 200 à 950 m.
Les LLJ influencent l'intensité de l'UHI via la génération de turbulence mécanique verticale. Lors d'épisodes de chaleur extrême, les températures nocturnes à Paris dépassaient de 9°C celles des zones rurales. Ces intensités élevées apparaissent lorsque le mélange sous les LLJ est faible, car la stratification thermique isole le jet de la couche de surface urbaine. Il a également été observé que la flottabilité urbaine et la topographie modulent les caractéristiques des LLJ (e.g. hauteur du cœur) uniquement en présence d'un mélange vertical suffisant. Ces résultats soulignent le rôle clé de la dynamique de l'ABL comme lien entre l'écoulement synoptique et la surface urbaine, et l'importance du mélange atmosphérique pour évaluer le risque thermique urbain et le transport de la pollution.

Title : Summertime nocturnal Low-Level Jet in the Paris region: interactions with the urban heat and surface characteristics

Keywords : Atmospheric Boundary Layer, Low-Level Jet, Urban Heat, Doppler Wind Lidar

Abstract : The urban environment is responsible for profound structural changes in the atmospheric boundary layer (ABL). Urban surfaces, characterized by heat emissions, impervious materials, and augmented roughness, retain heat efficiently and modify airflow. This creates distinct microclimate conditions, such as the nocturnal Urban Heat Island (UHI) phenomenon, which exacerbates heat risks for city dwellers. In addition to those surface-driven processes, synoptic-scale weather influences the urban microclimates and air pollution transport through its effects on the dynamics in the ABL. However, the understanding of many of these surface-atmosphere interactions remains limited due to a lack of comprehensive observations.
This thesis investigates the interaction between regional nocturnal Low-Level Jets (LLJs) and the urban atmosphere in the Paris region, using two years of Doppler Wind Lidar (DWL) observations at urban and suburban locations. A novel algorithm was developed for LLJ detection, and an innovative Doppler Beam Swinging (DBS) scan was introduced to enhance shallow LLJ monitoring. Results show that LLJs are a frequent phenomenon during summer and their characteristics vary with wind direction (e.g. strong LLJ mostly from the northeast). LLJs typically form after sunset and reach peaking heights around 200–950 m above the ground.
LLJs influence UHI intensity through the generation of mechanical vertical turbulence. During extreme heat events, air temperatures at night were up to 9°C higher in Paris city than in rural areas. Such high UHI intensities are found when mixing below the LLJs, which is weak as thermal stratification detaches the jet from the urban canopy layer. In accordance it was found that urban buoyancy and topography only modulate LLJ characteristics (e.g. core height) if sufficient vertical mixing is present. These findings emphasize the role of ABL dynamics as a critical link between synoptic flow and the urban canopy layer and highlight the importance of atmospheric mixing for characterizing urban heat risk and air pollution transport.

Institut Polytechnique de Paris
91120 Palaiseau, France